Title	Design and analysis of solid-core microstructured optical fiber sensors for sensing surrounding refractive index and surrounding temperature(Design and Analysis of Solid-Core Microstructured Optical Fiber Sensors for Sensing Surrounding Refractive Index and Surrounding Temperature, by LIM Jun Long)
Author(s)	Lim, Jun Long
Citation	Lim, J. L. (2018). Design and analysis of solid-core microstructured optical fiber sensors for sensing surrounding refractive index and surrounding temperature. Doctoral thesis, Nanyang Technological University, Singapore.
Date	2018-10-04
URL	http://hdl.handle.net/10220/46223
Rights	

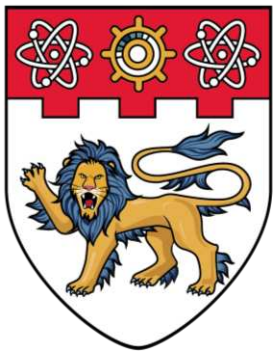

NANYANG TECHNOLOGICAL UNIVERSITY
SINGAPORE

DESIGN AND ANALYSIS OF SOLID-CORE MICROSTRUCTURED OPTICAL FIBER SENSORS FOR SENSING SURROUNDING REFRACTIVE INDEX AND SURROUNDING TEMPERATURE

LIM JUN LONG

SCHOOL OF ELECTRICAL AND ELECTRONIC ENGINEERING

2018

DESIGN AND ANALYSIS OF SOLID-CORE MICROSTRUCTURED OPTICAL FIBER SENSORS FOR SENSING SURROUNDING REFRACTIVE INDEX AND SURROUNDING TEMPERATURE

LIM JUN LONG

School of Electrical & Electronic Engineering

A thesis submitted to the Nanyang Technological University

in partial fulfillment of the requirement for the degree of

Doctor of Philosophy

2018

Abstract

The microhole collapsing effect technique is a relatively simple fabrication process that produces Photonic Crystal Fiber (PCF) refractometer using modal interferometry in the range of 10^{-5} refractive index resolution. The repeatable method preserves the same 125 μm structural integrity of the optical fiber for various applications such as multi-parameter sensing and bioaffinity. Compared to previous reports for conventional strain or temperature sensing using a single microbubble, the use of two microbubbles in the in-line microbubble structure significantly increases the light-molecule interaction for developing ultralow concentration biosensor. It has also been demonstrated as a potential reusable and label-less PCF biosensor platform. For temperature sensing, another low-complexity approach for fabricating a PCF directional coupler structure, without costly masking or precision marking laser, is also discussed. Numerical simulations have also been investigated on the PCF directional coupler structure to validate experimental result and on the microfluidic optical fiber device to rapidly find optimal fabrication-sensitivity design.

Preface

The preparation of this thesis started after the author's Qualifying Examination cum Confirmation Exercise. It is made in partial fulfillment of the requirement of the author's Ph.D. Many people have contributed in one way or another academically, practically and with research collaboration to this thesis.

The author expresses his sincere gratitude to his *Nanyang Technological University* supervisor Professor Perry Ping SHUM for his invaluable supervision and encouragement throughout the PhD journey. Dr. SHUM supervision has always been very productive and he provides the author various opportunities for research and interaction to improve his thesis.

The author greatly appreciates the support received through the collaborative work undertaken with:

- Mr. Huifeng WEI, Dr. Weijun TONG, and their team from *Yangtze Optical Fibre & Cable Company* (YOFC), China for providing the photonic crystal fiber and its supporting materials, and
- Prof. Roman DABROWSKI, Dr. Edward NOWINOWSKI-KRUSZELNICKI, and their team from *Military University of Technology*, Warsaw, Poland for providing the liquid crystal and its supporting materials.

The author would also like to special mention the collaborative work in co-authorship, noting discussions, and comments with the following:

- Prof. Perry Ping SHUM, *Nanyang Technological University*,
- Dr. Dora Juan Juan HU, *Agency for Science, Technology and Research (A*STAR)'s Institute for Infocomm Research*,
- Dr. Karolina MILENKO, *Warsaw University of Technology*, Poland,
- Dr. Yixin WANG, *A*STAR's Institute for Infocomm Research*,
- Dr. Emily Jianzhong HAO, *A*STAR's Institute for Infocomm Research*,
- Dr. Zhilin XU, *Nanyang Technological University*,
- Dr. Mi Kyoung PARK, *A*STAR's Institute of Microelectronics*,
- Dr. Linus Tzu-Hsiang KAO, *A*STAR's Institute of Microelectronics*,
- Dr. Rebecca Yen-Ni WONG, *A*STAR's Institute for Infocomm Research*,
- Mr.Varghese, *A*STAR's Institute for Infocomm Research*,
- Dr. Ying CUI, *Nanyang Technological University*,
- Dr. Yicheng LAI, *A*STAR's Data Storage Institute*,
- Dr. Zhifang WU, *Nanyang Technological University*,
- Dr. Guanghui WANG, *Nanyang Technological University*,
- Dr. Georges HUMBERT, *XLIM Research Institute*, France,
- Dr. Jean-Louis AUGUSTE, *XLIM Research Institute*, France,
- Dr. Muralidharan S/O Paramsothy, *A*STAR's Institute for Infocomm Research*, and
- Dr. Henry Wong Chuen Yuen, *A*STAR's Institute for Infocomm Research.*

Finally, the author would like to thank his family and friends for being there for him and being supportive throughout his entire candidature period.

Acknowledgement

The author gratefully acknowledges the funding and support received towards his PhD and thesis:

- *Agency for Science, Technology and Research (A*STAR) Scientific Staff Development Award (SSDA),*
- *A*STAR's TSRP Grant #102-152-0012*,
- *A*STAR's Infuse Exploratory Grant #I02-0331-03*,
- *A*STAR's Aerospace Programme Grant #1521500060*,
- *A*STAR* for its R&D facilities, and
- *Nanyang Technological University's* School of Electrical and Electronic Engineering for its R&D facilities;

Table of Contents

List of Figures

List of Tables

List of Abbreviations

Abbreviation	Full Meaning
APTES	3-Aminopropyltriethoxysilane
ASE	Amplified Spontaneous Emission
BPM	Beam Propagation Method
CAD	Computer Aided Design
EME	EigenMode Expansion
ESM	Endlessly Single Mode
FDE	Finite Difference Eigenmode
FDTD	Finite Difference Time Domain
FEM	Finite Element Method
FLICE	Femtosecond Laser Irradiation followed by Chemical Etching
FWHM	Full-Width Half-Maximum
GO	Geometrical Optics
HeNe	Helium-neon
LED	Light Emitting Diode
LMA	Large Mode Area
LPG	Long Period Grating
MCVD	Modified Chemical Vapor Deposition
MFBG	Microfiber-based Bragg Gratings

Abbreviation	**Full Meaning**
MMF	Multimode Fiber
MMI	Multimode Interference
MOF	Microstructured Optical Fiber
ND:YAG	Neodymium-Doped:Yttrium Aluminum Garnet
NLC	Nematic Liquid Crystal
OFS	Optical Fiber Sensor
OSA	Optical Spectrum Analyser
PBG	Photonic Bandgap
PBS	Phosphate Buffer Saline
PCF	Photonic Crystal Fiber
POA	Physical Optics Approximation
PWE	Plane Wave Expansion
RIU	Refractive Index Unit
RSoft	RSoft Photonic Component Design Suite
SLED	Superluminescent Diodes
SMF	Single Mode Fiber
SMT	Source Model Technique
TMM	Transfer Matrix Method
YOFC	Yangtze Optical Fibre & Cable Company

1. Introduction

1.1 Overview

In the first chapter of the thesis, the motivation, objectives, main contributions, and organisation of the thesis are presented.

1.2 Motivation

Since the invention of the Photonic Crystal Fiber (PCF) [1], it has attracted much interest because of its great potential for biosensing. PCFs have air holes along the whole length of the fiber. In general, the air holes of the cladding are arranged in a periodic index modulation and have a unique hexagonal symmetry. The advancement of PCF fabrication technology has made PCF of various design and patterns possible, which has enabled the PCF to be exploited to make numerous devices in sensing and communication applications.

One of the limitations that hinder deployment is the viability to fabricate on a commercial scale. Present research has been concentrating on improving the performance, in terms of sensitivity and dynamic range, based on established fabrication methodologies.

Moreover, many of the current methodologies require costly fabrication machinery, a need for highly stable environment for usage and are not repeatable. Therefore,

novel fabrication methodologies by modifying optical fibers to create new/improved existing sensors will open new frontiers.

1.3 Objectives

This thesis firstly aims to investigate the method of fabricating practical, robust and highly repeatable PCF sensors, and to examine its resonance wavelength when the surrounding refractive index or temperature changes.

1.4 Major Contribution of the Thesis

The major contributions of the author's work are summarised into four segments as follows:

1.4.1 Fiber Optics Device with Microbubbles for Sensing Refractive Index

A lab-based low-cost, robust and highly repeatable fabrication procedure is developed for fabricating the modal based interferometric refractometer, as shown in Figure 1.

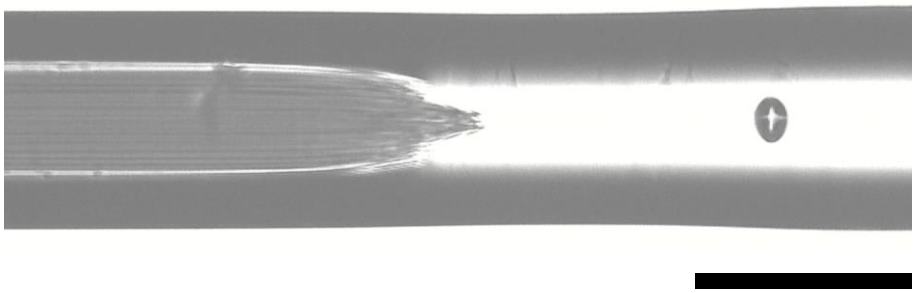

Figure 1: Microscopy image of one of the two spliced region of the in-line microbubble Photonic Crystal Fiber (PCF) sensor. On the left is the PCF and on the right the standard single mode fiber. In the middle are the collapsed regions and the air microbubble. The black scale bar shows 125 μm.

One sensor has two such interfaces that exhibits high response to changes in the surrounding refractive index, which has many potential sensing applications, especially in life science. A thorough search of the relevant literature yielded this work is first to report refractive index sensing using the in-line microbubble PCF sensor and first to report the use of a two-microbubble structured sensor. Prior work with microbubble defects have mainly focused on strain and/or temperature sensing and have a longer sensor length.

1.4.2 Applications for the In-line Microbubble Photonic Crystal Fiber Sensor

Having established the PCF interferometric device with two in-line microbubbles, further investigation for refractive index sensing applications have been carried out. Firstly, two of those sensors are spliced in series, and demonstrated multiplexed refractive index sensing at two different locations. Secondly, another in-line microbubble PCF sensor is spliced to a Long Period Grating (LPG) sensor for dual parameter sensing. The surrounding refractive index and temperature sensing is established to form a Sensor Matrix. The result shows that there is a deviation of less than 3×10^{-4} in refractive index.

Thirdly, a biosensor is fabricated using another in-line microbubble PCF sensor with a biochemical coating. An ultralow concentration of 10 μg protein in 1 ml of buffer solution is detected and verified using fluorescent label. In practice, the bioaffinity test can be made label-free to address the limitations associated with labels. The maximum shift of the resonance wavelength due to the bioaffinity event is 210 pm, which is easily measured by an entry level detector system. A thorough search of the relevant literature yielded that this work is first to report a bioaffinity test using an in-line microbubble PCF sensor or a PCF-based modal interferometry. The theoretical refractive index resolution of the sensor is 6.25×10^{-5}.

1.4.3 Nematic Liquid Crystal-PCF Device for Temperature Sensing

A low-cost, simple and efficient method to demonstrate the feasibility of manufacturing a highly temperature responsive sensor, is experimentally conducted. Theoretical calculation results using simulation software validates the experimental results. The device is based on the mode coupling between the nematic liquid crystal channel and the PCF's core modes. The temperature response of the fabricated device using various infiltration lengths is also characterised. A thorough search of the relevant literature yielded the work is the first of its kind to realize a highly temperature sensitive directional coupler. The measured mean and standard deviation temperature sensitivity are −3.79 nm/ °C and −0.153 nm/ °C respectively. The theoretical refractive index sensitivity and refractive index resolution of the calculated model corresponds to −7201 nm/ RIU and -2.8×10^{-6}, respectively.

1.4.4 Theoretical Analysis of a Transverse Micro-channel Fiber Optics Device

A micro-channel structure inside a Single Mode Fiber (SMF) is calculated and modelled using simulation software. The model is validated using previously reported results, where its calculated refractive index response matches with high degree of accuracy to the experimental results. Further investigation reveals that the transverse micro-channel is influenced by many geometry factors. A novel output power detection scheme is proposed to find the refractive index response rapidly for a given set of refractive index change. The proposed solution produces unique 3D profile plots to find the most

optimal fabrication-sensitivity design. At the most optimum dimension and operating condition, the best theoretical refractive index sensitivity and refractive index resolution are 581 dB/ RIU and 1.7×10^{-5}, respectively.

1.5 Organisation of the Thesis

The thesis is divided into seven major chapters and further divided into sections and sub-section appropriate to the topic. After the introduction in Chapter 1, Chapter 2 reviews and discusses the overview of optical fibers, methods of fabricating optical fiber sensors and numerical modelling methods. Three major modifications methods, external cladding sensing mechanism, selective infiltration *and* micro-channel through the standard single mode fiber, are discussed in the next four chapter.

Chapter 3 focuses on the design and fabrication of a novel in-line microbubble PCF interferometric device as a sensor, and how the PCF is used to fabricate the sensor. The sensor senses a change in refractive index around its cladding using the external cladding sensing mechanism. The technique forms a microbubble, usually unwanted in other applications, for creating a unique interference pattern that has resonance wavelength moving to higher wavelength as the surrounding refractive index increases.

Chapter 4 demonstrates the in-line microbubble PCF interferometric device for experimental temperature sensing and surrounding refractive index sensing. The unique refractometer has very strong mechanical strength and is reusable in life science application too. The measurement results and analysis result are plotted and described for each application.

In Chapter 5, another method on selective infiltration is discussed. In contrast to the external cladding sensing mechanism in Chapter 4, the analyte is now inside the optical fiber that changes refractive index as temperature changes. Nematic liquid crystal infiltrated into an air hole channel next to the core of the PCF is reported. A brief overview introduces the device followed, by the fabrication technique. A directional coupler structure demonstrates its temperature sensing capability with the simulation and experiment results.

The design and analysis of another optical fiber device is documented in Chapter 6. It senses changes in refractive index by a micro-channel through the standard single mode fiber. A transverse micro-channel inside the SMF is modelled using the RSoft simulation software. Different geometry parameters are calculated and an output power detection scheme is proposed, to find the optimal fabrication-sensitivity design.

Finally in the last chapter of the thesis, the thesis's research outcomes are wrapped up and recommendations on possible future work are proposed. A list of the author's publication toward this thesis are listed, followed by the references cited

and referred to in the thesis. Other supporting parts of the thesis are listed in the Table of Contents.

2. Literature Review

2.1 Introduction

This chapter aims to highlight some of the major developments and set the scene for discussion of the thesis. It describes some of the most significant issues, board references pointing to major achievements and areas of importance in the optical fiber sensor field.

Glass, as we know it, is a clear or translucent material used for various kinds of objects, such as bottle, window, mirrors, eyewear lenses, etc. It is an inorganic solid that comes in different colours, shapes, sizes, etc. It can be hard or soft, brittle or resilient, and able to withstand wind, rain or sun depending on how it is made. Natural glass has existed since the beginning of time. Early human in the Stone Age used natural occurring glass, like obsidian (70-75% silicon dioxide, remaining magnesium oxide and iron oxide), as cutting tools. Obsidian is a shiny black glass that is formed when lava cools down rapidly, such as by flowing into water. Human first discovered how to make glass in the middle of the second millennium BC, during the Middle to the Late Bronze Age. The origin of the first glass production in a regular and controlled way [2] probably comes from the region around ancient Near East (present day northern Iraq and Syria). Craftsmen have been making glass for thousands of year manually; before the mass production factory-made era arrived and spread glass technology to the masses in the modern age, eventually leading to the invention of optical fiber.

2.2 Overview of Optical Fiber

In the 1960s, Charles Kuen Kao and his co-workers made discovery that led to a breakthrough in optical fiber technology. They investigate how light transmits over long distances using optical fiber, and find out that the purity of the glass is the main problem rather than the fundamental physical effects, and such impurity could be removed. Yet, it is not until the 1970s that this ultrapure silica optical fiber, with high melting point and low refractive index, is invented by Corning Glass Works researchers, Donald Keck, and Peter Schultz, as described in Patent #3,711,262 [3]. The patent describes the method to produce high purity fused silica that is capable of carrying at least five orders more information than copper wire, at that time. They solved the high loss problem cause by the impurities in glass fiber as proposed by Kao *et al* in 1966 [4]. They invent the world first functional low-loss optical fiber that would become the communication backbone of today. They have purified materials in vapour phase deposited into cylindrical performs and use precisely controlled dopants to make the refractive index of the core a little bit higher than the cladding. The whole process is done without increasing the attenuation significantly.

Optical fibers can be made either with glass or plastic material to confine light within the waveguide. Optical fibers are flexible, transparent strand of glass used to transmit light between two ends. It is usually made of silica and the thickness is slightly more than the human hair. They permit signal transmission over long distances and have a higher bandwidth than copper wires. Their signal experiences

less loss are immune to electromagnetic interference, etc. The thesis' main research efforts concentrate on the silica material (a type of glass) optical fiber.

More recently, PCFs have received greater recognition and more interest in research. They are another type of optical fiber different from conventional optical fiber. They have air holes or microstructured features inside the optical fiber that guide light by a solid core or through an air core. More details on PCFs' development, performance and light guidance mechanisms are discussed in Chapter 3.

Table 1 shows the survey of diverse parameters when splicing different varieties of optical fibers. A typical splice between two pieces of single mode fiber can achieve very low insertion loss. When other kinds of optical fibers are spliced to itself or with another kind, the insertion loss varies greatly depending on the geometry, structure, materials, splice settings, etc.

Varieties of optical fiber	Cladding diameter (µm)	Type of fusion splicer machine	Fiber alignment	Splice loss (dB)
Standard single mode fiber	125	Standard	Core-to-core	0.02 to 0.05
Other standards (such as multimode, rare-earth doped, etc.)	80 to 400	Specialty splicers	Core-to-core/ core-to-cladding/ cladding-to-cladding	0.19 to 2.53 [5], vary with structure and cladding diameter
Photonic Crystal Fiber (PCF)	125 to >258			

Table 1: Survey of splicing different types of optical fiber [6].

In general, PCF suffers more insertion loss when spliced with the standard single mode fiber when compared to two pieces of SMF. The PCF splice loss can be described as a function of the air holes' geometry, i.e. pitch (Λ) and diameter (d) of the air holes [6]. In other words, the spacing between the air holes and ratio of the diameter-to-pitch, $\frac{d}{\Lambda}$, affect how light propagates through the splice interface. An example is when the large mode area PCF is spliced with a step index SMF, the splice loss varies from 1 dB to ~5 dB when $\frac{d}{\Lambda}$ changes from 0.15 to 0.53 [7]. The minimum splice loss point also corresponds to the optimal modal field match between the single mode fiber and the PCF.

2.3 Overview of Optical Fiber Interferometry

Optical interferometry is well known for its ability to make precise measurement of optical path difference or changes that induce a physical displacement or refractive index change. Early optical interferometers are limited by poor spatial and temporal coherence. The invention of the laser in the 1960s dramatically improved optical measurements. However, those optical interferometers are limited by the alignment of optical beams to achieve noiseless measurement.

With the rapid development in optical fiber communication, all-optical-fiber versions of classical interferometers are demonstrated. These optical fiber interferometers solve many of the alignment problems and displaced bulky optical interferometers. The idea for incorporating optical fiber into optical interferometry [8] allowed many robust and versatile photonic systems to be developed since the 1970s. This pioneering work continues to evolve and their contribution have produced many viable alternative technologies to electronics. Compact, lightweight, electrically isolated, immune to electromagnetic interference, etc, are some advantages that make optical fiber interferometer a formidable opponent in sensor research. Their uses are fast spreading and they play a significant role in the emerging market of civil engineering and security.

Optical fiber interferometers are grouped into three types according to how the phase change is induced. Firstly, when the sensing element and measurands cause a phase change inside the fiber waveguide, it is an intrinsic sensor. When there is an auxiliary sensing element used to convert the measurands and couple it to the fiber,

it is an extrinsic sensor. When the measurands induce a change in dimension of a sensing element, it is an external sensor.

The optical fiber interferometer is classified as a point sensor or a distributed sensor. Those in between these two types are termed as quasi-distributed sensors. The optical fiber interferometer, being an optical fiber, is subjected to one or more kinds of perturbation for sensing. Modulation of light caused by the changes in refractive index, size, shape, or strain converts measurands to a corresponding change in the light output. Surrounding refractive index, temperature, strain and electric field are some popular measurands.

The most common type of optical fiber interferometer is the all-fiber two-beam interferometers, namely the Michelson, the Mach-Zehnder, the Fizeau and the Sagnac interferometers. Two-beam interferometers generally have a light source divided into two arms to form a reference arm and a sensing arm. The arms will experience optical path difference changes induced by the measurands. An interference pattern is generated at the output by the total irradiance [9]:

$$I = I_1 + I_2 + 2\sqrt{I_1 I_2}cos\varphi, \tag{1}$$

where I_1 and I_2 are intensity from the reference arm and sensing arm, L is the arm length, λ is the wavelength, and φ is the optical phase difference.

When there is constructive interference, $\varphi = 0, \pm 2\pi, ...$, there is a maximal in the interference pattern. The total irradiance (1) becomes:

$$I = I_1 + I_2 + 2\sqrt{I_1 I_2}. \quad (2)$$

When there is destructive interference, $\varphi = \pm\pi, \pm 3\pi, ...,$ there is a minimal in the interference pattern. The total irradiance (1) becomes:

$$I = I_1 + I_2 - 2\sqrt{I_1 I_2}. \quad (3)$$

The visibility of the interference pattern can also be described by:

$$V = \frac{I_{max} - I_{min}}{I_{max} + I_{min}}, \quad (4)$$

where I_{max} and I_{min} are the maximum and minimum intensities.

2.4 Overview of Optical Fiber Sensor

Optical Fiber Sensors (OFSs) have experienced tremendous growth over the past several decades. The advancement in manufacturing components for mass production (such as laser and optoelectronics) have driven cost down with improved quality, gradually displacing traditional sensors. OFS provides an alternative to traditional sensors used for measuring acceleration, magnetic-field, temperature, pressure, acoustics, vibration, strain, humidity, bio-chemical, etc.

The inherent advantages of OFS has enabled them to offset their major disadvantages of high cost. Some of the appealing advantages are high sensitivity to environmental changes (such as temperature, pressure, refractive index and bio-chemical) and environmental ruggedness.

The most common grouping of OFSs is into extrinsic and intrinsic sensors [10]. Extrinsic OFSs guide light using optical fiber but the interaction of light and quantity in measurement takes place outside the optical fiber. Some of the extrinsic OFS applications include gratings, fluorescence, evanescent, laser Doppler velocimetry, and absorption band edge. Intrinsic OFSs on the other hand have the interaction take place within the optical fiber itself. Some of the intrinsic OFS applications include microbend sensor, distributed sensor, and interferometric sensor. In this thesis, Chapter 3, 4, and 6 will describe extrinsic OFSs while Chapter 5 will describe an intrinsic OFS.

Optical fibers can be connected in different configurations of interferometry to form OFSs, as described in Section 2.3. They may also be physically modified to form an all-fiber OFS with techniques such as Fiber Bragg Gratings (FBG), Long Period Gratings (LPG) or sandwiching another kind of optical fiber in between two pieces of SMF. An overview of the major equipment needed for fabrication of mainstream optical fiber sensor in research is tabulated in Table 2.

Physical modification methods	Vibration isolation	Type of laser used to fabricate	Other notable items
Fiber Bragg Gratings (FBG)	Yes	Excimer laser, femtosecond laser, ND:YAG laser	Alignment stages and optics, phase mask per sensor, UV-sensitive optical fibers
Long Period Gratings (LPG)	Yes	Excimer laser, carbon dioxide laser, femtosecond laser, ND:YAG laser	
Chemical etching	No	No	Hydrofluoric acid
Sandwiched in between two single mode fibers on both side	No, in general, depending on setup	No	Depending on the method, may need middle or high end fusion splicer machine

Table 2: Overview of major equipment needed for fabrication of mainstream Optical Fiber Sensors (OFSs) in research. ND:YAG denote Neodymium-Doped:Yttrium Aluminum Garnet. UV denotes Ultra-Violet.

Both FBG and LPG are mainstream OFSs used for broad applications in optical fiber communication, spectroscopy and sensing. To manufacture those sensors, they require vibration free location for positioning alignment stages and optics and may not be suitable for some raised flooring. Depending on the type of grating, costly phase mask, UV-sensitive optical fibers or annealing ovens may be used. The phase masks and the laser system form a large slice of the setup cost. Phase

masks are often utilised for mass production. The lasers used are usually bulky and require active cooling to extend the operational life.

The resonance wavelength of LPG, λ_{LPG}, is determined by the phase matching condition [11]:

$$\lambda_{\mathrm{LPG}} = \left(n_{core}^{eff} - n_{clad}^{eff}\right)\Lambda, \tag{5}$$

where n_{core}^{eff} is the effective refractive index of the fundamental core mode and $n_{clad}^{eff}$is the effective refractive index of the *m*th cladding mode.

When LPG is used for sensing its surrounding refractive index, the refractive index sensitivity, $\frac{d\lambda_{\mathrm{LPG}}}{dn_s}$, expression is [11]:

$$\frac{d\lambda_{\mathrm{LPG}}}{dn_s} = \lambda_{LPG} \cdot \Upsilon \cdot \Gamma, \tag{6}$$

where Υ is the waveguide dispersion defined by:

$$\Upsilon = \frac{\frac{d\lambda_{\mathrm{LPG}}}{d\Lambda}}{n_{core}^{eff} - n_{clad,m}^{eff}} \tag{7}$$

and Γ is the surrounding refractive index dependence defined by:

$$\Gamma = -\frac{u_m^2 \lambda_{LPG}^3 n_s}{8\pi r_{clad}^3 n_{clad}\left(n_{core}^{eff} - n_{clad,m}^{eff}\right)\left(n_{clad}^2 - n_s^2\right)^{\frac{3}{2}}} \tag{8}$$

where u_m is the *m*th root of the zeroth-order Bessel function of the first kind, r_{clad} is the optical fiber cladding's radius and n_{clad}^{eff} is the optical fiber cladding's effective refractive index.

Chemical etching is another common method to fabricate a OFS tip. The method is relatively low cost and reproducible [12]. However, the etching solution used to etch the silica material is also highly hazardous, with acute hazardous effects. Hydrofluoric acid is one of the strongest inorganic acid components in etching solution, which is very harmful, particularly aggressive to soft tissues, has systemic toxicity and creates symptoms that may not be obvious immediately after exposure [13]. The overall chemical reaction of fused silica and hydrofluoric acid is [14]:

$$SiO_2 + 6\text{HF} = 2H_2O + H_2SiF_6. \quad (9)$$

An application of the etched OFS tip is used to make an intrinsic Fabry–Pérot OFS using a fusion splicer machine for creating microbubble [14].

A common method used to fabricate an OFS for refractive index sensing is to sandwich another optical fiber type that can propagate light interaction with the surrounding refractive index. This optical fiber is spliced in between two SMF, which lead to a light source and a detector on either side. Sandwiching a Multimode Fiber (MMF) excites modes that are influenced by external perturbation. The length of the MMF has been reported not to have a significant impact on the refractive index, but the diameter of the MMF does [15]. The method creates an interference pattern by Multimode Interference (MMI) that has strong periodic

resonance wavelengths. The spacing between the two resonance wavelengths, $\Delta\lambda_{2\pi}$, is described by the parameters of the MMF [16]:

$$\Delta\lambda_{2\pi} = \frac{\pi^2 a^2 n_{core}^3}{NA^2 L}, \tag{10}$$

where a is the core's radius, n_{core} is the core's refractive index, NA is the numerical aperture and L is the length.

The use of sandwiching 50 µm diameter MMF has been proposed to improve refractive index sensitivity [15]. However, the thin cladding diameter of the optical fiber may pose challenges during the splicing process and there is uncertainly in it surviving the harsh procedures [17] and conditions for use in biosensing (without breaking).

The techniques listed in Table 2 may either use conventional optical fiber, PCF, or both to make an OFS. Table 3 tabulates some examples of reported OFS for refractive index sensing using the discussed methods and optical fibers.

Physical modification methods	**Refractive index resolution (refractive index range)**	
	Conventional optical fiber	**Photonic Crystal Fiber (PCF)**
Fiber Bragg Gratings (FBG)	1.0×10^{-4} *"197.03 nm/RIU"* (1.36 to 1.42) [18][a]	2.2 to 6.7×10^{-5} (1.4 to 1.44) [19]
Long Period Gratings (LPG)	6.49×10^{-4} (1.33 to 1.38) [20]	2×10^{-5} (~1.33) [21]
Chemical etching	8.9×10^{-3} *"45.05 dB/RIU"* (1.33 to 1.395) [22][a]	2.7×10^{-5} *"750 nm/RIU"* (1.3739 to 1.3577) [23][a]
Sandwiched in between two single mode fibers on both side	1.1×10^{-4} *"180 nm/RIU"* (1.342 to 1.352) [15][a]	6.25×10^{-5} (1.33 to 1.34) [17]

[a] Theoretical calculated with either level accuracy of 0.4 dB or wavelength accuracy of 0.02 nm using original information quoted in italic, if refractive index resolution not stated in references

Table 3: Overview of refractive index responses from the discussed methods and optical fibers.

FBGs and LPGs are traditional OFS sensing methodologies used for refractive index sensing [18, 20]. Gratings incorporating PCFs have high resolution OFSs, sensitivity with narrow resonance wavelengths using FBGs and another with cladding modes resonances using LPGs [19]. Chemical etching provides the means to remove materials from optical fibers to increase the interaction between light and external refractive index [22, 23]. The sandwiched method has the advantage of low cost and ease of fabrication [15].

From Table 3, it can be seen that the refractive index resolution from the various types of optical fiber and method have an estimated resolution ranging from 10^{-5} to

10^{-3}. PCFs OFS in general have an order higher refractive index resolution over conventional optical fibers OFS because of the ability to manipulate how light is confined in the waveguide by changing the microstructure design.

Conventional optical fiber, such as step index SMF, has strict design rules to follow for core and cladding diameter, modal cut off wavelength, etc. hindering the development of more specialised dispersion or birefringence application. They are designed to have minimum confinement losses to keep as little light leakage as possible for long haul optical fiber communication. The limited amount of light propagating near its external surrounding medium reduces the light-matter interactions required for refractive index sensing.

PCF on the other hand allows for the alter of light propagation characteristic achieving unconventional propagation properties, such as endlessly single-mode guidance [24, 25] by adjusting the geometry of the air holes and spacing between air holes, or substantial interaction between the light guided along the optical fiber and surrounding medium for refractive index sensing by for example using a very small core PCF for propagating large evanescent field [26, 27].

When multiple methods are combined, for example the FBG, chemical etching and Fabry-Pérot interferometer on an SMF, similar refractive index response in the order of 10^{-5} could also be achieved [28].

For FBGs on a standard SMF, the Bragg wavelength (resonance wavelength) is:

$$\lambda_B = 2 \cdot n_{eff} \Lambda, \tag{11}$$

where n_{eff} is the effective refractive index and Λ is the period of the Bragg grating. The cladding of the single mode fiber has to be removed to significantly increase the evanescent field interaction with the surrounding medium creating a Microfiber-based Bragg gratings (MFBG) OFS [29]. The Bragg wavelength is rewritten into a function of the microfiber's radius and surrounding refractive index:

$$\lambda_B = 2 \cdot n_{eff}(r_{MF}, n_s)\Lambda, \tag{12}$$

where r_{MF} is the microfiber's radius and n_s is the surrounding refractive index.

The refractive index sensitivity, S_{MFBG}, of the MFBG is therefore defined as [29]:

$$S_{MFBG} = \frac{d\lambda_B}{dn_s} = \frac{d\lambda_B}{\delta n_{eff}(r_{MF},n_s)} \frac{\delta n_{eff}(r_{MF},n_s)}{\delta n_s} = 2\Lambda \frac{\delta n_{eff}(r_{MF},n_s)}{\delta n_s}. \tag{13}$$

2.5 Overview of Numerical Modelling

There are numerous software available in the market [30, 31] to investigate electromagnetic wave propagation in optical waveguides. They are divided into three categories – wave propagator, mode solver, and system simulator. Wave propagator can model uniform and non-uniform waveguide in the longitudinal propagation direction, while the mode solver models only the uniform waveguide in the propagation direction.

The first category, wave propagator, allows realistic devices to be modelled by having the abilities to arbitrarily launch input and monitor the beam or pulse at any

point of the structure. The technique includes both the time domain method and frequency domain method. Examples of the time domain method are Finite Difference Time Domain (FDTD) Method, and the Finite Element Method (FEM). The FDTD method is computationally intensive when modeling complex large structure in the time domain. The modal properties are only generated at the end of every propagation run, which may not be suitable for a rapid design process. The FEM is a versatile method that can be implemented in both the time and frequency domain. Depending on how it is programmed by the manufacturer, the FEM can be a wave propagator, a mode solver, or both at the same time. In the frequency domain method, some examples are the Beam Propagation Method (BPM), the Transfer Matrix Method (TMM), and the EigenMode Expansion (EME) method. The BPM solves wave propagation problem for any given frequency. It is a versatile technique for calculating complex refractive index profiles and structures. More advanced techniques, such as wide-angle BPM, bi-directional BPM, semi-vectorial BPM and full-vectorial BPM have been developed to model reflective or grating structures. Similarly in the TMM and EME method, both methods are also able to model bi-directionally.

The second category, the mode solver, has overlapping methodologies with the wave propagator category, such as the BPM, TMM, EME method, and FEM. Other non-overlapping methods or techniques used for the mode solver category are Plane Wave Expansion (PWE) method, Source Model Technique (SMT) method, and multipole method. PWE method operates in the frequency domain for complex waveguide structures. The fields in the waveguide structures expand, as Tong put it

simply in his book: "definite-frequency states in some truncation of a complete basis" [32], and solve the resulting linear eigenproblem. The SMT method is a fully vectorial method to find modes in an arbitrarily shaped piecewise-homogeneous waveguide structures. The multipole method operates similarly to SMT method but is restricted to circular shaped nonintersecting homogeneous waveguide structures. This category of simulator finds the guided modes and the refractive index profile of waveguide structures.

The third category, system simulator, models many photonic components and devices at different level at the system level. They play an important role for system design when it is not practical to conduct experiment due to cost or lack of resources. Individual models, such as a blackbox, measurement or physical, can be altered or turned on or off independently to investigate the overall system performance.

Some examples of commercial software that uses the methods discussed are the RSoft Photonic Component Design Suite (Synopsys, Inc.), referred to as RSoft for the rest of this thesis; and the MODE Solutions (Lumerical Solutions, Inc.) referred to as Lumerical for the rest of this thesis.

The RSoft software is capable of modelling complex three dimension structures and simulates both passive and active photonic devices. The suite has a CAD environment to design layout and define parameters of photonics device, and numerous simulation engines to simulate and compute different type of light propagation by different numerical methods. The three dimension and object

oriented design features of the CAD environment allows complex waveguide structures to be modelled. Its hierarchical layout also supports complicated waveguides to be built from smaller waveguides. One of the simulation engines, the BeamPROP, uses BPM algorithm for fast and accurate design and simulation of waveguide structures. It is based on the implicit finite-difference scheme that calculates the output of time-update depending on itself. It is commonly used by researchers to solve intensity and modes based structures, and are generally not suitable for Maxwell equations related problem like FDTD method, or FEM [30].

The Lumerical MODE Solutions software models the spatial profile and frequency dependence of modes by solving Maxwell's equations on a cross section of the waveguide. It utilises the Finite-Difference Eigenmode solver or the EME method to solve the mode profiles, effective index, and loss. Images of the cross sectional view of optical fiber for example can be imported directly into the software and find its modes easily. This thesis makes use of the RSoft BeamPROP and the Lumerical Mode Solutions to model and support its finding in the later chapters.

3. Design and Fabrication of Photonic Crystal Fiber Device with Microbubble

3.1 Introduction

In this chapter, the Photonic Crystal Fiber (PCF) and microbubble in an optical fiber are briefly introduced, followed by the description of the design and fabrication of a novel in-line microbubble PCF interferometric device.

3.1.1 Photonic Crystal Fiber

Kaiser *et al* proposed the Microstructured Optical Fiber (MOF) [8] to solve the high insertion loss problem in 1974. They proposed to confine light in the solid silica core with air cladding instead of solid cladding. Although the concept had potential, the fabrication technology at that time cannot compete with Modified Chemical Vapor Deposition (MCVD). The MCVD fabrication technique is still in use for today's standard optical fiber manufacturing. Hence, MOF development has been sluggish until the 1990s. Then hope came when Yablonovitch *et al* developed the first photonic crystal in 1987.

The emerging photonic crystal consists of periodic dielectric structure that affects the propagation of electromagnetic waves. When applied to fiber optics,

the propagation of light is highly dependent on wavelength. With the knowledge of photonic crystal, Knight *et al* successfully fabricated the first PCF in 1996 [33]. He differentiates the PCF against the MOF by stating that PCF has '*a periodic index modulation in the cladding and a unique hexagonal symmetry*' [1]. It has attracted much attention and interest because it displays novel optical properties that conventional optical fibers cannot achieve.

In recent decade, both MOFs and PCFs are interchangeably used to describe one another by researchers. Many other names and terminologies [34], such as air-silica guiding optical fiber, air-silica holey fiber, holey fiber, effective index guiding fiber, air hole cladding fiber, photonic band gap fiber, hollow ring core fiber, etc., are also reported and classified for various designs.

For silica based optical fibers, the stacking technique is the most widespread and straightforward method to fabricate PCF preforms. Various capillary tubes and rods are stacked together to form the designed geometry of the preforms. Other methods, such as drilling, extrusion and moulding, have been developed over the years to create the holes in preforms. After forming the PCF preforms, the actual PCF can be drawn, similarly like the MCVD, using fiber drawing tower.

Bennett *et al* has shown that early PCFs exhibit attenuation loss in the order of 0.24 dB/m at 1550 nm and is limited to about fifty meters in length [35]. As the fabrication technology of the PCF advance, the PCF's attenuation loss improves to 0.37 dB/Km at 1550 nm and 0.71 dB/Km at 1310 nm for a

distance of 10 Km [36]. Those achievements from Tajima *et al* improved their polishing and etching process [36] to overcome the high attenuation loss. The roughness of the air hole surface along the PCF is attributed to the high attenuation loss during fabrication.

PCF is a waveguide that transmits light either through its solid or hollow core. The core is surrounded by a microstructured cladding of air holes. The array of air holes runs along the optical fiber axis. The air holes may vary in different shapes and sizes depending on their design applications.

PCF are grouped into two classes according to their modes of operation or in other words their mechanisms for light confinement. The guiding mechanism depends whether the cladding's refractive index is higher or lower than the core. The main difference between the two is that index guiding PCF's guided modes are a continuum whereas Photonic BandGap (PBG) PCF has a discrete set of guided modes separated by the bandgap.

A PCF with a solid core has a higher effective refractive index than its surrounding cladding air holes, operating like conventional optical fiber. They are index-guided PCF that confine light in the core by a modified total internal reflection. An example is the Endlessly Single Mode (ESM) PCF [1]. Birks *et al* demonstrate that ESM PCF confines only single mode beyond 337 nm [24]. As the core size increases, the ESM becomes a Large Mode Area (LMA) PCF [25]. Maintaining the ESM principle, the LMA PCF large effective area and high NA PCF make it an excellent candidate for high-power application in

recent times. The LMA PCF also has low nonlinearity and optical fiber damage properties making it promising to construct a fiber laser and amplifier with very short length of fiber.

PCFs with light confinement in the air core operate by the photonic bandgap effect. The air core has a lower effective refractive index than the surrounding cladding air holes. A low index defect, such as the hollow core fiber, is by far the most advanced two dimensional photonic bandgap structures that guide lights in the air core [37, 38]. It has low nonlinearity and fiber damage properties making it suitable for high-power delivery and gas sensing.

The PCF can be separated into four categories or groups by their confinement methodology – PBG fiber, holey fiber, hole-assisted fiber and Bragg fiber [39, 40, 41, 42, 43, 44]. The PBG fiber confines light by the bandgap effect using a periodic air hole arrangement, the holey fiber confines light by air hole arrangement, the hole-assisted fiber confines light by the presence of air holes in a conventional higher-index core, and the Bragg fiber confines light by the bandgap effect with concentric rings of a multilayer film. Some of the unique and practical applications possible with a PCF are supercontinuum generation sources [45], medical imaging [46], and special optical communication components [47, 48, 49].

3.1.2 Photonic Crystal Fiber Device with Microbubble

PCF interferometers are emerging as a frontier in optical fiber sensors because of its great potential. Rapid advancement of PCF fabrication technology and availability of off-the-shelf PCFs have made PCFs a viable platform for sensing physical parameters. It has been widely used in temperature [50, 51, 20], strain [52, 53] and refractive index [54, 55, 17, 56, 57] measurement. There are other sensing platforms that are well-known approaches for altering the PCF structurally for sensing. FBGs [58], LPGs [59], side polishing [60], and fiber tapering [61], *etc*. are some common approaches. They possess vital disadvantages such as the need for vibration isolation table, the manual labor, and the weakening of optical fiber integrity due to change in structure, force and/or curvature.

Refractive index sensing using an in-line microbubble PCF sensor has been demonstrated [17] [56]. The reported sensor operates in reflection. When varying the surrounding refractive index from 1.33 to 1.40, the sensor exhibits a refractive index sensitivity of 11.5 nm/ RIU. RIU stands for Refractive Index Unit. In another report, the sensor operates in the transmission configuration [17]. It shows refractive index sensitivity 320 nm/ RIU and refractive index resolution 3×10^{-5}.

In comparison the transmission configuration has twenty-seven times the refractive index responsiveness than the reflection configuration. Higher refractive index sensitivity facilitates bioaffinity measurement. Being capable

of detecting specific bio-molecules, it is appealing as a promising new class of bio-analytic devices. To the best knowledge of the author through thorough search of the relevant literature, this type of modal interferometer, the in-line microbubble PCF sensor for *refractive index sensing*, is the first of its kind.

A thorough search of the relevant literature yielded only Li *et al* [53] who demonstrated PCF based sensor with microbubble for sensing purpose. The microbubble acts as a microcavity that has air-silica interfaces of the microbubble to form a low reflection Fizeau interferometer for strain sensing. The interferometric sensor of this type operates in the reflective configuration. Numerous beams of light reflecting off the silica-air-silica surfaces create many beams of light interfere with one another. The presence of the microbubble slightly weakens the tensile strength of the fiber, but achieves 3000 με without breakage. Tensile stress has been reported to operate better than FBGs [53]. Furthermore, the Fizeau interferometer can also function as a high temperature sensor. Due to the low temperature sensitivity, the sensor has a very large dynamic range. Temperature sensitivity is in the range of a few to tens of pm/°C. The change of strain or temperature modulates the optical properties of light in the interferometric sensor. The characteristic of the measured spectrum are traced for measurement. For example, the fringe spacing (free spectral range), maximal (peak), and minimal (dips) are tracked for the change in wavelength, phase or intensity. In the context of an interferometric sensor, it is worth mentioning that most efforts have been concentrated on temperature and strain sensing.

3.1.3 Light Scattering By Microbubble

The Mie theory and physical optics are used to describe the light scattering by microbubble [62]. Depending on the context, the microbubble is also called air bubble, hollow sphere, cavity, spherical inclusion, hole *etc*.

In the Geometrical Optics (GO), the spherical microbubble illuminates by a plane wave experience total reflection when the incident angle is greater than the critical angle [63]:

$$\theta_c = \pi - 2\phi_c, \tag{14}$$

where $\phi_c = sin^{-1}\frac{m_b}{m_s}, m = \frac{m_b}{m_s} < 1$, m_s and m_b are the refractive indices of the surroundings medium and the bubble medium respectively.

In the Physical Optics Approximation (POA), the reflection contribution (p = 0) and refraction contribution (p = 1) account for most of the scattering light [63] near the critical scattering angle. p = 0 rays in the near field has only external reflection [64]. The rays are all reflected when the angle of incidence ray (θ_i) satisfies:

$$\sin\theta_i \geqslant \sin\theta_c = n_i/n_o. \tag{15}$$

In the far field, the rays produce a diffraction scattering pattern in the critical scattering pattern. Rays that has $\theta_i < \theta_c$ pass through the microbubble by refractions. p = 1 rays refract twice and interfere with p = 0 rays. The fine

structure in the coarse structure of Figure 2(b) are interference generated by the neglected p = 2 and p = 2' rays.

Other pointer to take note is the coarse and fine structures are dependent on the size and shape of the microbubble. When the microbubble is too small, the Rayleigh scattering theory takes over light scattering pattern. When the shape of the microbubble is spheroid, the ray optics predictions of the sphere are still valid as long as major or minor axis lies in the scattering plane.

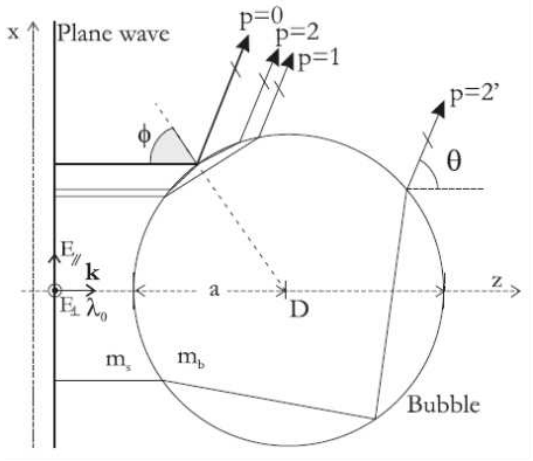

(a)

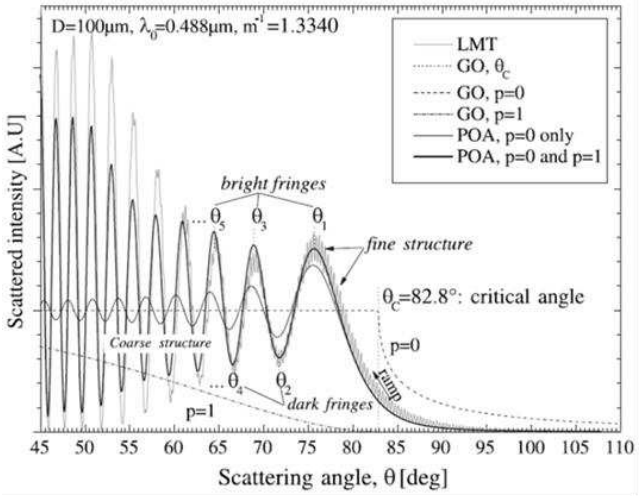

(b)

Figure 2: (a) Scattered rays in the near-critical angle scattering region when a plane wave is incident to a microbubble from reference [63]. (b) Light scattering pattern near the critical angle by one air bubble in the water from reference [63]. LMT denotes Lorenz-Mie Theory. GO denotes Geometrical Optics. POA denotes Physical Optics Approximation. p = 0 denotes reflection contribution. p = 1 denotes refraction contribution.

In the context of light propagating through optical fiber, the loss due to light deflecting out caused by microbubbles is referred as extrinsic scattering loss [65]. The primary cause for formation of these bubbles comes during optical fiber fabrication and may even form during the optical fiber splicing. These defects are not negligible and they scatter a significant fraction of light out of fiber waveguides [66].

The light scattering in optical fiber has been reported in several analytical investigations [67, 68]. Chremmos *et al* have analysed light scattering by a chain of microbubbles in optical fiber [68]. For a specific size, increasing the number of microbubble in the chain increases the reflected power and decreases transmitted power around specific critical frequencies. The periodic perturbation by the chain of microbubbles can be modeled by grating theory. Increasing the size of the microbubble decreases the critical frequencies maximum of reflected power. Increasing the refractive index of the microbubble above that of the optical fiber ($n_m > n_1$) decreases the critical frequencies maximum of reflected power; while decreasing the refractive index of the microbubble below the optical fiber ($n_m < n_1$) increases reflected power.

3.2 Fabrication & Experimental Setup

In this section, the profile of the PCF and how the microbubble is formed is discussed.

3.2.1 Profile of Photonic Crystal Fiber

The experiments in Chapter 3 and 4 are carried out using an all-silica, index-guiding, multi-mode PCF from *Yangtze Optical Fibre & Cable Company* (YOFC), China, as shown in Figure 3(a).

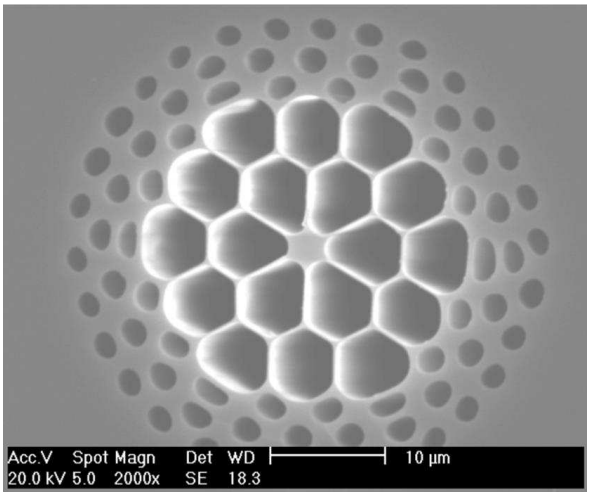

(a)

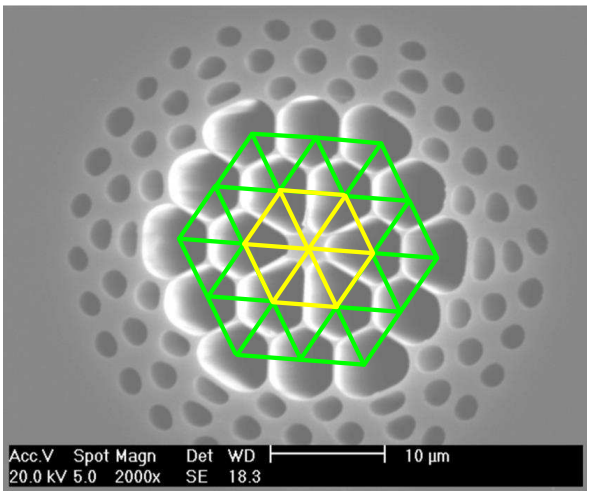

(b)

Figure 3: Scanning Electron Micrograph of the PCF. (a) Without and (b) with lattice guidelines for the first two rings of air holes. Image courtesy of YOFC.

The PCF's cladding is 125 µm. The core's diameter is 2.85 µm. The inner two rings and outer three rings have air hole diameters, 5.8 µm and 2.8 µm respectively. It can be observed that the first ring of air holes are arranged with six triangles in an asymmetrical hexagonal lattice. When the lattice is arranged with equilateral triangles, as illustrated in Figure 3(b) by the yellow triangles and all sides having the same length, it is generally known as hexagonal lattice. The PCF in Figure 3 has irregular air hole shapes beyond the first ring of air holes, which forms an asymmetric structure PCF. The green triangles illustrate the ideal centre position of the air holes for a hexagonal lattice. It can be seen that many of the air holes are not centred. In other words, when the triangle edges are centred to the air holes, it forms a scalene triangle that has all its

sides with different lengths. The scalene triangles have many patterns on all sides since no sides are equal.

3.2.2 Formation of Microbubble

The in-line microbubble PCF sensor is fabricated using the PCF shown in Figure 3 with a fusion splicer machine (FSM-40PM by *Fujikura*). The microbubble is formed at the splice region between the standard 125 µm cladding diameter SMF and the PCF with controlled splicing parameters. The microhole collapsing effect [5] is applied to fabricate the in-line microbubble PCF sensor. It is a delicate and novel technique to make a PCF sensor without the need of special vibration isolation table. The sensor can be fabricated very fast and the optical fiber strength is not compromised. The fabrication involves using a fusion splicer machine to splice a very short length (mm) of PCF to SMF.

The splicing settings need to be optimised to create the microbubble. The PCF in Figure 3 has an air filling fraction of 81.8%. Other hollow-core [53] and solid-core PCF [17] PCFs with large air-filling fraction, around 90%, can also form microbubbles. The microbubble that forms usually comes in two geometry shapes – circular or elliptical.

One microbubble is formed in each splice region after the fully collapse region. The shape of the cleaved fiber facets and the splicing process greatly influence

the microbubble formation. It affects its geometry and the likelihood of microbubble formation.

The arc time and arc power current resolution of the splicer machine are in the range of 10 ms and 0.01 mA respectively. Table 4 shows the key parameters set [55] in the setting of the fusion splicer machine.

Step #	Arc time (s)	Arc power (mA)	Offset (μm)	Number of times to arc
1	1	15.09	80	1
2	2	14.10	80	3

Table 4: Key parameters of the fusion splicer machine using the microhole collapsing effect technique [55].

The formation of a microbubble in splicing SMF and PCF takes several steps as shown in the sequence of photographs in Figure 4. The photographs are taken from the microscope image display of the fusion splicer machine.

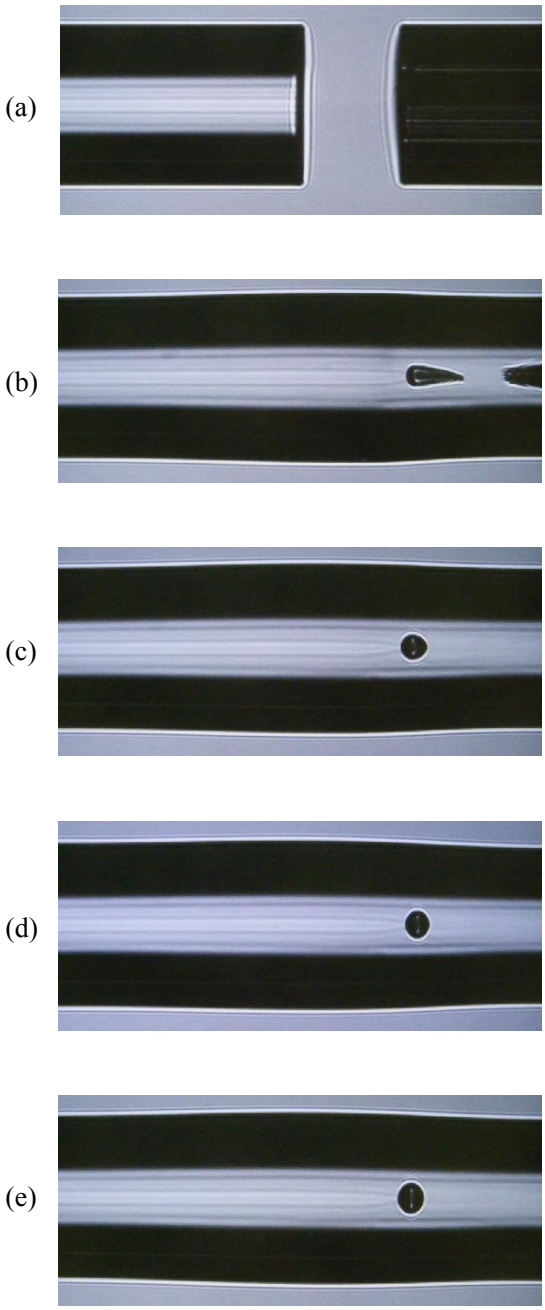

Figure 4: Microscopy images of the side views of the splicing joints between the PCF and the SMF. (a) Cleaved PCF on the left and SMF on the right. (b) After the first arc discharge. (c) 1, (d) 2 and (e) 3 weaker arc discharges are applied.

When the PCF and SMF are put into the fusion splicer machine, the microscope image display of the fusion splicer machine is blanked at first. After pressing the Set button, Figure 4(a) shows the cleaved end of the PCF on the left and SMF on the right for inspection. After pressing the Set button again, one arc discharge fuses the SMF and PCF together. The SMF-PCF is mechanically jointed. The process traps tiny air pocket at the splice region by completely collapsing a section of the PCF. A comet tail shaped air pocket is visible at the SMF-PCF interface in Figure 4(b).

The arc power is then reduced from 15.09 mA to 14.10 mA and three arc discharges are applied by repeatedly pressing the Arc button. As shown in Figure 4(c) to (e), the shape of the ellipse microbubble becomes rounder at the vertex during the three arc discharges [55]. The semi-major axis become narrower and the semi-minor axis become wider. The additional arc discharges are of lower power than the default SMF-SMF splice setting's rearc function [69]. Similar work using small solid core multimode PCF with high air filling ratio to form microbubble has also been demonstrated by Fan *et al*. [70]. The collapsed PCF structure during the splicing process traps air bubble inside the joint and three more arc discharges reshape their microbubble.

In the splicer settings there is also a parameter called "offset". It facilitates the control of air holes during microhole collapse by regulating the amount of heat applied to the PCF. The setting shifts the arc discharge position away from SMF-PCF interface towards the SMF side of the optical fiber by 80 μm

affecting the temperature distribution field along the longitudinal direction of the PCF. In contrast to previous report [5] with offset ranging from 205 to 255 μm, the shorter offset used here supply more heat to the PCF collapsing the air holes rapidly inside the PCF. The PCF has lower softening point than the SMF and with the right amount of heat via an optimised offset distance, air can be trapped inside the splice region in between the completely collapsed the PCF's air holes and the fused SMF. The microbubble formation is highly repeatable with the optimised splicer settings in Table 4.

Equally as important as the splicer setting is the cleave angle (θ) of SMF and PCF facet as shown in Figure 5(a). Microbubble size variation is also attributed to θ before the splice. It is found that for θ less than 2 ° microbubble is formed and for θ more than or equal 2 ° a microbubble of irregular shape and unpredictable size is formed.

A θ of 0 ° is an ideal case, where air gap between the SMF and PCF is equally spaced and uniform. So in practice, θ should be kept as small as possible to produce consistent microbubble.

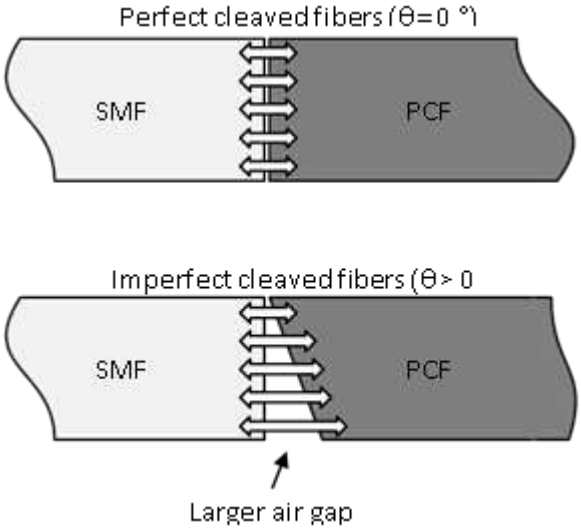

Figure 5: Illustration of imperfect cleaved Photonic Crystal Fiber (PCF) that creates a large air gap at the interface resulting variation of microbubble size. The white arrows indicate the relative distance to close the gap.

Assuming the arc discharge conditions can be applied identically all the time, the amount of air in the microbubble should be the same. Therefore, well-cleaved ends of the optical fibers will yield a repeatable, consistent shape and size of the microbubble.

On the other hand, if θ is more than 0 °, the condition will change as the separation distance between the SMF and PCF is different along the surfaces.

This leads to uncertainty when forming a microbubble. The melted fiber will need to close up a larger air gap and produce uneven shape at the splice joint forms, as shown in the bottom part of Figure 5. Examples of different cleave angle of PCF are shown in Figure 6. The size and shape of microbubbles are random and their transmission spectrums are generally a flat insertion loss spectrum, equivalent to a badly spliced optical fiber.

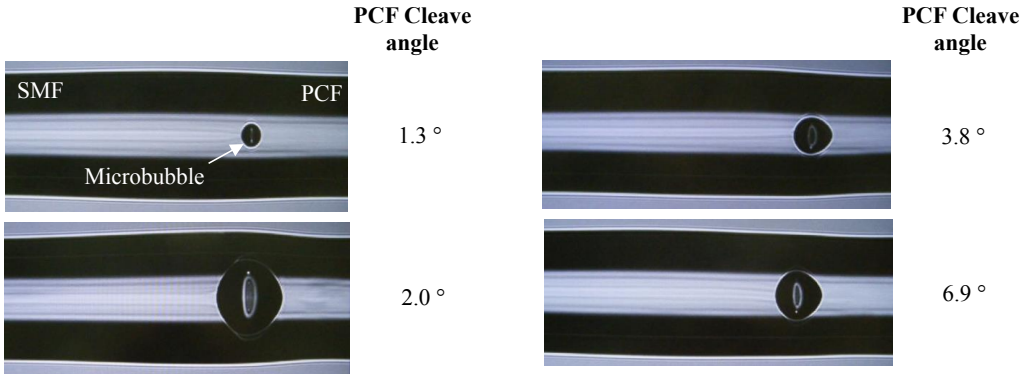

Figure 6: Microscopy images of the formation of microbubble at different cleave angle of the PCF.

Therefore during the fabrication process of the in-line microbubble PCF sensor, a well-cleaved fiber and optimised splicer settings are essential for consistent microbubble formation and repeatability. The discussion on insertion loss due to the splicing is discussed in 3.3.1 with the results.

3.3 Results

In the experiments, both ends of the PCF are spliced to an SMF applying the microhole collapsing effect technique. Figure 7 shows both sides of the spliced regions. One microbubble is visually seen in each splice region.

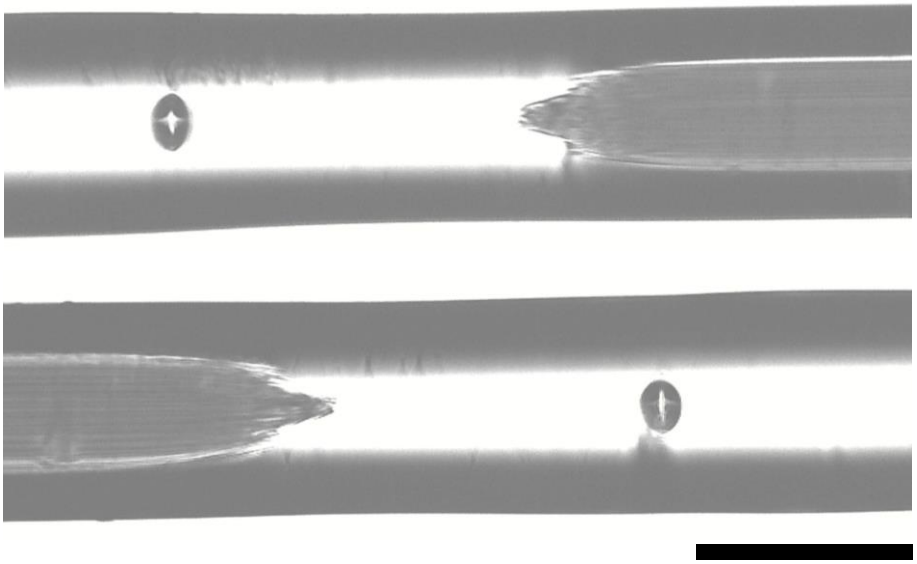

Figure 7: Microscopy images of one in-line microbubble PCF sensor at both end of the spliced region. The black scale bar shows 125 μm.

While fabricating the sensor at the second splice, the SMF-PCF-SMF is connected to a light source at one end and an Optical Spectrum Analyser (OSA) at the other

end. The equipment reveals the interference pattern generated, as shown in Figure 8.

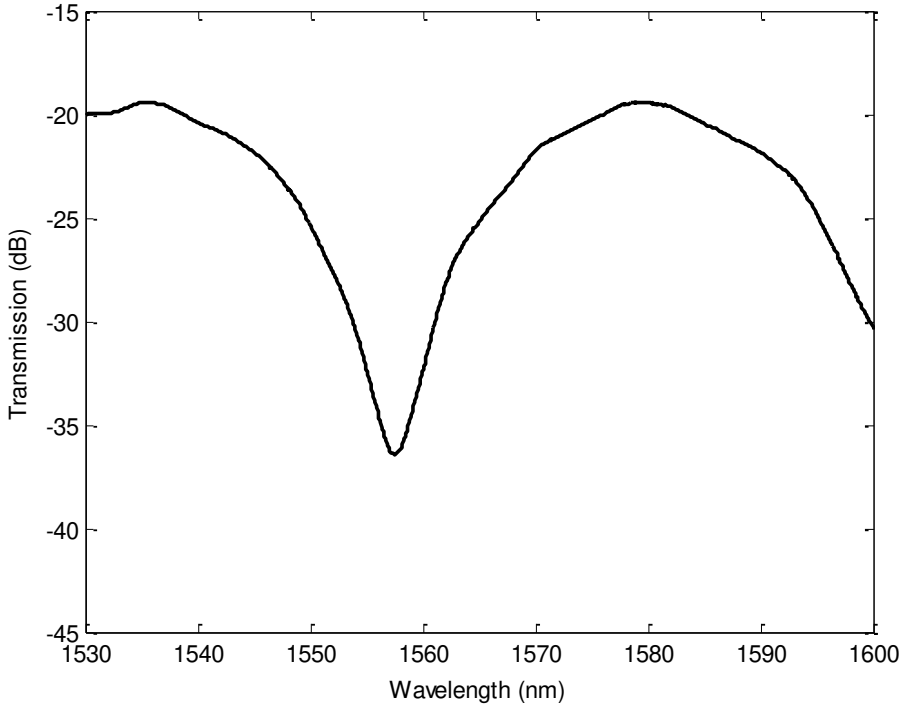

Figure 8: Interference fringe of the in-line microbubble Photonic Crystal Fiber (PCF) sensor.

A certain numbers of weak arc discharges is also applied. This process controls and slowly alters the geometry of the microbubble. The transmission spectrum of the device results from multiple mode interferences. The interference fringes show high contrast when the cladding modes are efficiently excited and become comparable to the core mode in intensity.

3.3.1 Optical Properties

The interference of the modes originates from the PCF-based all-fiber modal Mach-Zehnder interferometer [71]. The two microbubbles contribute to the interference and they have refractive indices lower than the optical fiber, which operate like two thick diverging lenses inside the device. Light that enters the first microbubble gets scattered by the two parabolic surfaces twice. The scattering effect excites higher-order modes in the fused region launching before into the PCF. The first scattering takes place at the SMF-air interface while the second scattering takes place at the air-PCF interface. The launched fundamental mode of the SMF, centered at the middle of the parabolic surface, is attenuated greatly by the scattering.

After the first microbubble, the fundamental and the scattered modes diffract in the fully collapsed region of the PCF. This diffraction excites many cladding and core modes into the PCF. A significant portion of light propagates as cladding modes, which results in the evanescent wave outside the PCF for refractive index sensing.

The evanescent wave interacts with the surrounding refractive index outside the cladding making it capable of detecting its ambient variation. The effective index of the cladding modes depend on the surrounding refractive index. Its evanescent wave should have travelled to the external surface of the PCF to interact with the surrounding environment. Since the core modes of the PCF are far away from the surrounding refractive index change, they will not

be modified. The different guided modes propagate at discrete speed inside the PCF and accumulate wavelength dependent phase differences.

The interaction of the modes can be described by a modified (1). Assuming two parallel waves are contributing to the interference [9], the spectra can be expressed as:

$$I_i = I_1 + I_2 + 2\sqrt{I_1 I_2}cos(\Delta\phi_i), \quad (16)$$

where I_1 and I_2 are the irradiance of the waves interfering with each other. $\Delta\phi$ is the phase difference between the two coupling modes travelling at different optical path length. i is the sensor designation for multiple sensors [9]. $\Delta\phi_i$ (in radian) is expressed as:

$$\Delta\phi_i = \frac{2\pi}{\lambda}\Delta n_i L_i + \Phi_i, \quad (17)$$

where L_i is the microbubble-to-microbubble distance. λ is the wavelength. Φ_i is the initial phase difference of the interfering waves. Δn is the effective index difference [9]. When light propagates in an optical fiber, the propagation constant is described as:

$$\beta = k\Delta n = \frac{2\pi}{\lambda}\Delta n,$$

where k is the wave number associated with the wavelength of the light.

The modes propagate inside the uncollapsed part of the PCF until the second fully collapse region of the PCF. It will then recombine the modes and travel

towards the second microbubble before being scattered again. Next, the SMF receives the interference pattern light and propagates by its fundamental mode to the OSA. The transmitted spectrum will show the interference pattern generated by the sensor.

For better understanding of the microbubbles on the insertion loss, the in-line microbubble PCF sensor is modelled using the RSoft simulation software as shown in refractive index profile of Figure 9.

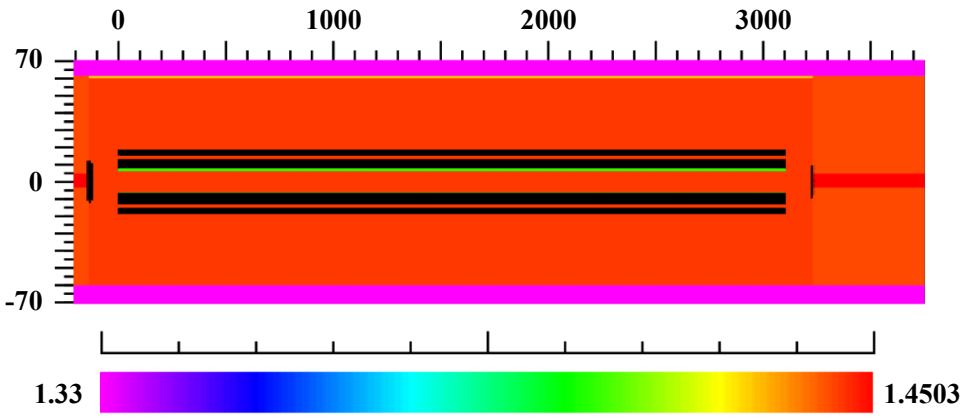

Figure 9: Refractive index profile of the simplified in-line microbubble PCF sensor from the RSoft simulation. The horizontal axis is the propagation z distance in µm. The vertical axis is the width of the device in µm.

For simplicity the partial collapsed region of the structure is omitted. The in-line microbubble PCF sensor's simplified model is submerged in water having refractive index of 1.33. Two microbubbles at $z = -150$ µm and $z = 3232.9$ µm containing air have refractive indices of 1.0. Single mode fiber light is launched into the model at the single mode fiber from $z = -198$µm. The beam propagation direction is in the z axis (horizontal axis, left-to-right direction).

The beam propagations of different combination of in-line microbubble PCF sensor with and without microbubbles are shown in Figure 10. The beam propagation of the simplified model of Figure 9, with two microbubbles [17], are shown in Figure 10(a). The structure exhibits strong scattering of light into the cladding after the first microbubble. There are multiple reflected beams resulted from the Fresnel reflection between the air-silica interfaces. As a result, there will be significantly more amount of light participating in the interaction with surrounding medium at the entire PCF length. At the second microbubble, it is not obvious to see the PCF's core light being scattered from the light already in the cladding.

Figure 10(b) shows the beam propagation without the second microbubble. The beam propagations between Figure 10(a) and Figure 10(b) are almost identical and do not show any change in light intensity except after z = 3232.9 µm without looking very closely.

In Figure 10(c), the first microbubble is removed while the second microbubble is still kept in the simulation. The beam propagation shows a

significant higher intensity of light is being propagated in the PCF's core region and significant lesser intensity of light is being transmitted in the cladding of the PCF. At z = 3100 µm, it is observed that the light from the PCF's core region diverges out into the cladding and gets reflected back at the optical fiber-air interface. The diverged light can be seen easily with lesser amount of light propagating in the cladding. At the second microbubble similar to Figure 10(a), it is not obvious to see any light being scattered by the second microbubble.

Figure 10(d) shows the beam propagation [17] without any microbubble in the structure. The beam propagation z < 3100 µm is identical to Figure 10(c). It can be seen that without the second microbubble, there is more light propagating near the core of the single mode fiber after z = 3232.9 µm.

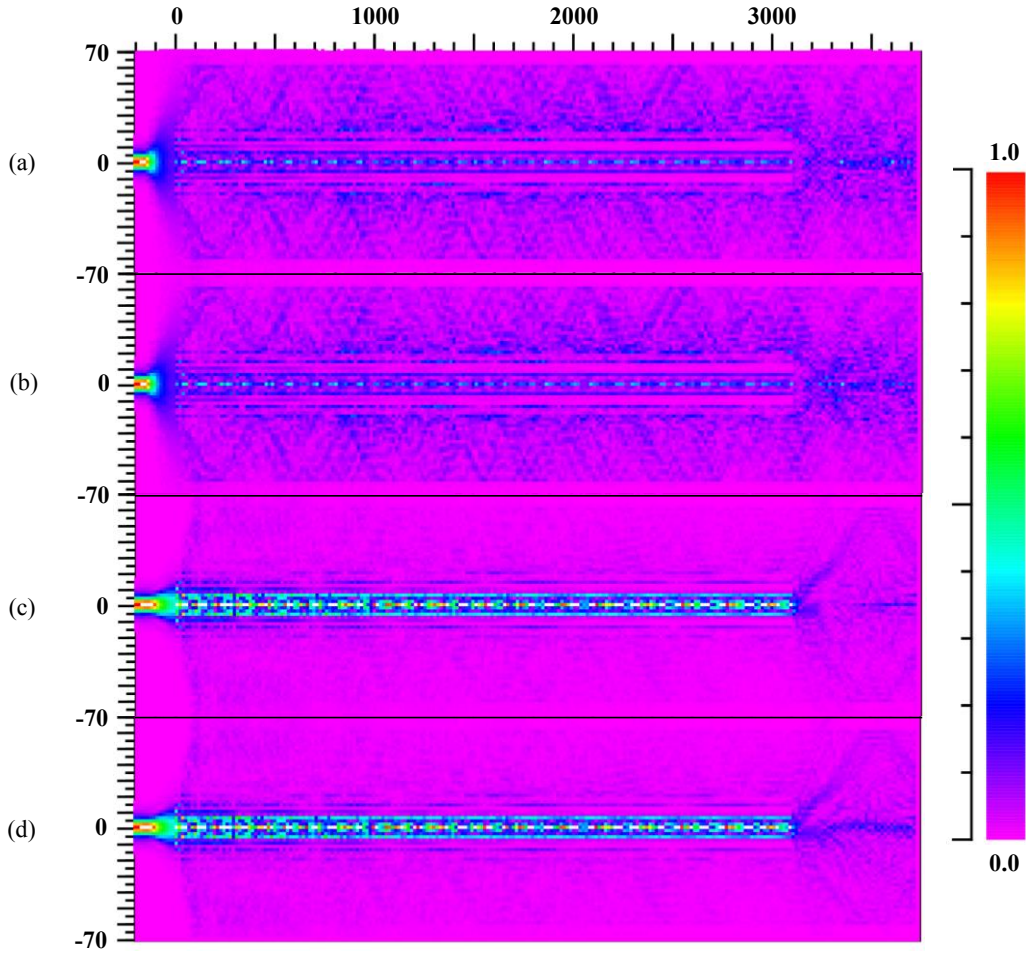

Figure 10: Beam propagations for (a) two microbubbles [17], (b) one microbubble at $z = -150$ µm, (c) one microbubble at $z = 3232.9$ µm, and (d) no microbubble [17] in the simplified model of the in-line microbubble PCF sensor. The horizontal axis is the propagation z distance in µm. The vertical axis is the width of the device in µm.

The power in the core of the single mode fiber at the end of the propagation length $z = 3741$ µm for Figure 10(a) to (d) are tabulated in Table 5. The results

show that the in-line microbubble PCF sensor suffers significant insertion loss in the range of ~20 dB with or without the microbubble. With the microbubble, the excitation of cladding mode contributes a significant portion of the insertion loss. In the absence of the microbubble, the insertion loss is attributed to the mode field diameter mismatch between different optical fibers.

Model	**Normalised Power**	
	(a.u.)	**(dB)**
Two microbubble	1.67×10^{-2}	−17.8
One microbubble at $z = -150$ µm	1.37×10^{-2}	−18.6
One microbubble at $z = 3232.9$ µm	4.62×10^{-3}	−23.4
No microbubble	1.43×10^{-2}	−18.4

Table 5: Power in the core of the single mode fiber from the beam propagation simulations at $z = 3741$ µm.

3.3.2 Mechanical Properties

The mechanical properties of Optical Fiber Sensors (OFS) have to be taken into account for many practical usages. Cleaning and reconditioning the external surface of the OFS, for example, is an essential process for biochemical OFS [72]. Chemicals and heat may be used to remove residue and/or sterilise the surface. Actions like pulling the optical fiber, or the presence strong current of the surrounding fluid cause the optical fiber to break

or suffer integrity issue. Most of the time, researchers encounter optical fiber breakage at the fabrication process already [73].

The in-line microbubble PCF sensor has an excellent mechanical structure. The outer cylindrical shape of the sensor resembles the appearance of any other stock optical fiber. It does not have any protruding form or construction that weakens the mechanical structure from its SMF-PCF fused design. When cleaning the in-line microbubble PCF sensor, one can hold one end of the sensor and use a clean wipe to wipe directly across the PCF region.

3.4 Summary

In concluding this chapter, we have introduced the background of PCF and reviewed the background, design and fabrication of the novel in-line microbubble PCF interferometric device. A PCF is used with single mode fiber to create the microbubble by trapping tiny air bubbles at the splice interface during the collapsing the PCF's air hole. The findings show that the in-line microbubble PCF sensor has an easy fabricating process, distinct light-fluid interaction and interference pattern, and mechanically strong structure. The formation of the microbubble is controlled by the various parameters in the PCF's air holes geometry, fusion splicer's settings, and cleaved optical fiber ends.

In another report, the air holes of PCF are pressurised during splicing to control the size. This method is useful for PCF that has the tendency to fully collapse without

forming a microbubble [5, 74, 75, 76]. In other words, the microbubble dimension depends on the pressure applied by adjusting the pressure into the air hole of the PCF. Figure 11 shows the pressurised setup [77]. However, it is obvious that this method is more complex as it requires more fabrication tools, possible debris entering the air holes, and is a single-side fabrication technique.

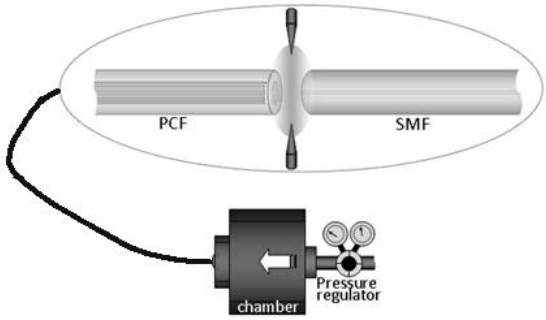

Figure 11: Illustration of the simplified pressurised fabrication setup from [77].

Another technique to form a microbubble in an optical fiber is normally found between a 'badly spliced' single mode fibers. In other words, microbubble is formed during the fusion arc process in the telecommunication industry.

Duan *et al* have demonstrated that an all optical fiber Fabry–Pérot interferometer (FPI) or etalon strain sensor using two ends of single mode fibers [78]. They firstly heated one end of the single mode fiber with arc discharge until a hemispherical tip

formed. Next they splice the hemispherical tip with another piece of well cleaved single mode fiber under axial stress, which will also form a microbubble by trapping air using surface tension. Additional rearc discharges are applied to reform the microbubble. The sinusoidal interference patterns [78], generated from the single mode fiber to single mode fiber splicing technique, indicate that either two or three interfering modes are present and similar sinusoidal interference patterns are also found in PCF formed modal interferometer [79]. For fiber optic sensing application utilising sinusoidal interference patterns, a common trade-off is between the sensitivity and maximum sensing range. The maximum sensing range is the period of the sinusoidal interference pattern, typically refers to as Free Spectral Range (FSR).

Ideally for a sensor, the FSR should be as large as possible and the interference pattern should shift as much as possible, which is its sensitivity. Zhang *et al* have also demonstrated a three-beam path PCF modal interferometer that shifts the sinusoidal-like interference pattern by at most 9.2 nm without being ambiguity. The maximum sensing range of the in-line microbubble PCF sensor's interference pattern, as shown in Figure 8, has the potential to shift at least 40 nm to the right without ambiguity.

4. Application of In-Line Microbubble Photonic Crystal Fiber Device

4.1 Introduction

In the fourth chapter, the in-line microbubble Photonic Crystal Fiber (PCF) sensor is applied for three sensing applications. Temperature and surrounding refractive index sensing are covered. Experimental procedures and results for the in-line microbubble PCF sensor are also discussed in detail in this chapter.

4.2 Experimental Setup

In this chapter, the sensors are fabricated using the same method, with one microbubble inside each of the single mode fiber (SMF)-PCF fused region, as described in the previous chapter. The sensor could be configured in either the transmission or reflective configuration. In the transmission configuration there are a total of two microbubbles in the fused regions, and in reflective configuration there is one microbubble in the fused regions. The thesis concentrates on the transmission configuration because it has a higher refractive index sensitivity than the reflective configuration.

4.2.1 Sensors Geometry

The in-line microbubble PCF sensors are fabricated according to 3.2.2, without pressurised air, and their dimensions are measured and tabulated in Table 1. A total of four sensors, namely as A, B, C, and D, are made and used in this Chapter. Their experimental setups are shown later in this chapter.

Geometric measurements	**Sensor A**	**Sensor B**	**Sensor C**	**Sensor D**
Microbubble-to-microbubble (L_{MM})	2810	3250	3000	3100
Microbubble, input (L_{MI})	24.6	22.6	24.1	17.8
Microbubble, input (W_{MI})	35.6	32.9	41.0	22.6
Microbubble, output (L_{MO})	18.2	24.3	29.5	24.2
Microbubble, output (W_{MO})	26.0	30.2	45.6	36.7
Fully Collapsed Region, input (L_{FI})	199	183	143	124
Fully Collapsed Region, output (L_{FO})	152	172	110	180

Table 6: Dimensions of the fabricated in-line microbubble PCF sensors. Unit in microns (μm).

Figure 12 illustrates the geometric measurements during the sizing. The PCF regions are separated into three regions – the unmodified PCF region (R_1), the partially collapsed PCF region (R_2) and the fully collapsed PCF region with one microbubble (R_3). Each sensor consist of two microbubble, two fully collapsed PCF regions, two partially collapsed PCF regions and one unmodified PCF region. It is worth mentioning that the PCF length, $L = L_{MM} + L_{MI} + L_{MO}$, is much shorter when compared to PCF interferometers reported by other groups [52, 54, 57, 80]. Microscopy images of Sensor A are shown in Figure 13.

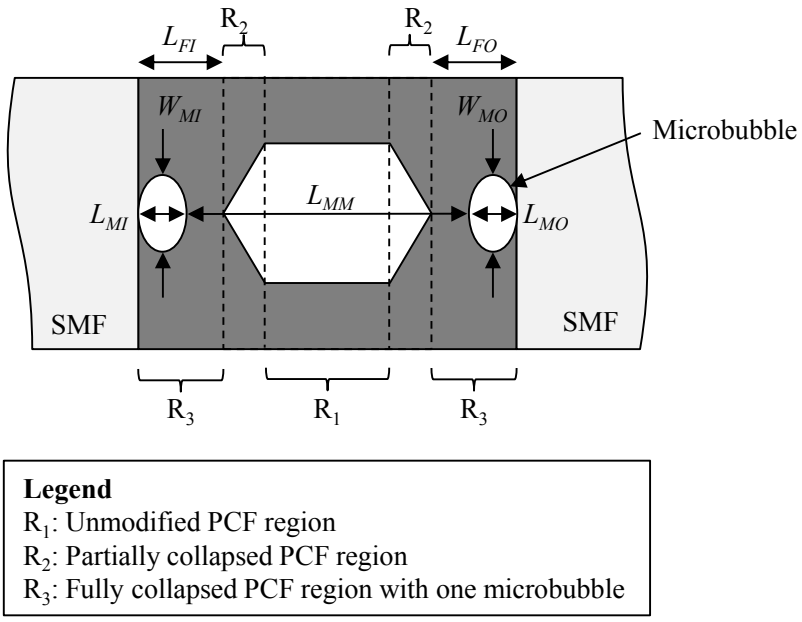

Figure 12: Illustration of the geometric measurements.

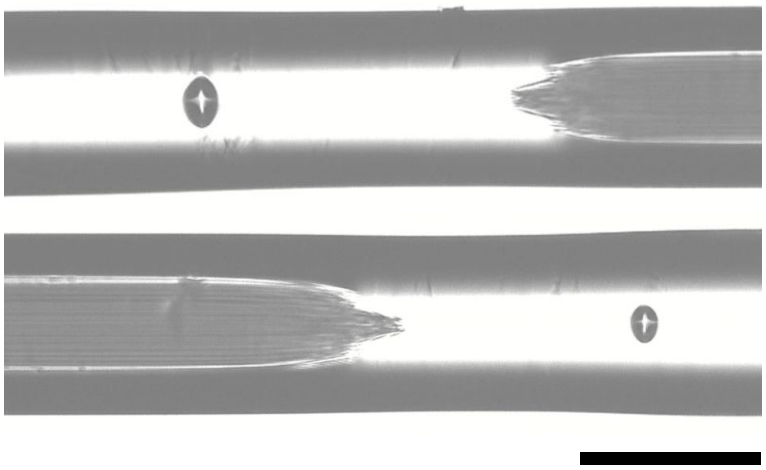

Figure 13: Microscopy images of the Sensor A at both end of the spliced region. The black scale bar shows 125 μm.

4.2.2 Configuration

In transmission configurations, the sensors are connected to a light source and Optical Spectrum Analyser (OSA), as illustrated in Figure 14.

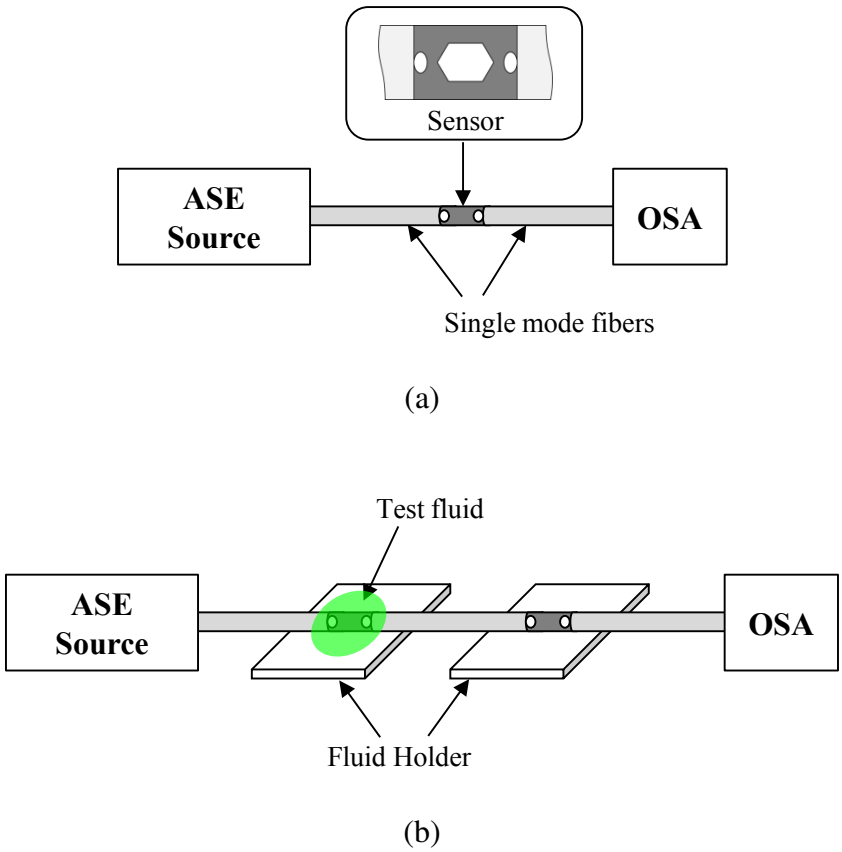

Figure 14: Measurement setup using the transmission configuration for (a) single sensor, and (b) two sensors in series, cascaded together.

A broadband Amplified Spontaneous Emission (ASE) light source is used to observe the resonance wavelength shift. ASE light sources are incoherent light sources with high intensity and broad spectrum. Other examples of incoherent light sources includes Light Emitting Diode (LED), superluminescent diodes (SLED or SLD) and halogen lamp. Another type of light source is the coherent light source, which include laser diode, HeNe laser, tunable laser, fiber laser, and femotosecond laser for fast modulation and switching. Coherent light

sources are comparatively more expensive, larger size and have a narrower wavelength range.

In the context of the thesis, the interference fringe of PCF sensors are tracked for sensing either refractive index or temperature. For incoherent light sources, such as ASE light source or SLED, provide wide wavelengths of light into the PCF sensor that can be measured by OSA. For certain coherent light source, such as the tunable laser, would provide the same means of detecting the transmission by sweeping the light across a range of wavelengths and measuring the light intensity with a photodiode.

In the reflection configuration, the technique discussed in 3.2.2 to form microbubbles in the sensor modified. After forming the first microbubble, the microhole collapsing effect is applied to the other end of the PCF without a single mode fiber, the PCF collapses and forms a single-end type of Optical Fiber Sensor (OFS) as shown in Figure 15 [56].

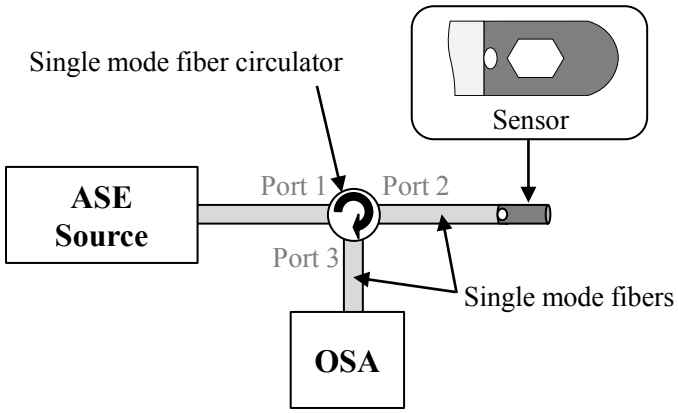

Figure 15: Measurement setup using the reflection configuration with one sensor.

The interference pattern generated from the reflection configuration, as shown in Figure 16, differs from the transmission configuration in Figure 8. This is due to the fact that the OFS operates by the Fabry–Pérot effect with multiple cavities. The setup works like the Michelson interferometer with multi-bean interference. When light traveling from the single mode fiber reaches the microbubble, the core mode get diffracted and excited into the cladding modes. The modes propagate through the PCF and reflect back in the reverse direction at the tip of the sensor. The hemispherical tip is formed when all the air holes collapse during microhole collapsing effect.

The cladding modes creates evanescent wave outside the PCF and changes its effective index according to the surrounding refractive index. When the core and cladding modes reach back to the microbubble, the beams combine

together with a phase difference. The microbubble in the sensor forms a Fabry–Pérot cavity that creates a sinusoidal interference pattern.

Together, the Fabry–Pérot effect and Michelson interferometer forms the large sinusoidal interference pattern and small fringe interference pattern shown in Figure 16 respectively. The small fringes shift to higher wavelength when the sensor is subject to a higher surrounding refractive index and shift to lower wavelength when the sensor is subject to a lower surrounding refractive index. When the sensor is placed inside a high refractive index such as glycerine, all the small fringes disappear leaving only the large sinusoidal interference pattern. The reflection configuration has a refractive index sensitivity of 11.5 nm/ RIU over a refractive index range of 1.33 to 1.34 and theoretical refractive index resolution of 1.74×10^{-3} when using a wavelength accuracy of 20 pm.

There are many other established techniques, such as Fabry–Pérot [81] and FBG [82], to modify PCF for sensing refractive index in the reflection configuration. In general, PCF is made of single material, silica, which exhibits very low temperature sensitivity when compared with conventional single mode fiber because of low thermal expansion coefficient. The in-line microbubble in the reflection configuration demonstrates another way to use intermodal interference for sensing refractive index.

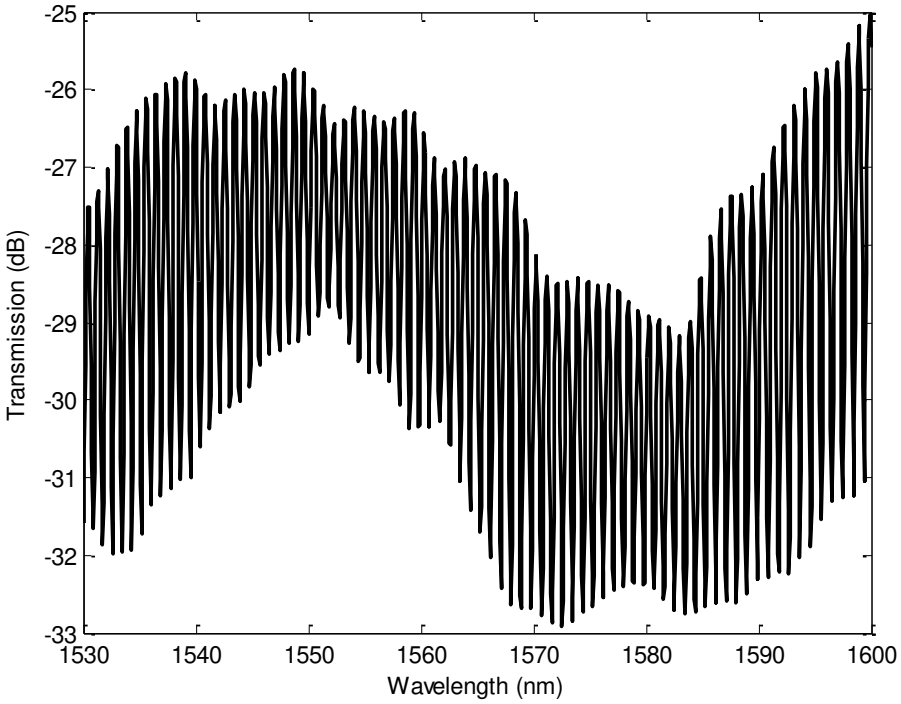

Figure 16: Interference pattern generated from the reflection configuration.

4.3 Result and Discussion

The results are described and discussed in this section. For the first application, two in-line microbubble PCF sensors, Sensor A and B, are used to investigate the feasibility to connect multiple sensors together to simultaneously sense two refractive index liquids [55]. For the second application, Sensor C is cascaded to a Long Period Grating (LPG) to investigate the temperature and refractive index response [20]. Simultaneous measurement of temperature and the surrounding refractive index are obtained by this configuration. Both of their resonance wavelengths are chosen so that they are distinguishable and will not cross one

another during the calibration process. For the third application, Sensor D is used to conduct the bioaffinity experiment [17].

4.3.1 Cascaded Refractive Index Sensor

The ability to multiplex sensors significantly reduces the cost and complexity of the sensor array. However, many works have encountered a common setback, their interference patterns have overlapping peaks-or-dips or have changed patterns. A successful multiplexed sensor has been reported [52] however the performance is still incomparable to the FBG sensor array that has several hundreds or even thousands of sensing points.

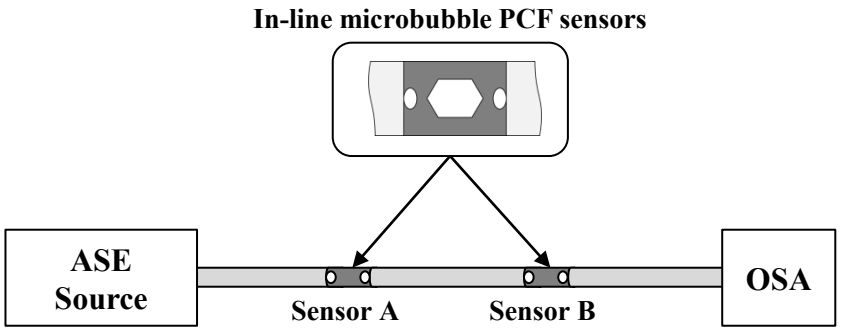

Figure 17: Experimental setup for the cascaded refractive index sensors.

The experimental setup for the cascaded refractive index sensors is presented in Figure 17. Two pieces of in-line microbubble PCF sensors, Sensor A and B,

are cascaded in series to investigate their interference pattern change due to a change in refractive index. The transmission is measured using an ASE light source and OSA. The measured spectrums of Sensor A and B are plotted in Figure 18 from 1530 nm to 1600 nm. Sensor A, denoted by the solid black line, shows two dips at 1546 nm and 1590 nm. Sensor B, denoted by the solid blue line, exhibits one dip at 1557 nm.

The measured transmission spectrum, I_{t}, is fitted into the modified model from (16). From the equation the interference pattern, I_A, of Sensor A is expressed as:

$$I_A = I_1 + I_2 + 2\sqrt{I_1 I_2}cos\left[\frac{2\pi\Delta n_A}{\lambda}L_A + \Phi_A\right] + I_{\mathrm{loss}}, \tag{18}$$

where $I_1 = 1.0$, $I_2 = 0.6,\ \Delta n_A = 0.0195,\ L_A = 2.81\mathrm{e}^{-3}, \Phi_{\mathrm{A}} = \ 0.3456.$

Likewise for interference pattern, I_B, of Sensor B is expressed as:

$$I_B = I_1 + I_2 + 2\sqrt{I_1 I_2}cos\left[\frac{2\pi\Delta n_B}{\lambda}L_B + \Phi_B\right] + I_{\mathrm{loss}}, \tag{19}$$

where $I_1 = 1.0$, $I_2 = 0.6,\ \Delta n_B = 0.0165,\ L_B = 3.25\mathrm{e}^{-3}, \Phi_{\mathrm{B}} = \ 0.4398.$

Another 20 dB insertion loss, $I_{\text{loss}} = -20$, is included in the each of the calculation before plotting the calculated spectrum with dashed lines in Figure 18:

$$I_{\text{t}} = I_A + I_B. \tag{20}$$

The inclusion of insertion loss is due to the loss mechanisms in the excited fiber modes in the fully collapse region, the Fresnel reflection and refraction at the optical fiber cladding and surrounding refractive index region after the microbubble, and the scattering losses at the microbubble's interfaces as described in 3.3.1 on Page 47. The microbubbles are necessary to excite higher order cladding modes into the PCF cladding evanescent wave for interaction with the surrounding refractive index.

For Sensor B, it can be seen that the simulated and measured spectrum overlay each other closely. However for Sensor A, it can be observed that there is larger deviation between the simulated and measured spectrum. The reasons for the deviation could come from the simplified assumption that only two waves are involved in generating the interference pattern.

Next, Sensor A and B are cascaded and measured in de-ionised water (refractive index = 1.3323), as shown in Figure 19. The resonance wavelengths of the dips match the individual measurement, namely at 1546 nm, 1557 nm and 1590 nm. It can be seen that the 1557 nm dip of Sensor B is attenuated 3 dB more than the two dips due to the broadening effect of the dip at 1546 nm.

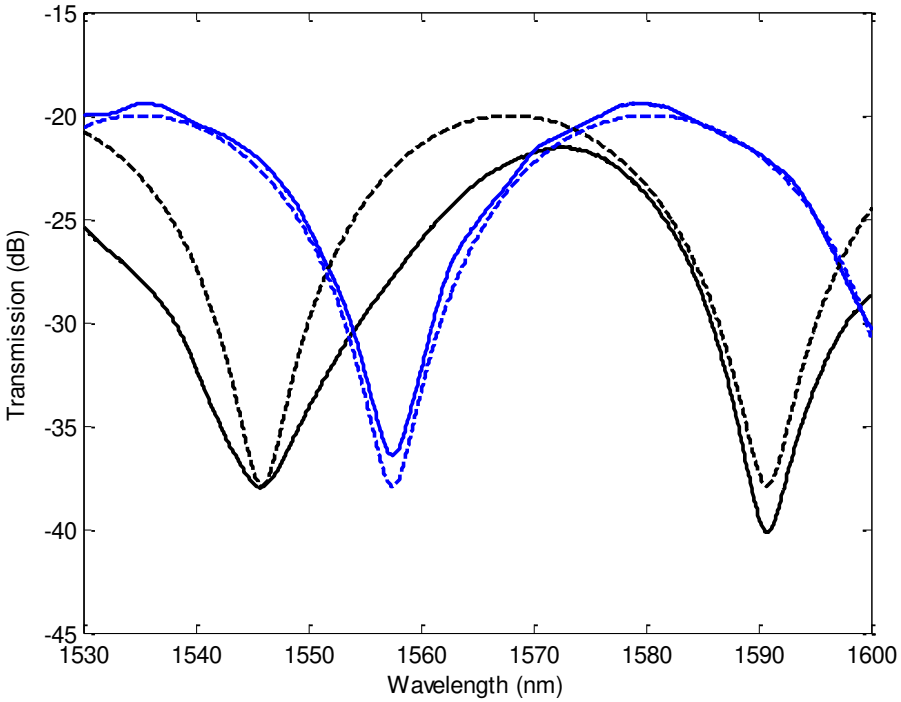

Figure 18: Individual measured (solid lines) and calculated (dashed lines) spectrum of Sensor A (black lines) and B (blue lines). The devices are submerged in de-ionised water at 24 °C.

The dip at 1546 nm is also levelled due to its close proximity to the decreasing slope of Sensor B interference spectrum. The dashed line in Figure 19 shows the simulated spectrum for the cascaded devices by summing up (2) for Sensor A and B.

The two in-line microbubble PCF sensors are distanced around 50 cm apart during the splice to facilitate easy handling during calibration later. The splices are performed on the leading SMF. Different lengths of SMF in between the

two sensors do not affect the shape of interference pattern generated and only slight attenuation loss is observed when extremely long SMF are used.

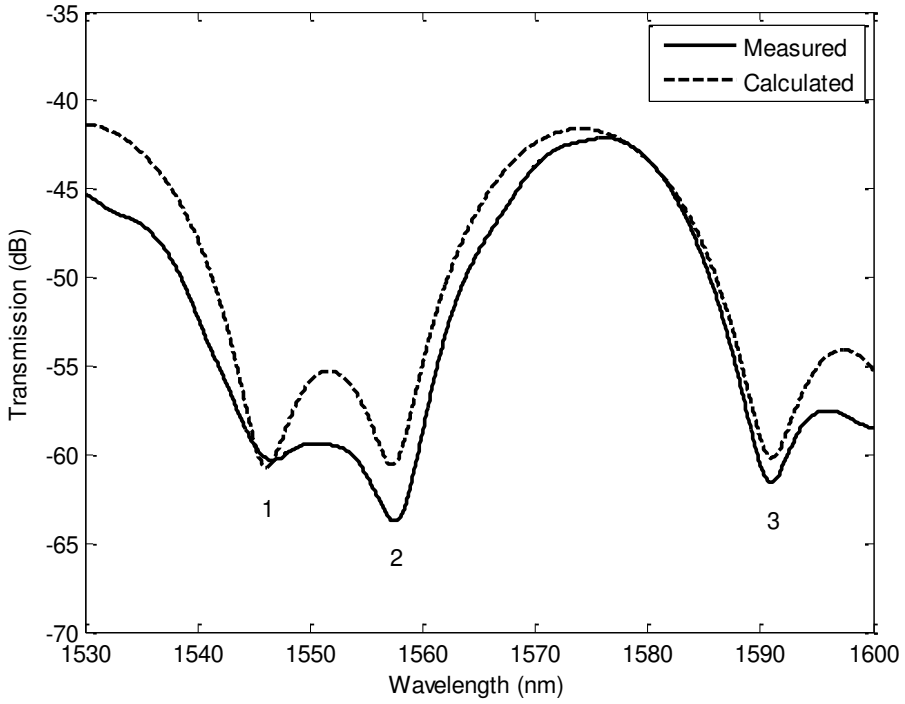

Figure 19: Measured (solid line) and calculated (dashed line) spectrum of the cascaded Sensor A and B. The devices are submerged in de-ionised water at 24 °C.

Refractive index sensing is carried out by immersing one in-line microbubble PCF sensor in different refractive index liquid while the other in-line microbubble PCF sensor is kept in de-ionised water, which has constant

refractive index. The refractive index liquid, Test Fluid, is a mixture of different concentration of glycerin (Certified ACS by *Fisher Scientific*) in de-ionised water. A refractometer (r2 mini by *Reichert*) with a refractive index accuracy of 2×10^{-4} is used to measures the refractive index. Refractive indices from 1.3323 to 1.3751 are mixed for the experiments.

Any trace of the Test Fluid is cleaned off properly in between any measurement with 2-propanol. Firstly, this measurement demonstrates simultaneous refractive index measurement using cascaded in-line microbubble PCF sensors. This means that two refractive index liquid can be measured at the same time. Secondly, the measurement also examines and evaluates the cross-talk between the two in-line microbubble PCF sensors affecting the dips.

For the clarity of discussion, the dips are numbered, #1, #2, and #3, according to their spectral position from the left to the right, as shown in Figure 20. In the first simultaneous refractive index measurement, Sensor A is immersed in different refractive index liquids while Sensor B is immersed in de-ionised water. It can be observed that in Figure 20 dip #3 preserves its shape when moving towards the longer wavelength as the refractive index of the Test Fluid increases. In contrast, the shape of dip #1 slowly becomes undifferentiated as it move closer to dip #2. Dip #2 is attenuated more and more as dip #1 shift.

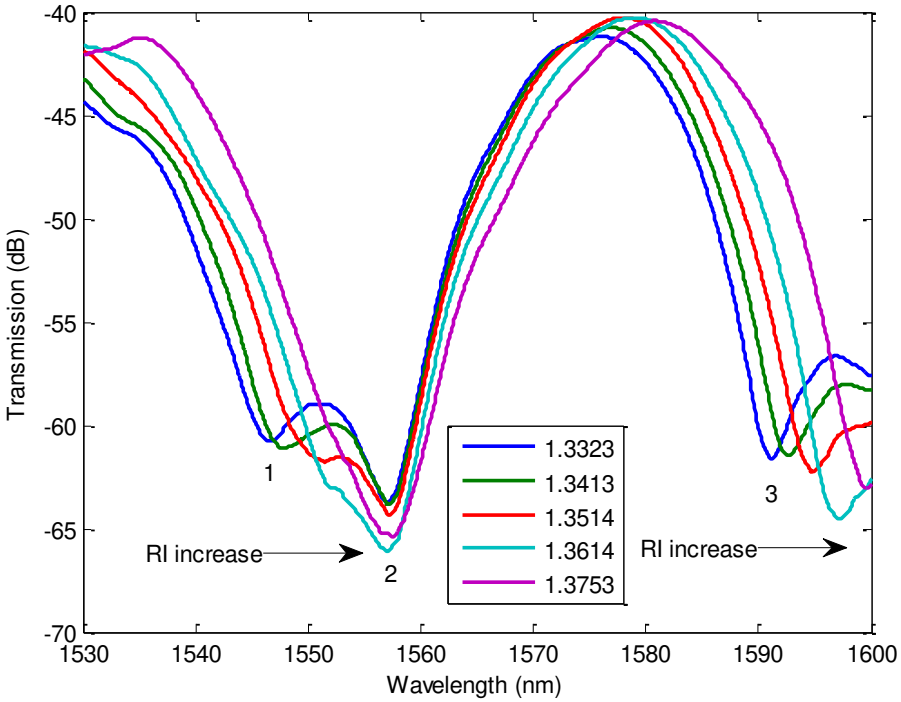

Figure 20: Measured spectrum of cascaded refractive index sensors when Sensor A is being tested. Black arrow indicates the direction the dips shifted as refractive index increases. While Sensor A is in test, Sensor B is kept constant refractive index by submerging it in de-ionised water.

The resonance wavelengths of Figure 20 are tracked as a function of changes in refractive index, and depicted in Figure 21. The corresponding refractive index sensitivity for dip #1 and dip #3 are 252 nm/ RIU and 207 nm/ RIU respectively.

When taking into account the OSA's wavelength accuracy of 20 pm, one can derive the theoretical sensitivity to be 7.94×10^{-5} RIU. The theoretical

sensitivity supports the device measurement accuracy to the commercial refractometer 2×10^{-4} used to calibrate the Test Fluid. Meanwhile, dip #2 displays a level refractive index response with 8.95 nm/ RIU.

One last observation is that all the data points, as shown in Figure 21, fit the linear regression lines, which is essential for practical usage.

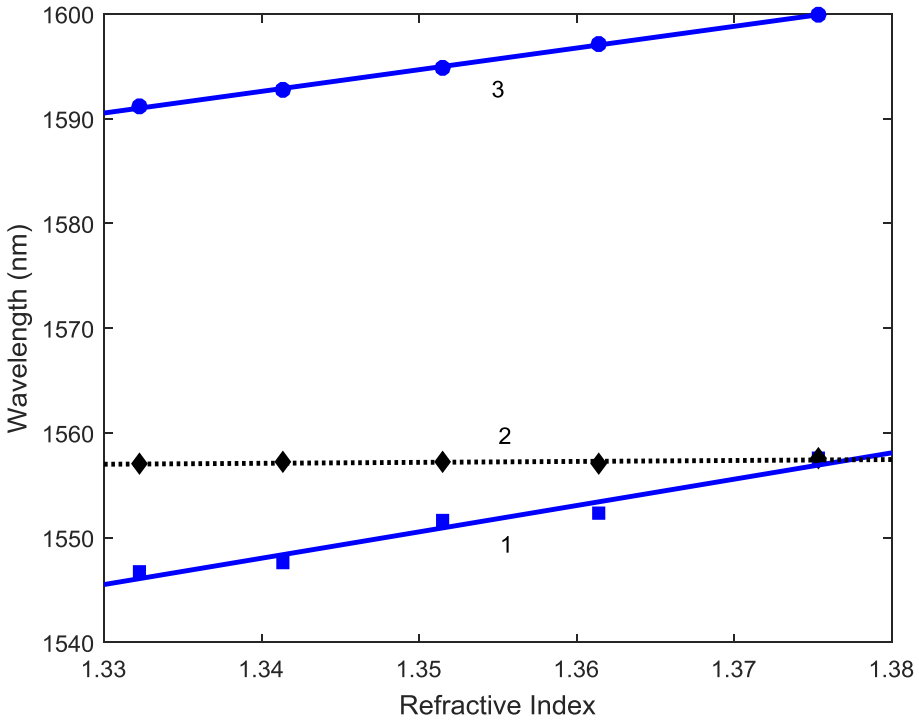

Figure 21: The three numbered dips in Figure 20 are tracked and plotted. The square, diamond and circle symbol represent dip #1, #2 and #3 respectively. The blue lines indicate the Sensor A in test, while the black lines indicate Sensor B in de-ionised water as control.

In the second simultaneous refractive index measurement, Sensor B is immersed in different refractive index liquids while Sensor A is immersed in de-ionised water, as shown in Figure 22. Dip #2 shifts to longer wavelength as the test refractive index increases. The dips in Sensor A have a barely noticeable wavelength shift. However, it can be seen that there is lesser attenuation as the refractive index of the Test Fluid increases.

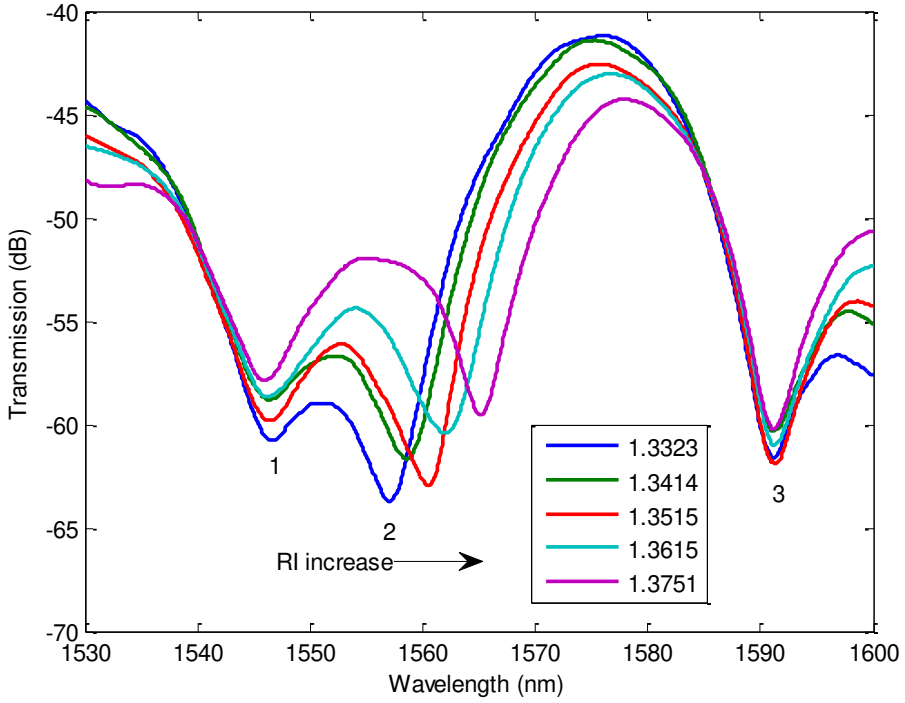

Figure 22: Measured spectrum of the cascaded refractive index sensors when Sensor B is being tested. Black arrows indicate the direction the dips shifted as refractive index increases. While Sensor B is in test, Sensor A is kept constant refractive index by submerging it in de-ionised water.

Likewise for the second simultaneous refractive index measurement, the dips in Figure 22 are tracked as a function of changes in refractive index, and depicted in Figure 23. Dip #2 displays similar refractive index response of 187 nm/ RIU. The control dip #1 and #3 displays 13.5 nm/ RIU and 0.295 nm/ RIU respectively. The linear regression lines are also well fitted.

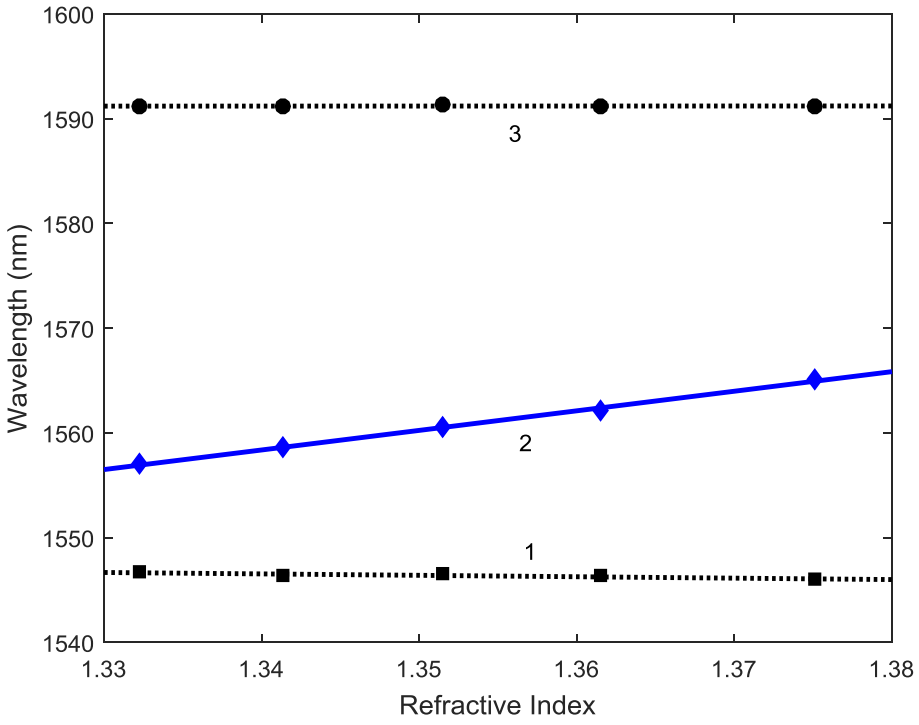

Figure 23: The three numbered dips in Figure 22 are tracked and plotted. The square, diamond and circle symbol represent dip #1, #2 and #3 respectively. The blue lines indicate the Sensor B in test, while the black lines indicate Sensor A in de-ionised water as control.

Comparing the results between the two simultaneous refractive index measurements, clearly it is shown that the first measurement has close proximity of two sensing dip, namely dip #1 and #2. The two resonance wavelengths become 'overlapped' and become difficult to distinguish individually. This imposes a problem if the dynamic refractive index sensing range comes close to or exceeds +15 nm as shown in Figure 20.

In contrast, the second measurement shows a better measurement. Dip #2 has a large dynamic refractive index sensing range that does not affect the other dips. All three dips have influential effects in term of crosstalk between the two simultaneous refractive index measurements. The crosstalks are plotted in Figure 24.

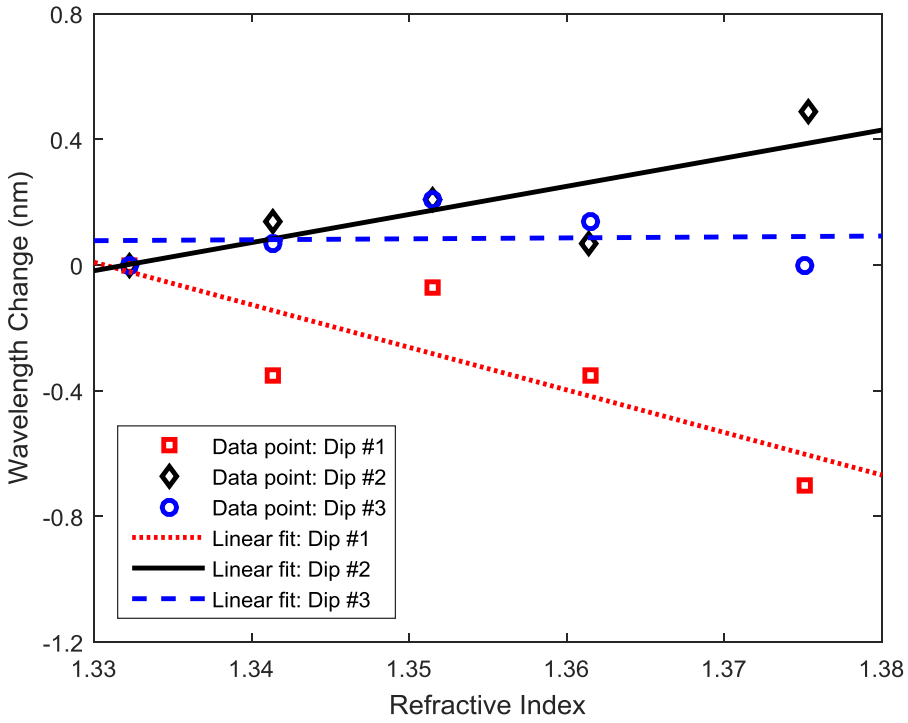

Figure 24: Wavelength shift as a function of refractive index change for the controls in the two simultaneous refractive index measurements. Red colour represents the second measurement's dip #1. Black colour represents the first measurement's dip #2. Blue colour presents the second measurement's dip #3. The straight lines are the linear regression lines for the experimental data points.

The position and shape of dips influence amount of crosstalk when sensing. When the dips are closely together and have broad dip profile, the crosstalk increases. When the dips are far apart and have a narrow dip profile, the crosstalk is reduced significantly.

The crosstalk will accumulate as more and more sensors are cascaded together. Regular filter cannot eliminate the crosstalk as it originates from the optical property of the in-line microbubble PCF sensor. Therefore, the individual sensor has to be chosen prudently with narrow dip profile, and have sufficient spectral separation of the resonance dips to other sensors. In the case of the example in this section, dip #2 and dip #3 are the most optimal resonance wavelength to be traced for two simultaneous refractive index measurement.

When the refractive index of the Test Fluid changes at either one of the test sensors, the corresponding test sensor's dip will shift. The sensor's dips that is being tested will shift to higher wavelength when the Test Fluid's refractive index increases. Likewise, when the Test Fluid's refractive index decreases, only the test sensor's dips will shift to lower wavelength. All the dips do not shift left or right entirely together when both Test Fluids do not change together at the same value refractive index. The changes in the refractive index of the Test Fluid also changes the peak of the spectrum. However it can been seen that in Figure 20 and Figure 22 all the peaks shifted to higher wavelength when the refractive index increases. For any change in refractive index around the cascaded refractive index sensors, the peaks would not be differentiable and trackable to find the relationship between the resonance wavelengths with the refractive indices.

Besides tracking the dips and peaks to find the relationship between the resonance wavelengths with the refractive indices, Rindorf *et al.* tracked their

sensor's dip using Full-Width Half-Maximum (FWHM) [21]. From Figure 20, the FWHM scheme will not be applicable for the measured spectrum of the cascaded refractive index sensors because dip #1 has less than 3 dB difference between its minimal and the maximal.

4.3.2 Dual Parameter Sensor

Sensor C is used to perform the second experiment in this chapter. The experimental setup is presented in Figure 25. One in-line microbubble PCF sensor, Sensor C, and one LPG is cascaded in series to investigate their interference pattern change due to a change in refractive index and temperature.

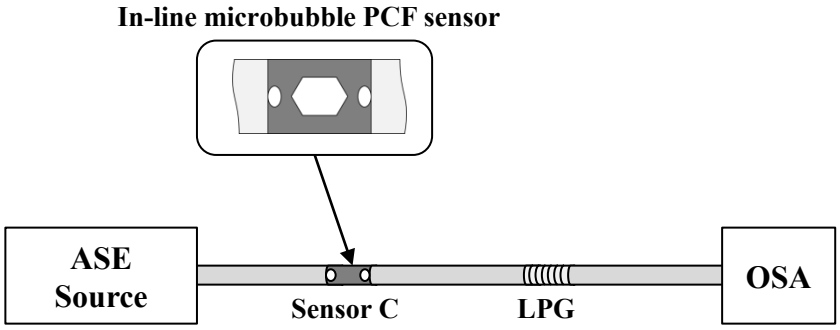

Figure 25: Experimental setup for the dual parameter sensor.

The in-line microbubble PCF sensor's resonance wavelength is at 1513 nm, as depicted by the blue line in Figure 26. One 30 mm LPG sensor was cascaded

in series together with Sensor C as shown by the black line in Figure 26. The LPG is produced by the point-by-point grating writing technique using a 248 nm wavelength Excimer laser on a hydrogen-loaded SMF. Its grating period is 455 μm and resonance wavelength is 1546.3 nm at −15 dB, as shown by the red line in Figure 26.

The cascaded sensors, the LPG and in-line microbubble PCF sensor, shows two distinctive dips at two resonance wavelengths in the transmission spectrum. They are chosen at that particular resonance wavelength so that they will be distinguishable during the refractive index sensing and do not 'overlap' one another.

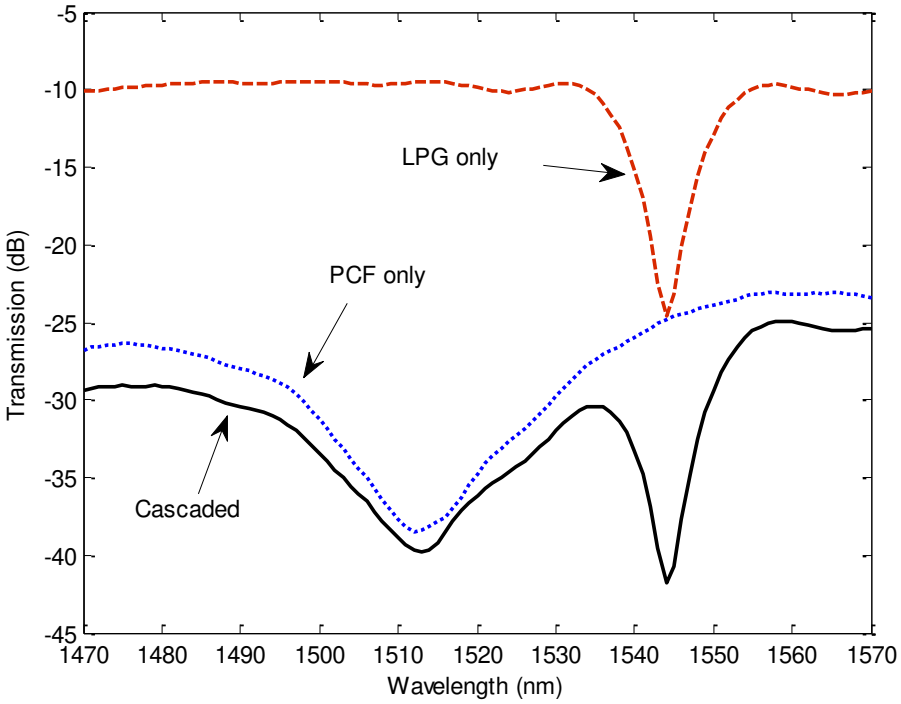

Figure 26: Measured spectrum of the in-line microbubble PCF sensor (blue dotted line), the LPG (red dashed line), and the cascaded device (black solid line). All the devices are submerged in de-ionised water at 24 °C.

The refractive index sensing is performed by immersing one device at a time to different refractive index liquid while keeping the other in de-ionised water. After one device has completed the refractive index calibration, it is kept in de-ionised water and the other is calibrated. The cascaded sensors exhibit distinctive refractive index responses. In Figure 27, as the refractive index of the surrounding increases, the LPG resonance wavelength at 1546 nm shifts towards shorter wavelengths. On the other hand, the resonance wavelength of the in-line microbubble PCF sensor

shifts towards longer wavelengths. Linear fitting is applied to obtain the refractive index sensitivity coefficient. The in-line microbubble PCF sensor and LPG exhibit 171.96 nm/ RIU and −30.82 nm/ RIU respectively. The LPG used has the typical refractive index response but has shorter length than the typical 68 to 85 mm [83].

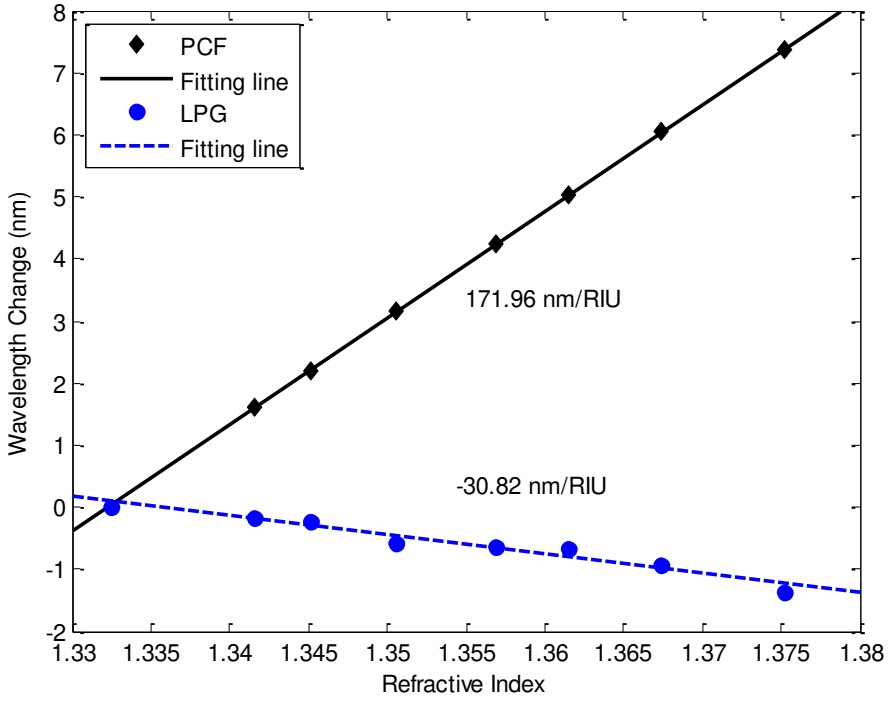

Figure 27: Refractive index response of the resonant wavelengths. PCF denotes the in-line microbubble PCF sensor; LPG denotes the Long Period Grating (LPG). Symbols represent the experimental data and the straight lines represent its linear fitting.

PCFs have excellent temperature stability and a low thermo-optics coefficient, and are not easily affected by temperature changes [50, 52, 54, 53, 57]. Experiments for sensing should be carried out in a temperature stable area where there is as little temperature variation as possible to reduce any thermal effect on the measurement. The experiments in this thesis were conducted in this manner.

The laboratory thermometers reading shows that the air temperature has a fluctuation of less than 0.1 °C, making temperature drift negligible [20]. The refractometer also has automatic temperature compensation and the refractive index is checked prior to each refractive index measurement to ensure reliable measurements.

The cascaded sensors are placed into an oven to calibrate its thermal responses. The oven controls the internal temperature from 25 to 100 °C with 0.1 °C step. Figure 28 plots the LPG and in-line microbubble PCF sensor temperature response. Both LPG and in-line microbubble PCF sensor resonance wavelengths move toward the longer wavelengths linearly as temperature increases. The temperature sensitivity of the LPG 47.4 pm/ °C is higher than the in-line microbubble PCF sensor 10.4 pm/ °C. The latter is the typical temperature response of pure silica based PCF sensors.

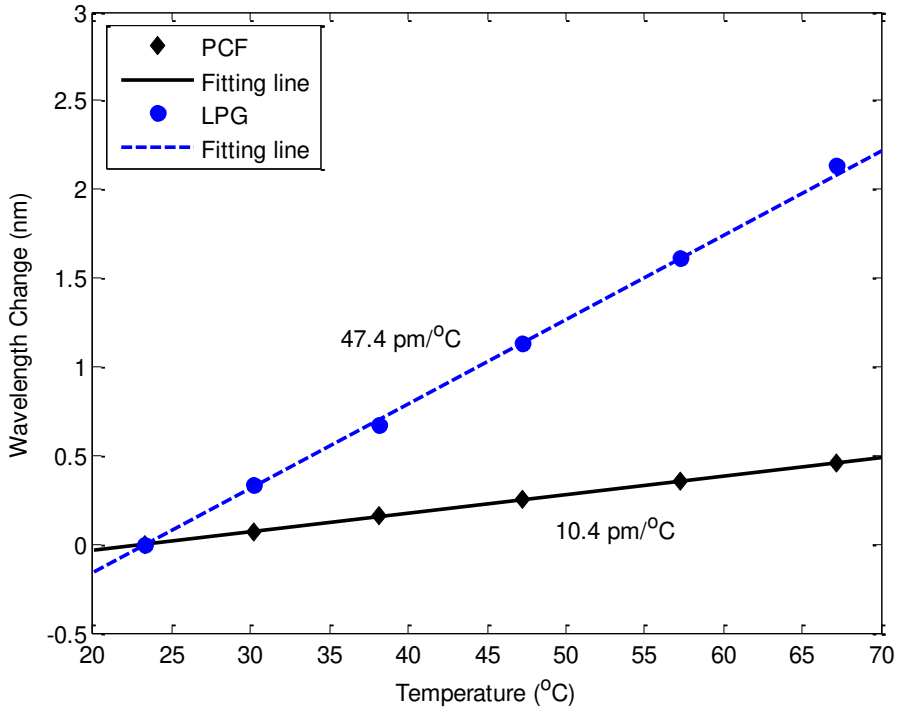

Figure 28: Temperature response of the resonant wavelengths. PCF denotes the in-line microbubble PCF sensor; LPG denotes the Long Period Grating. Symbols represent the experimental data and the straight lines represent its linear fitting.

Measurement results from the refractive index and temperature sensing can be put into a Sensor Matrix [20]:

$$\begin{bmatrix} \delta n \\ \delta T \end{bmatrix} = \begin{bmatrix} 171.96(\text{nm/ RIU}) & 10.4\times10^{-3}(\text{nm/ ℃}) \\ -30.82(\text{nm/ RIU}) & 47.4\times10^{-3}(\text{nm/ ℃}) \end{bmatrix}^{-1} \times \begin{bmatrix} \delta\ \lambda_{\text{PCF}} \\ \delta\ \lambda_{\text{LPG}} \end{bmatrix}, \quad (21)$$

where δn is the variation in refractive index, δT is the variation in temperature, $\delta\ \lambda_{\text{PCF}}$ is the variation in resonance wavelength of the in-line

microbubble PCF sensor and $\delta \lambda_{LPG}$ is the variation in resonance wavelength of the LPG.

Simultaneous refractive index and temperature sensing can be achieved when the LPG and in-line microbubble PCF sensor responds linearly. The Sensor Matrix's precision is experimentally validated in the next page.

The cascaded sensors are put into the same de-ionised water at the same time. Next, the oven heats it from room temperature, and oven's temperature reading is recorded. The logged temperatures are 31.2 °C, 32.4 °C, 36.9 °C, 39.8 °C, 44.6 °C, 48.0 °C, and 53.7 °C. 31.2 °C is set as the initial temperature for reference and comparison.

The measurement results are applied to the Sensor Matrix and plotted in Figure 29. The diagonal solid line, from top right to bottom left, represents the ideal situation where the applied temperature change and the measured temperature change are identical. In other words, the perfect case is when there is a change in the applied temperature; the change in measured temperature is of the same value along the diagonal line. The Sensor Matrix's data points, in black circle, are in close proximity to the perfect case demonstrating that the results agree well with actual temperature change.

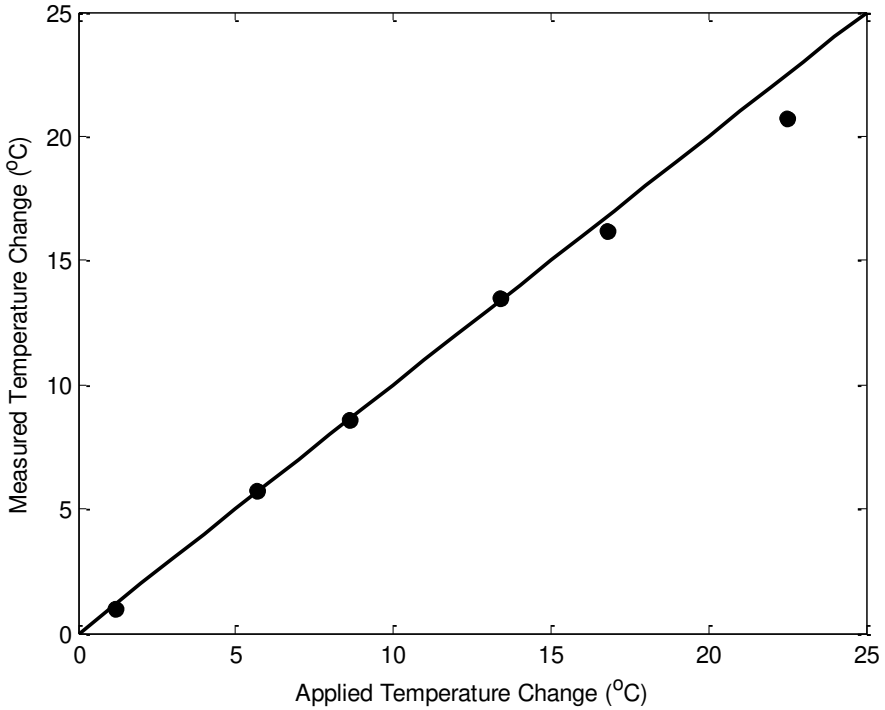

Figure 29: Measured temperature change as a function of applied temperature change. Solid line represents the perfect case when the applied temperature shift is the same as the measured temperature change [20]. The black circle represents the experimental data from the Sensor Matrix.

The change of refractive index can also be determined from the Sensor Matrix, as shown in Figure 30. The solid line plots the reference refractive index-temperature data extracted from Table 7 of [84]. Schiebener *et al* measured their experiment at 0.1 MPa and wavelength 0.6382 μm [84]. The refractive index at 30 °C is used as reference. Sensor Matrix data, in black circle, shows deviation less than 3×10^{-4} when compared to [84].

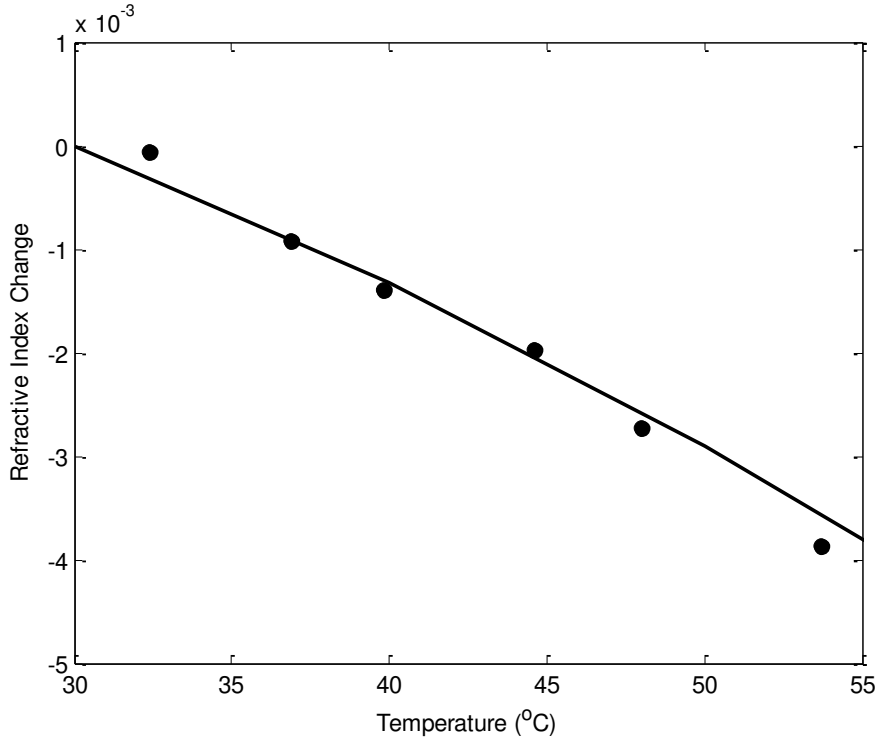

Figure 30: Calibrated refractive index as a function of temperature change. Black dots represent the experimental data. Curve line represents its fitting. The solid line plots reference refractive index-temperature data from [84] for comparison.

4.3.3 Label-Less Biosensor

The experimental setup is presented in Figure 31. One in-line microbubble PCF sensor, Sensor D, is connected to ASE light source and OSA to measure the transmission.

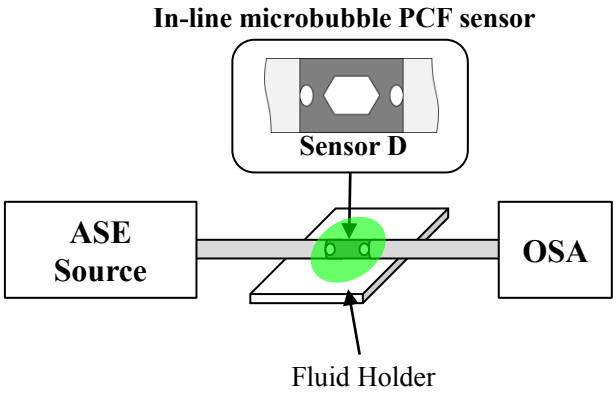

Figure 31: Experimental setup for the label-less biosensor.

Sensor D's refractive index response is plotted in Figure 32. For clarity, the dips are labelled (a) and (b). The measured spectrum shows the interference patterns are shifting from shorter wavelengths to longer wavelengths as the surrounding's refractive index increases.

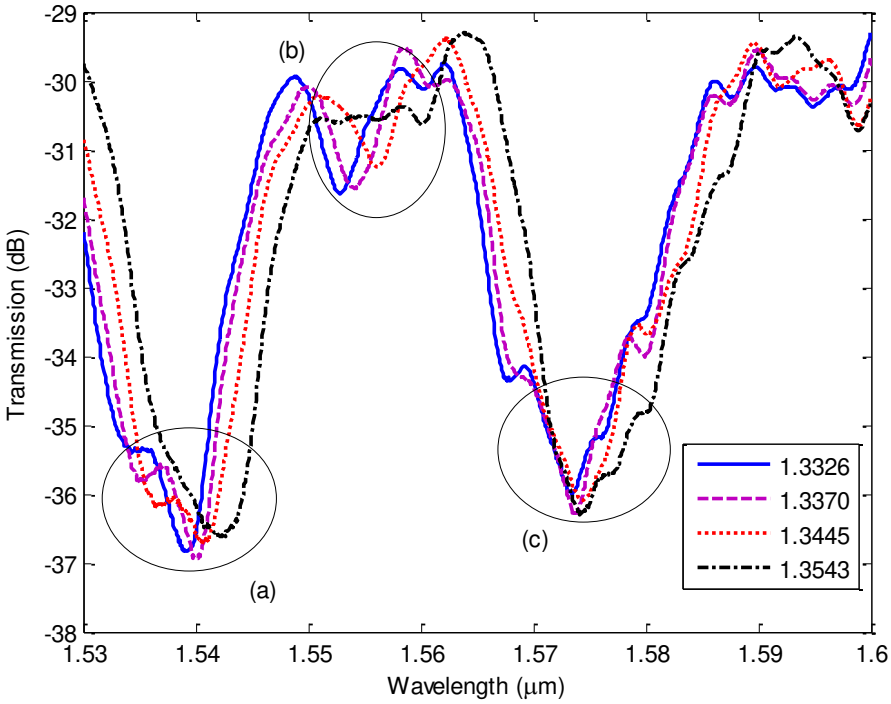

Figure 32: Measured spectrum of Sensor D during refractive index calibration. Three dips, labelled and circled, are tracked for analysis.

The two dips are tracked during refractive index calibration to determine Sensor D's refractive index sensitivity. They are chosen because their interference patterns remain relatively similar during the refractive index calibration.

From Figure 32, it is clear that the interference pattern is not a pure sine wave shape meaning that more than two interfering modes are interfering to produce the pattern.

To verify more than two modes are present, the corresponding spatial frequency for refractive index 1.3326 and 1.3370 spectrum is plotted in Figure 33. It shows that the core mode at 0 nm^{-1} interferes with the higher order cladding modes. Referring to Figure 12, where regions of the PCF's air holes are fully collapsed, the modes are no longer guided modes like the unmodified PCF region. The fully collapsed PCF regions are like coreless silica fiber without any core-cladding structure [85]. Hence, the modes will interfere with each other based on the multimode interference effect [86].

Forty-five strong cladding modes are identified that show changes in spatial frequency and intensity when subjected to refractive index change. The core mode does not change.

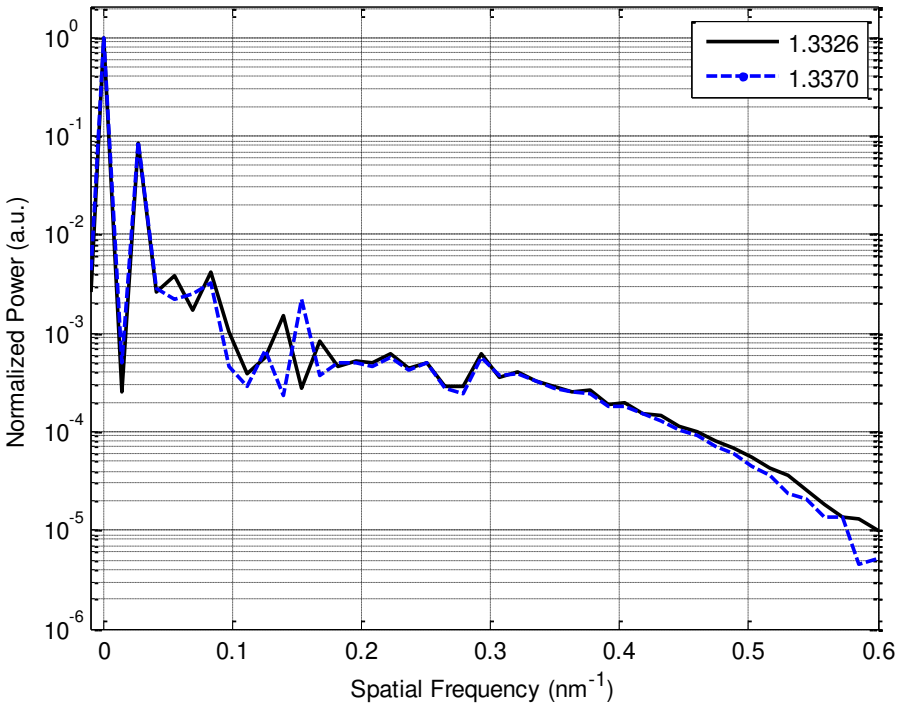

Figure 33: Spatial frequency spectra of Sensor D. The black solid line represents refractive index at 1.3326, and the blue dashed line represents refractive index at 1.3370.

Figure 34 shows dip (a) and (b) change in wavelength as the refractive index changes. A linear fit is applied to determine the refractive index sensitivity from 1.332 to 1.340. The result shows that dip (a) has a refractive index response of 166 nm/ RIU and dip (b) 320 nm/ RIU, respectively.

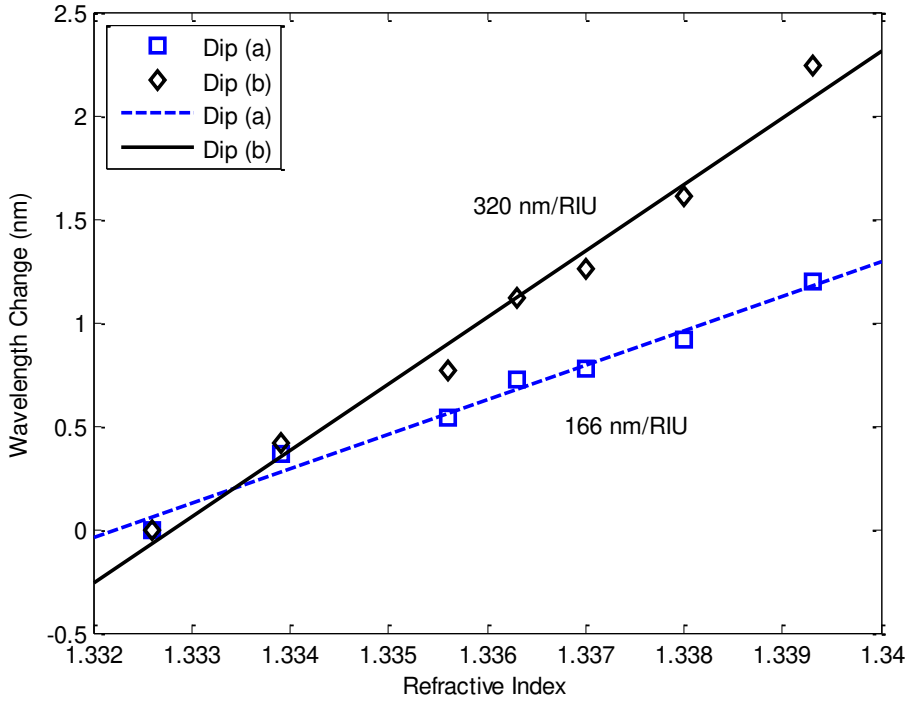

Figure 34: Wavelength change as a function of refractive index for the two dips. Symbols represent the experimental data and the straight lines represent its linear fitting.

Sensor D is then chemically modified and functionalised with biotin to become a biosensor as illustrated in Figure 35 [17]. 3-aminopropyltriethoxysilane (APTES) is attached to the surface of the sensor by placing the sensor into a mixture of 2% APTES in ethanol/H2O (95%/5%, v/v) for two hours. Next, the sensor is removed from the mixture and rinsed with de-ionised water and ethanol. Subsequently, the APTES modified surface is covalently attached to a layer of biotin by immersing into a mixture of 1 mg/mL biotin-NHS in de-

ionised water for one hour. Finally, the functionalised Sensor D is rinsed with de-ionised water to get rid of any unbound biotin-NHS molecules.

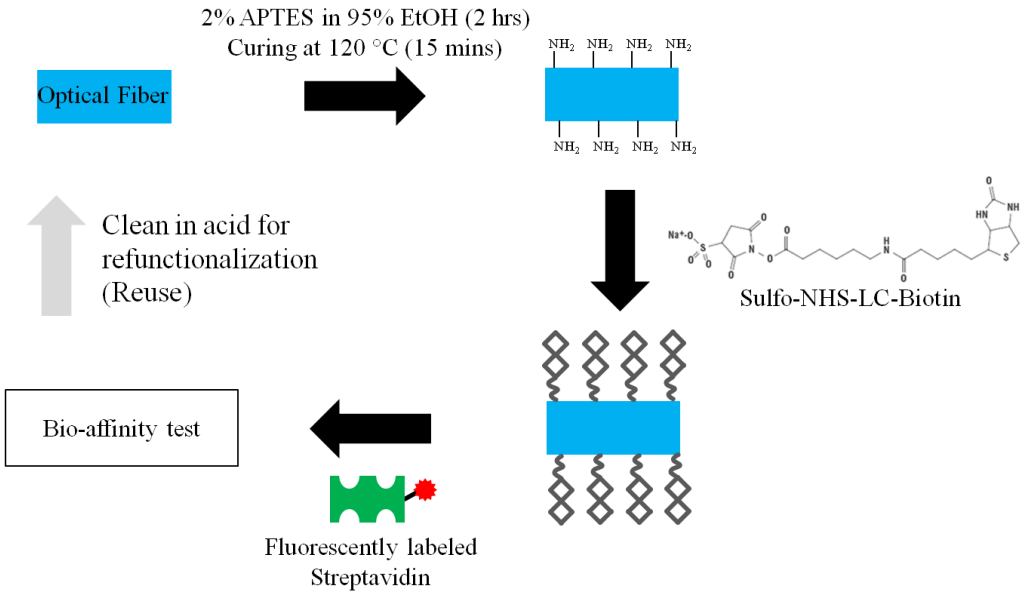

Figure 35: Schematic representation of the biotin modified optical fiber surface and the streptavidin immobilisation.

After surface modification and functionalisation with biotin, the interference pattern of Sensor D exhibits substantial changes, as depicted in Figure 36. The device is now a biosensor. The interference patterns are recorded when the biosensor is fully submerged in de-ionised water after thorough rinsing. The presence of biotin binding on the fiber surface causes the cladding modes to change, which results in a different interference pattern. Dip (a) and (b) are still visible with noticeable change in intensity level and wavelength.

Resonance wavelengths shift +1.26 nm and +0.49nm for dip (a) and (b) respectively. Dip (c) becomes untraceable due to the multiple dips from 1570 nm to 1590 nm.

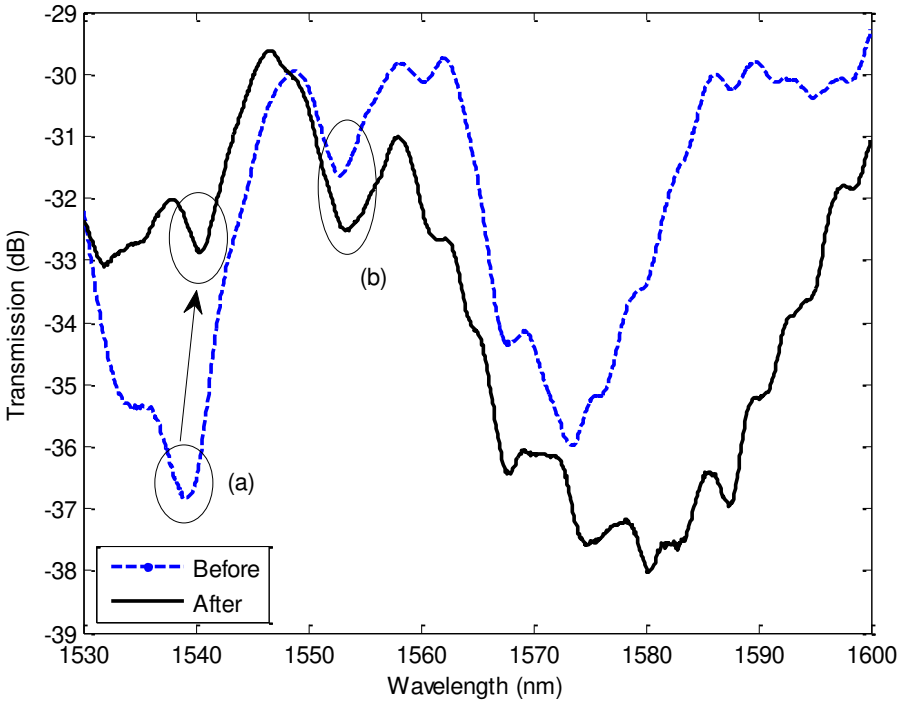

Figure 36: Measured spectrum of the biosensor in de-ionised water. Blue dashed line and black solided line represent the before and after interference pattern of the surface modification and functionalisation respectively.

For the bioaffinity test, two tests are performed. Firstly, the biosensor is submerged into 1 ml of the test solution for five minutes. The test solution has 10 μg/ml of streptavidin in a Phosphate Buffer Saline (PBS) solution.

After that the excess salt residue is rinsed off using de-ionised water. The measured spectrum is plotted by the red dashed line in Figure 37 from 1530 nm to 1560 nm. It is observed that dip (a) shifts 119 pm and dip (b) shifts 210 pm to longer wavelengths than before submerging in the test solution. Both the dips are attenuated about 1 dB.

Secondly, the biosensor is submerged into 1 ml of the test solution again until the streptavidin-biotin binding is saturated. This process allows the whole biotin-functionalised surface area to be bind with streptavidin.

In Figure 37, the blue dashed line at dip (a) and dip (b) depict a shift of 89 pm to shorter wavelengths, and 422 pm to longer wavelength respectively. From the bioaffinity tests, dip (b) exhibits a monotonic trend, which makes it an excellent choice for detection of biomolecules of the two dips. The label-less biosensor will eliminate the need to consider photostability of the dye in buffer or antifade, making the sensing mechanism distinctive from prior research.

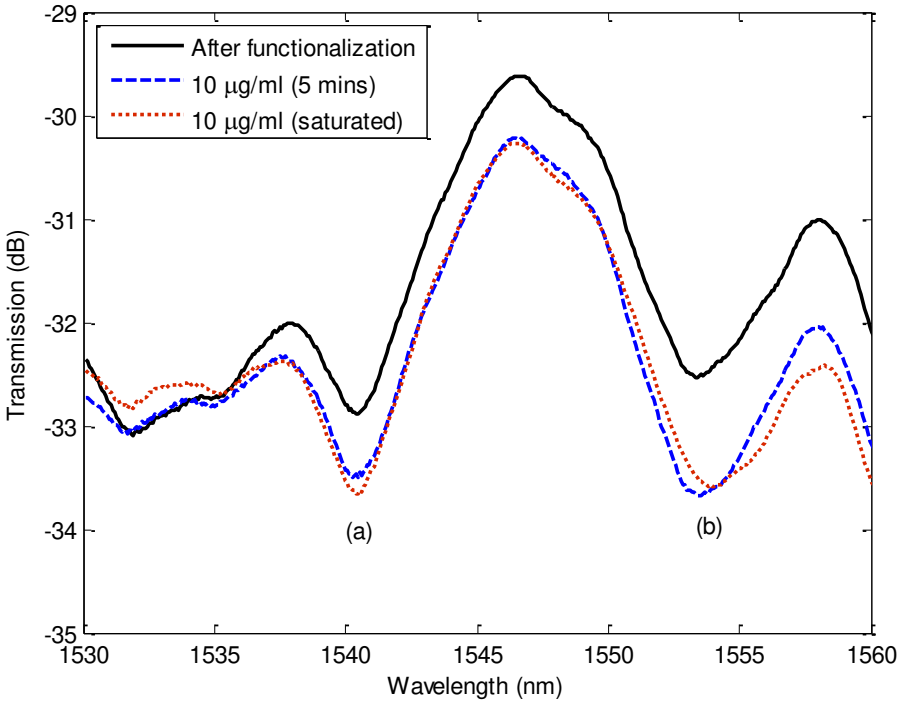

Figure 37: Measured spectrum of the biosensor during bioaffinity test. The streptavidin concentration is 10 µg/ml of PBS solution. Black solid line plots the spectrum after the functionalisation. Blue dashed line plots the spectrum after five minutes. Red dotted line plots the spectrum after streptavidin-biotin binding has saturated.

The streptavidin in the test solution is labelled with Cy3. The Cy3 dye is an orange-fluorescent label for scientific staining purposes. The benefit of the fluorescent dye labeled is to visually examine the biotin-modified fiber for any conjugation of streptavidin. The Cy3-labeled streptavidin is glowing red as shown in Figure 38. If there is no bioaffinity, no Cy3-labeled streptavidin will be attached to the PCF surfaces and the fluorescence image should be totally black like the region around the biosensor shown in Figure 38.

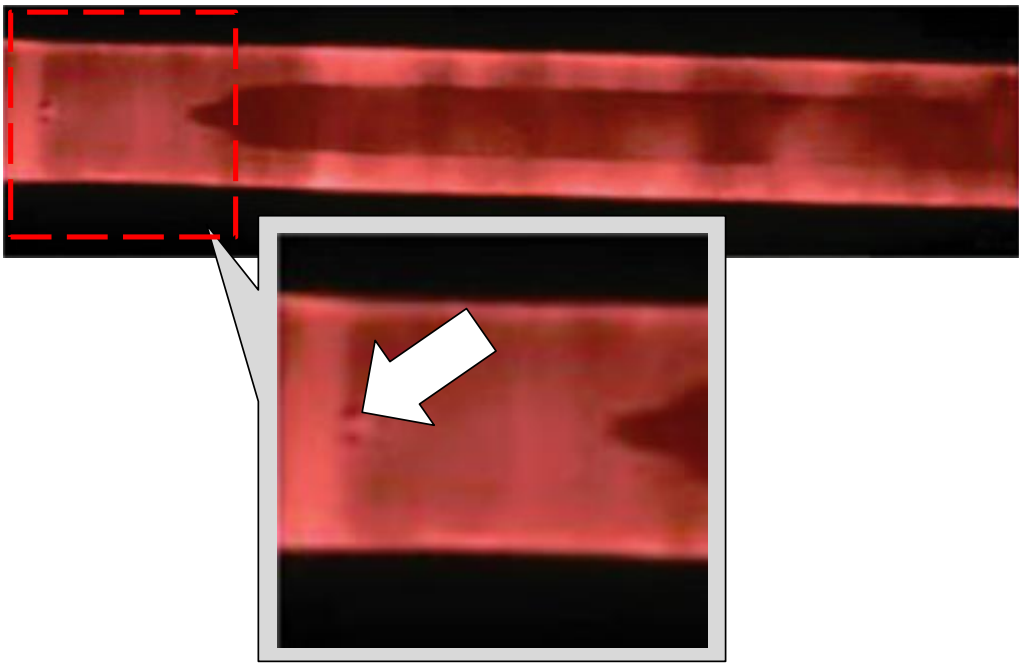

Figure 38: Fluorescence image after performing bioaffinity test. The Cy3-labeled streptavidin bonds to the surface of the biotin-modified PCF. The inset shows white arrow pointing at the microbubble inside the SMF-to-fully collapsed PCF region.

4.4 Summary

The refractive indices of the Test fluid used in the experiments using calibrated to the typical biosensing range from 1.33 to 1.38. The refractive index of the buffer solution, ~1.33, [87] and the mean refractive index of cell, 1.38, [88] set the lower and upper limits. In general, a cell typically consists mainly of an aqueous solution of salts and proteins. For different parts of the cell, the refractive indices are tabulated in Table 7, with other saline and buffer solutions. The lowest value is 1.33414 and the highest value is 1.39.

Biosensing	Refractive indices range
Cell's nucleus (except nucleolus)	1.355 to 1.365
Cell's cytoplasm	1.36 to 1.39
Cell's nucleolus	1.375 to 1.385
HeLa cells	1.385
Saline solution (contact lens)	~1.334
Sodium phosphate buffer (pH 7)	1.335
Sodium phosphate buffer (pH 7.4)	1.33414
Protein solution	1.34559

Table 7: Refractive indices range for different biosensing [89, 90, 91, 92, 93].

Cells make up tissues. Bolin *et al* report that there is a variation of refractive indices between the same type of tissues but different species of animal, and between different type of tissues but same species of animal [94]. For examples, among the species of human, canine, porcine and bovine, the variation of a kidney's refractive index is ~0.28. The four species of animals' liver and lung tend

to have lower refractive indices (average of species = 1.380) than other common tissues, 1.390 to 1.410 range. The human's lung shows the lowest refractive index of 1.367, while bovine's adipose stands out highest at 1.455 since it contains high lipid content [94]. Table 8 shows the comparison of refractive index responses between various types of optical fiber sensors from literatures and from this chapter.

Device length (mm)	Refractive index resolution	Sensor structure	Sensing range of the refractive index
44	3.4×10^{-5}	LP_{01}-LP_{0p} PCF [95]	1.33 to 1.38
19	1×10^{-4}	LMA PCF [54]	1.33 to 1.45
42 and 43	3.4×10^{-5}	Large-core air-clad PCF [96]	1.3225 to 1.327
6	7×10^{-4}	Two-ring triangular MOF with FBG [26]	~1.33
6	4×10^{-3}	Six-hole MOF with FBG [26]	~1.33
9.42	5.4×10^{-5}	Multimode interference [97]	1.33 to 1.45
20	8.8×10^{-5}	No-core fiber [98]	1.300 to 1.430
35 to 49	2×10^{-5}	LPG in PCF @1050nm [21]	1.33
30	6.49×10^{-4}	LPG, (in this thesis) [20]	1.33 to 1.38
2.81	7.94×10^{-5}	In-line microbubble PCF sensor (Sensor A in this thesis) [55]	1.33 to 1.38
3.25	1.07×10^{-4}	In-line microbubble PCF sensor (Sensor B in this thesis) [55]	1.33 to 1.38
3	1.16×10^{-4}	In-line microbubble PCF sensor (Sensor C in this thesis) [20]	1.33 to 1.38
3.1	6.25×10^{-5}	In-line microbubble PCF sensor (Sensor D in this thesis) [17]	1.33 to 1.34

Table 8: Comparsion of refractive index responses between optical fiber sensors at near water refractive indices.

In-line microbubble PCF sensors have many advantages over other types of sensors for biosensing. It can be fabricated by the fusion splicer machine, commonly used

for optical fiber communication or research without the need for precise or bulk alignment setup. Moreover, the refractive index resolution of the in-line microbubble PCF sensors are in the range of 10^{-5} to 10^{-4}, which is comparable to other high sensitivity optical fiber sensors and commercial refractometer, r2 mini by *Reichert*, used in the experiments. The two microbubbles in each in-line microbubble PCF sensor have created a shorter coupling length between the fiber modes to realise such high sensitivity. Being shorter in length will also require less fluid needed during testing and being able to fit or reach smaller spaces more easily.

Without using PCF to create intermodal interferometer, having a 9.42 mm length of multimode fiber sandwiched in between two single mode fibers would also produce the multimode interference required for sensing any change in external refractive index [97]. The corresponding refractive index resolution is 5.4×10^{-5} over 1.33 to 1.45.

Another similar intermodal interferometer with 20 mm of no-core fiber sandwiched in between two single mode fibers yields 227.14 nm/ RIU from 1.300 to 1.430 [98]. The long length of no-core fiber creates significant insertion loss at -80 dBm at the interference pattern's maximal. By observing Table 8, it clear that the in-line microbubble PCF sensors are relatively much shorter in length compared to PCF interferometer or intermodal interferometers reported by prior work.

Other groups have achieved high sensitivity by infiltrating the analyte [21] or Test Fluid into the air holes of the PCF [99, 100]. In the application of the biosensor, having the bioaffinity conjugation on the outer surface is notably of practical merit

than those inside of the PCF sensor. The most obvious reason is that cleaning the outer surface of PCF sensor is a straightforward process and it can be re-functionalised, and used again effortlessly. Moreover, the response time will be faster as there is no limitation of diffusive transportation inside the PCF [99].

Instead in the next chapter, we will discuss having the liquid infiltrated PCF for other excellent application such as for temperature sensing using liquid crystal.

5. Design and Analysis of Selective Infiltration of Liquid Crystal in Photonic Crystal Fiber

5.1 Introduction

In the fifth chapter, the infiltration of liquid crystal into a single air hole next to the core of the PCF is discussed. A brief overview of the fabrication technique is followed by the theoretical analysis and the experiments conducted. A directional coupler structure demonstrates its temperature sensing capability with simulation and experiment results.

5.1.1 Infiltration of PCF Air Holes

The axially aligned air holes in PCFs are excellent microfluidic platform for refractive index [101, 102, 56], biological event [100], and temperature [103, 104] sensing. Because of the small dimension of the air holes, the volume of infiltration material required is in the order of femtoliter to sub-nanoliter.

Infiltrated materials such as polymer [105], gas [106], liquid [107], metal [108], and semiconductor [109] have been demonstrated. The development of the selective infiltration technique has allowed the platform to produce highly controllable and repeatable devices.

The technique allows single air hole of PCF to be filled with high refractive index fluid to produce a highly sensitive temperature sensor such as a directional coupler structure [110, 111]. Those air holes filled with high refractive index fluid becomes a waveguide and interacts with the core guided modes of the PCF. When those interactions are in the phase matched condition, resonance wavelengths in the form of dips are present in the transmitted spectra. The thermal responses of the devices are 11.61 nm/ °C and 54.3 nm/ °C, respectively in the range of 1 °C and 1.5 °C.

5.1.2 Liquid Crystal

Liquid crystal is a special material that exhibits properties in between that of a solid and liquid. Friedrich Richard Reinitzer discovered the new phase of matter, the liquid crystal phase, in 1888 when he noticed that cholesteryl benzoate had two distinct melting points. The solid crystal, when heated to 145 °C, melted into a cloudy fluid when it was heated to 178.5 °C, it turned into a clear liquid.

The phenomenon is reversible, and a liquid crystal has an excellent thermal and electrical tunability. It is a suitable candidate for infiltration into the air hole of PCF for sensing temperature [112, 113], electric field [114, 115] and hydrostatic pressure [116].

Temperature sensing is typically conducted by exploiting the tuning the bandgap properties [117, 118]. The Nematic Liquid Crystal (NLC) is a type of liquid crystal that exhibits hedgehog topological defects. An example of NLC is the 6CHBT from *Military University of Technology*, Warsaw, Poland. The refractive index of liquid crystal changes when it is subjected to temperature changes from 20 °C to 53 °C, as plotted in Figure 39.

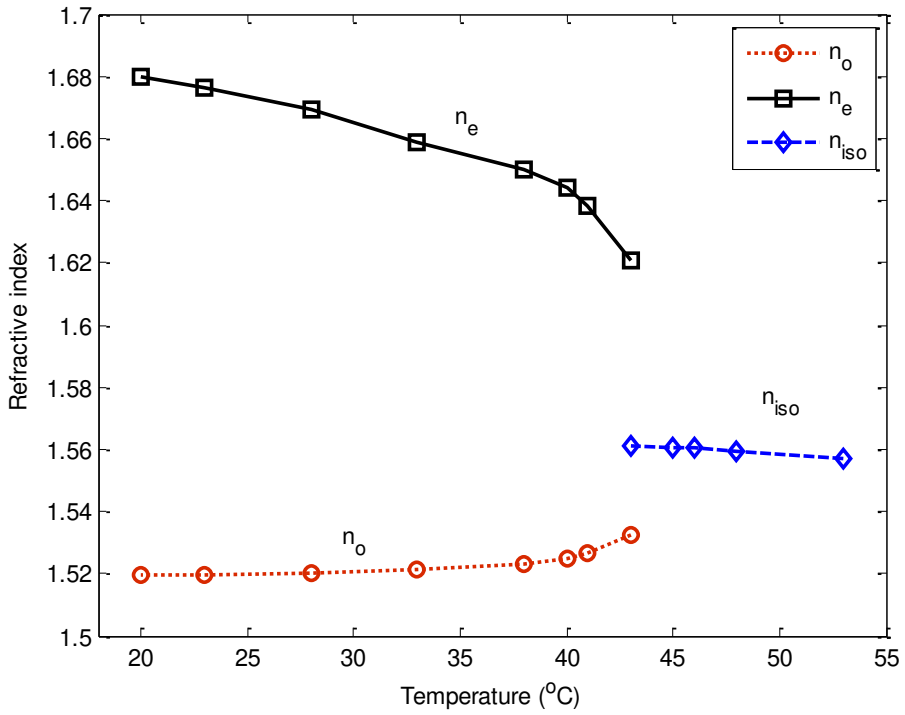

Figure 39: Refractive index of the 6CHBT as a function of temperature changes. n_e denotes extraordinary refractive index, n_o denotes ordinary refractive index, and n_{iso} denotes isotropic refractive index.

At lower temperature, the NLC is anisotropic and its nematic phase from 20 °C to 43 °C exhibits decreasing extraordinary refractive index and increasing ordinary refractive index as temperature increases. In the anisotropic phase, due to the flow-induced orientation, certain molecular alignments dominate [112]. At the transition phase at 43 °C, the nematic NLC becomes isotropic. The isotropic phase, from 43 to 53 °C, exhibits decreasing isotropic refractive index. When NLC is infiltrated into a PCF's air holes, the effective refractive index of light traveling along the PCF axis is near to the ordinary refractive index [103, 104] in the nematic phase.

5.2 Fabrication

Commercially available LMA-25 PCF, by *NKT Photonics*, is used to conduct the selective infiltration experiments [113, 119]. The selective filling technique fills a single air hole with NLC, and the filled PCF is spliced to SMF at both ends.

5.2.1 Profile of the Photonic Crystal Fiber

LMA PCF has a triangular lattice of air channels, with the core channel missing. The LMA PCF used in this thesis is shown in Figure 40. The core diameter of the LMA PCF is defined as:

$$d_{core} = 2\Lambda - d, \tag{22}$$

where Λ is the pitch between two adjacent air channel and d is the diameter of the air channel.

It is suitable for high power application in power generation and power delivery, due to the fact that it has a higher fiber damage threshold and low non-linearity compared to conventional optical fiber. The outer diameter, the air hole diameter, and the pitch of PCF are 268 μm, 8.4 μm, and 16.35 μm respectively [79].

Figure 40: Microscope image of the LMA-25 photonic crystal fiber cross section. Cladding diameter is 268 μm for reference.

5.2.2 Selective Infiltration Technique

Selective filling in the PCF is performed by first blocking all but one of the air channels that will be filled. Then the blocked PCF end is submerged in a test fluid (upright direction) to fill the unblocked air holes via the capillary effect.

When the test fluid infiltrates the required length, the filled PCF is taken out of the test fluid. It is then cleaved before measurements.

5.3 Result and Discussion

Commonly used stationary shop glue, for paper bonding, can be used to block the air holes of the PCF. It is applied by using two set of 3-axis translation stages and is viewed under a microscope.

The first 3-axis translation stage positions the PCF in the field of view of the microscope. The second 3-axis translation stage holds an optical fiber tip with a tapered end, which is used to put the glue to block the air holes. A digital microscope is used to oversee the whole process.

A tiny droplet of glue is put onto the tapered fiber tip by swiping across the surface of the glue stock. Once the glue droplet is in contact with the PCF, the glue will spread and flow across the end surface of the PCF.

The movement is dependent on its viscosity, surface tension and composition. When there is sufficient glue applied to block the air holes, the tapered fiber tip is moved away from the PCF and the glue is allowed to dry by air.

The whole process usually takes a few minutes to about thirty minutes. Different patterns can be achieved as illustrated in Figure 41.

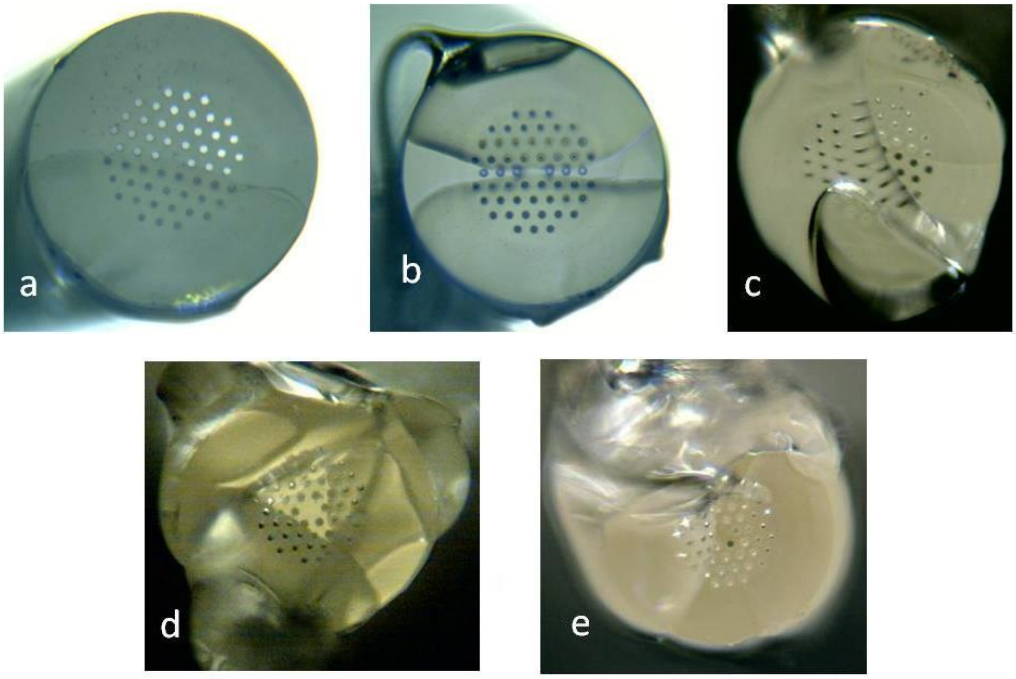

Figure 41: Microscope image of blocking patterns on the LMA-25 PCF. (a) About half of the air holes are unblocked; (b) center row of air holes are unblocked; (c) a pie-shaped of air holes are unblocked; (d) a triangle-shaped of air holes are unblocked; (e) a single air holes is unblocked and used for selective infiltration. Cladding diameter is 268 μm for reference.

The glue blocking the air holes of the PCF is cured via air drying and the glued end of the PCF is submerged into the NLC solution for infiltration. The NLC solution will fill up the unblocked air holes by capillary effect. After the NLC solution has infiltrated the whole length of the PCF, the non-glued end of the PCF is used to examine and verify the infiltration process. Figure 42 shows one of the air hole, next to the PCF core, selectively filled with NLC. The NLC filled air hole can be

seen clearly, as a white circle, when compare to other unfilled air holes, seen as dark circles. The NLC filled PCF length is 101 mm.

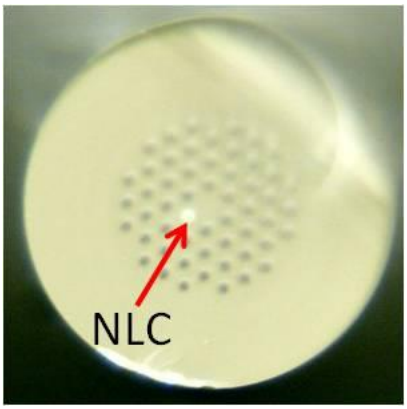

Figure 42: Microscope image of the selectively filled NLC in one of LMA-25 air holes. Cladding diameter is 268 μm for reference.

There are a few pointers to take note when splicing the NLC-filled PCF to SMF to ensure minimal splice loss. Firstly, the fiber facet must be cleaved properly. Secondly, the arc position of the fusion splicer machine must be adjusted 80 μm towards the SMF side. This is to minimize the damage to the NLC due to heat and prevent bubble formation when air expands when heated. Thirdly, due to the fact that LMA-25 has a much larger cladding than SMF, a fully collapse region will ensure a mechanically strong splice.

In Figure 43, it is seen that the air hole filled with NLC does not fully collapse in the fully collapse region. This phenomenon is due to the reason that air is

very compressible compared to NLC, and some NLC solution may have changed into vapor when the arc is applied. Otherwise, there should be no protruding channel in the fully collapse region.

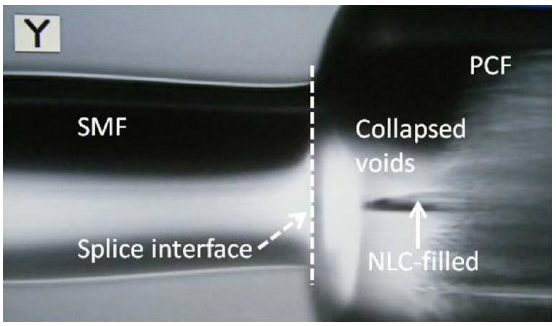

Figure 43: Microscope image from the fusion splicer machine for the splice between SMF and NLC filled LMA-25.

5.3.1 Theoretical Analysis

Mode coupling occurs between the NLC channel and the core of the PCF in the NLC selective filled PCF [110, 111]. When the effective mode index of NLC channel matches to that of the PCF core at the phase matching wavelengths, resonance wavelengths, in the form of dips, are observed in the interference pattern.

Modes propagating in the core of the pure silica PCF are insensitive to small temperature variation. However, the modes at the NLC channel are highly

dependent on temperature because of the optical properties of NLC. In other words, the guided modes of the NLC change as a function of temperature.

The coupled mode theory explains the mechanisms observed. The PCF core and NLC channel are independent waveguides affected by the perturbation of the lightwave from one another. The coupled modes must satisfy [120] the phase matching condition when:

$$\beta_{core} = \beta_{NLC}, \tag{23}$$

where

$$\beta_{core} = k_0 n_{eff,core} , \tag{24}$$

and

$$\beta_{NLC} = k_0 n_{eff,NLC} , \tag{25}$$

are the propagation constants for the core mode and NLC mode respectively, k_0 is the wave vector in vacuum, $n_{eff,core}$ and $n_{eff,NLC}$ are the effective indices of the core mode and NLC mode respectively.

In other words, higher order NLC channel modes are coupled to the PCF's core guided modes when the phase matching condition is satisfied, which is the resonance wavelength [121]. At resonance wavelength, their effective mode indices match and maximum power coupling takes place. The resonance wavelength corresponds to the resonance condition being satisfied. From

Figure 39, it is clear that the refractive index of the NLC is higher than that of the silica. Hence, only the higher order modes of the NLC channel can fulfil the phase matching condition.

The temperature sensitivity and mode profiles are modeled and examined using Lumerical MODE Solutions. The refractive index of the silica PCF is defined as 1.448. The NLC isotropic refractive index is 1.5605 at 46 °C.

The first sixty guided modes of the NLC channel are shown in Figure 44. The calculated dispersion from 1530 nm to 1600 nm is plotted in Figure 44. Figure 45 shows all the sixty NLC channel modes (LP_{01} to LP_{23}) in black solid lines and the PCF core modes (LP_{01} to LP_{11}) in blue solid lines at 46 °C.

In Figure 46, NLC channel modes LP_{71}, LP_{04} and LP_{23} intersect PCF core modes LP_{01} and LP_{11}. Black lines denote the PCF's silica core modes. Blue dashed lines denote one of the NLC channel modes for analysis later. If the phase matching condition is satisfied at the intersection, the three NLC channel's modes couple to the two PCF core's modes [120]. Multipeaks in the resonance wavelength are caused by these coupled modes at 1580 nm and 46 °C.

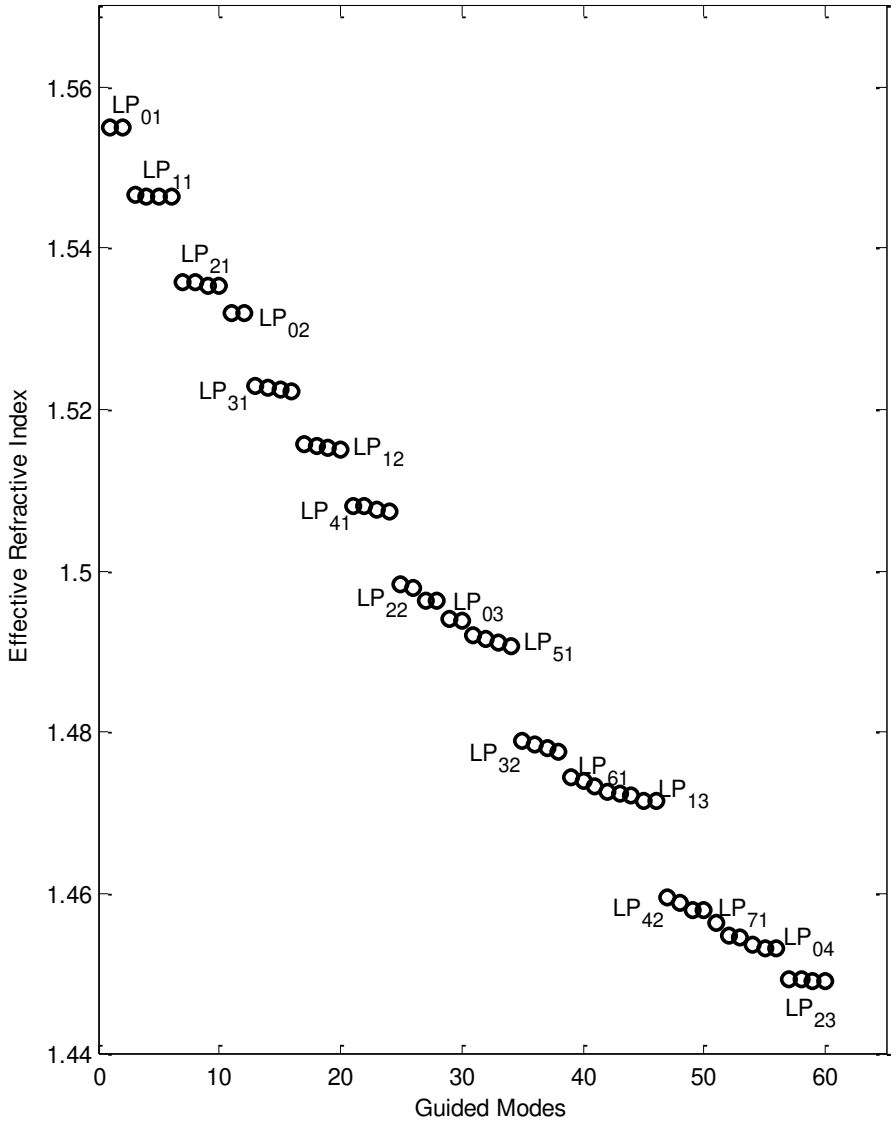

Figure 44: Calculated effective refractive index of the guided modes at 46 °C and 1600 nm. LP represents Linear Polarised.

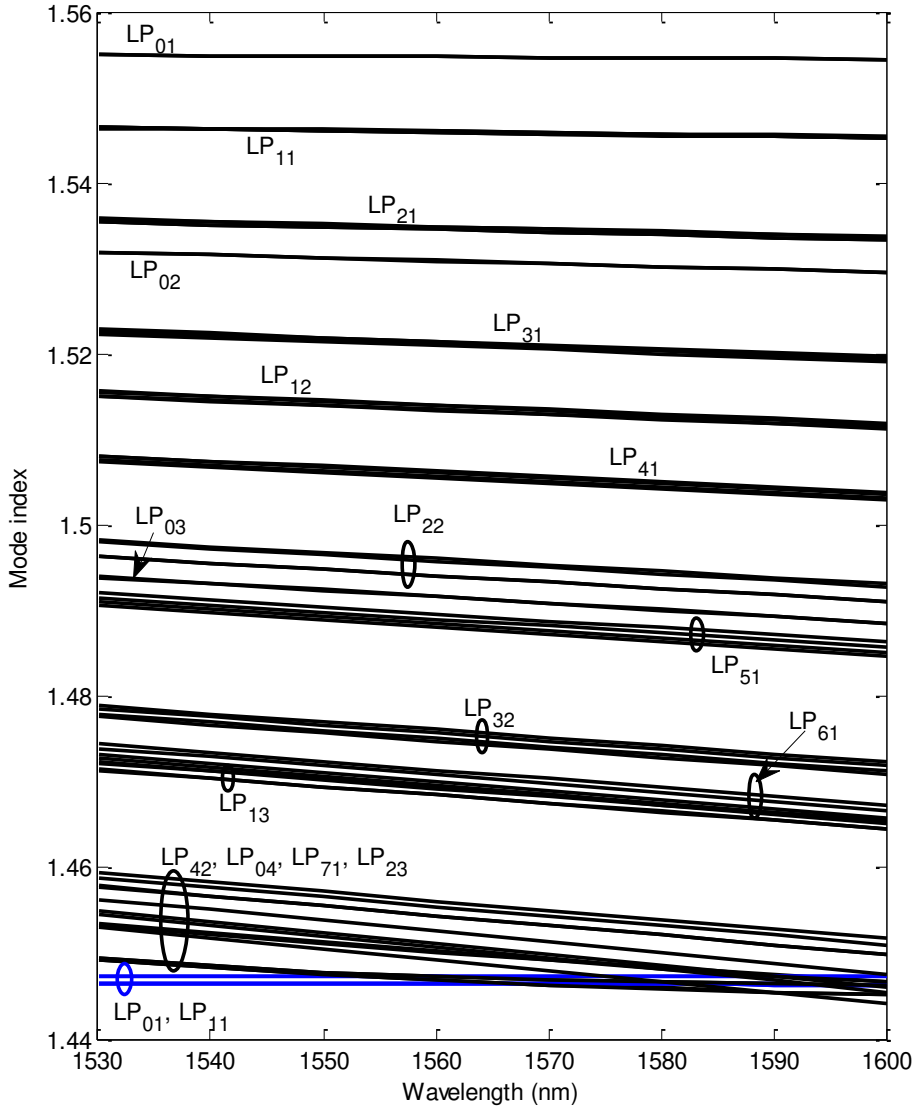

Figure 45: Calculated NLC channel modes and PCF core modes at 46 °C.

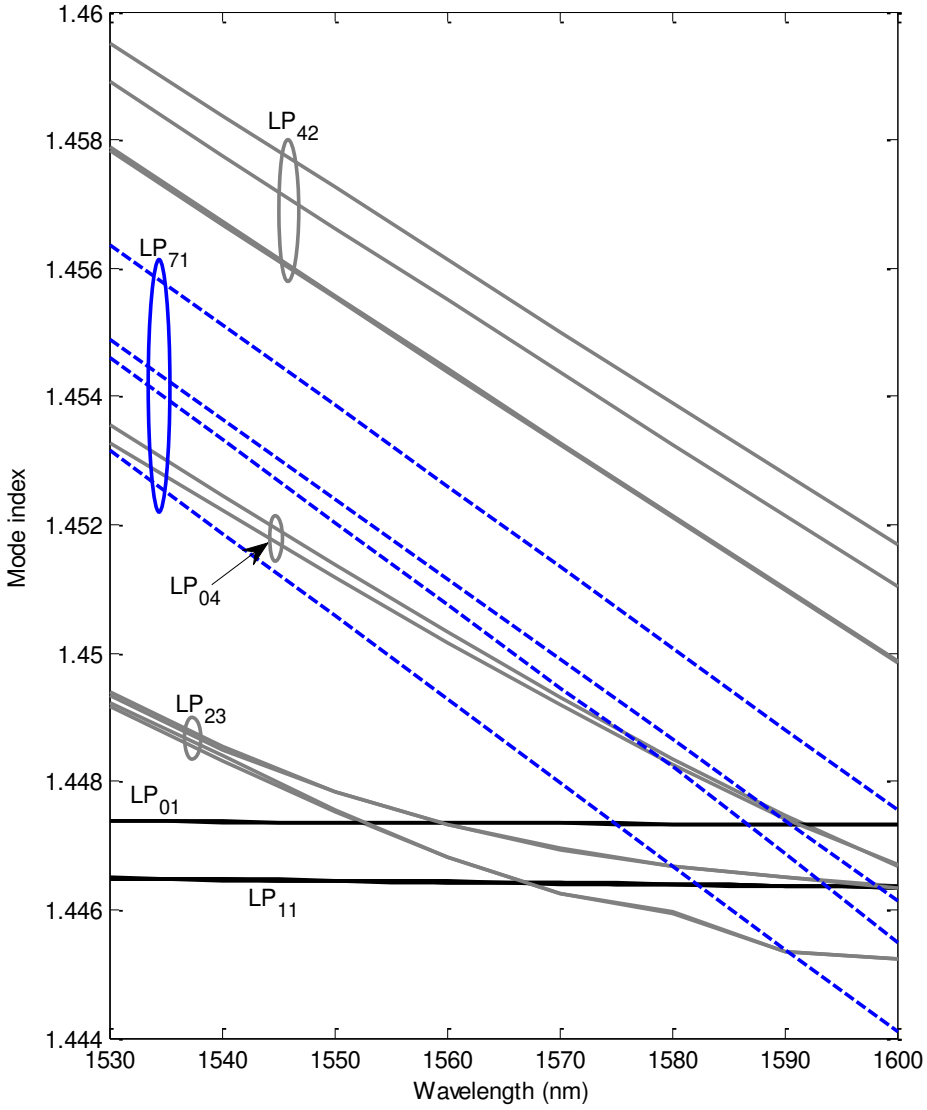

Figure 46: Intersections between NLC channel modes (LP_{71}, LP_{04} and LP_{23}) and PCF core modes (LP_{01} and LP_{11}).

To compute the temperature sensitivity, the intersection of NLC channel mode LP_{71} and PCF core mode LP_{01} is tracked. Additional dispersion calculations are simulated at 48 °C and 53 °C with the isotropic refractive index at 1.5595 and 1.5573 respectively, as shown in Figure 47. The modal dispersion for 46 °C, 48 °C and 53 °C are calculated because only these temperatures data points within the NLC's isotropic refractive indices are available for input into the model.

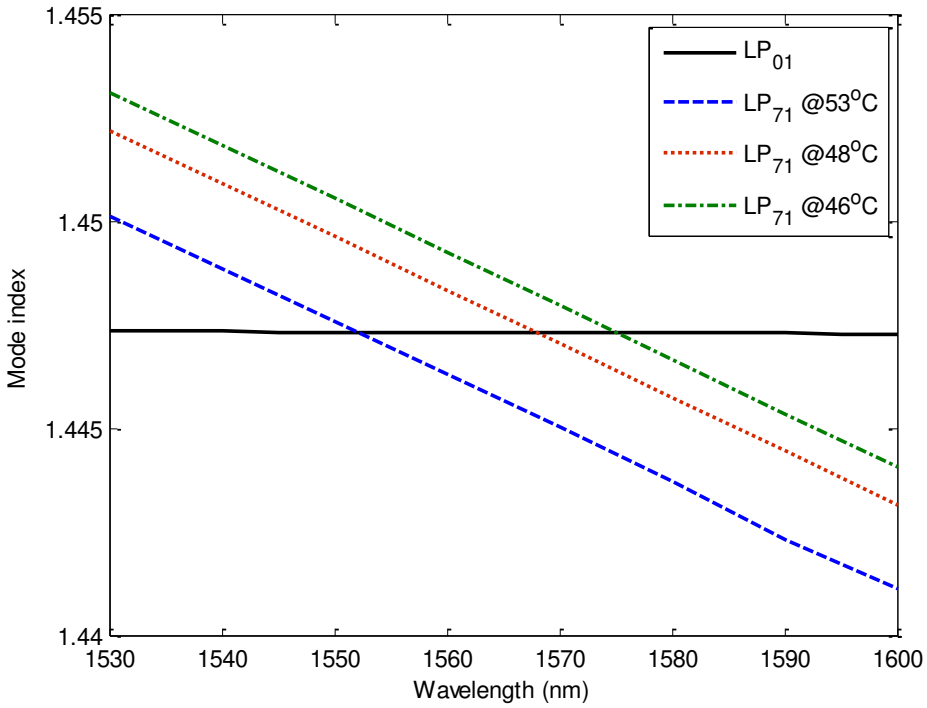

Figure 47: Calculated NLC channel mode LP_{71} and PCF core mode LP_{01} at 46 °C (solid), 48 °C (dashed), and 53 °C (dotted).

Those linear fit line is plotted in Figure 48. The calculated temperature sensitivity is −3.27 nm/ °C.

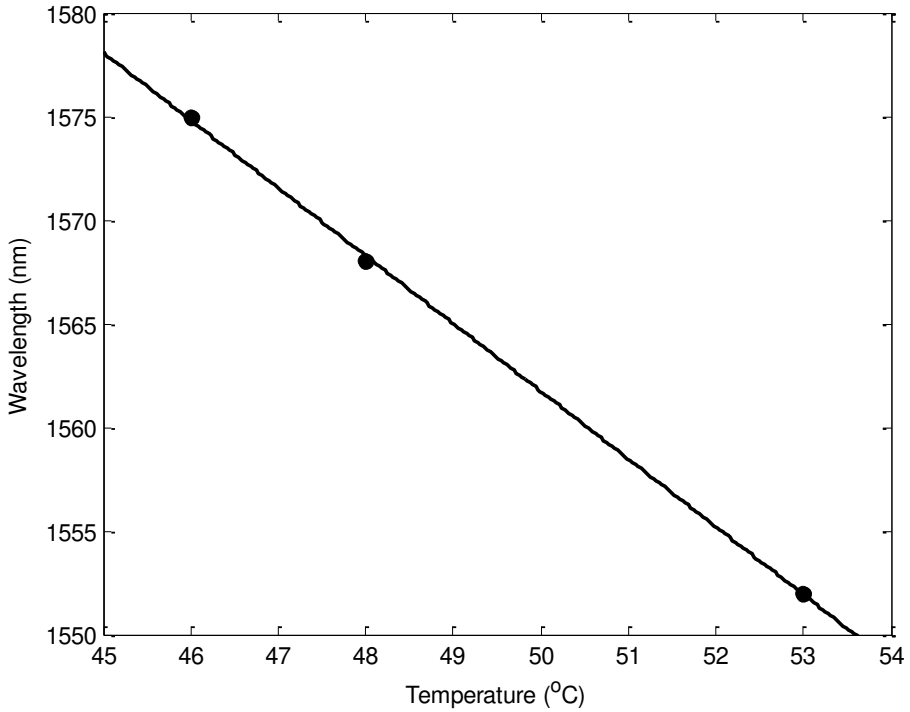

Figure 48: Calculated temperature response tracking the resonance wavelength. Symbols represent the phase matching condition data and the straight lines represent its linear regression line.

5.3.2 Experimental Analysis

In the experiment, the fabricated sensor is placed in an oven to examine how it respond with temperature changes. In the later part, the cut back method

investigates how the length of the infiltrated device influences the thermal response.

The measurement setup is illustrated in Figure 14(a). For clarity, the measured spectra are separated into four plots, by NLC phase and interference pattern, as shown from Figure 49 to Figure 52.

In the nematic phase of the NLC, the measured interference pattern shifts to longer wavelength as the temperature increases, as depicted in Figure 49 and Figure 50.

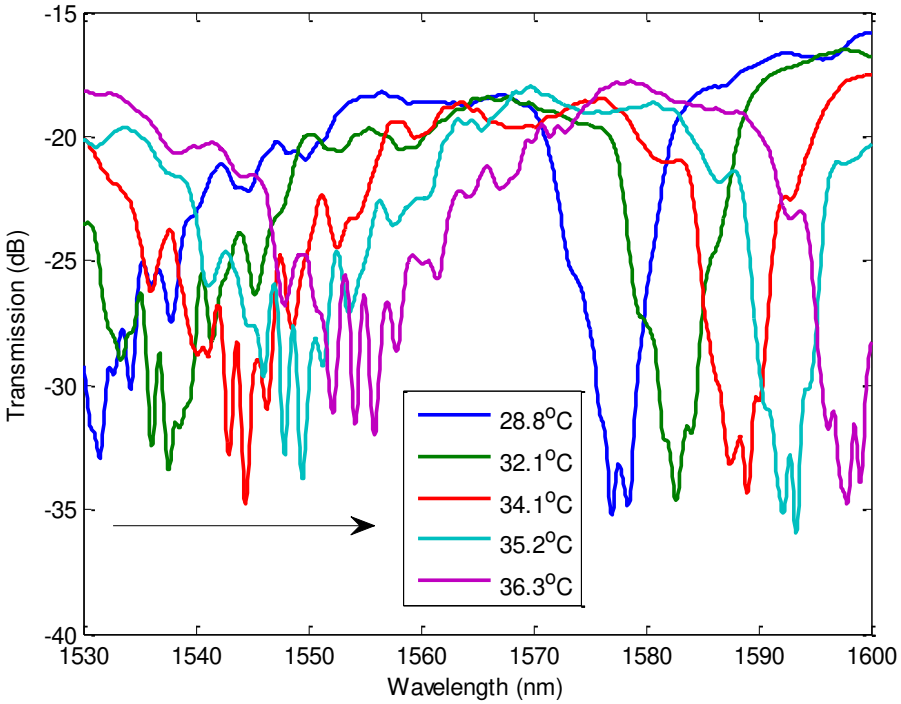

Figure 49: Measured spectrum of the NLC selectively filled PCF in the nematic phase at 28.8 °C, 32.1 °C, 34.1 °C, 35.2 °C, and 36.3 °C.

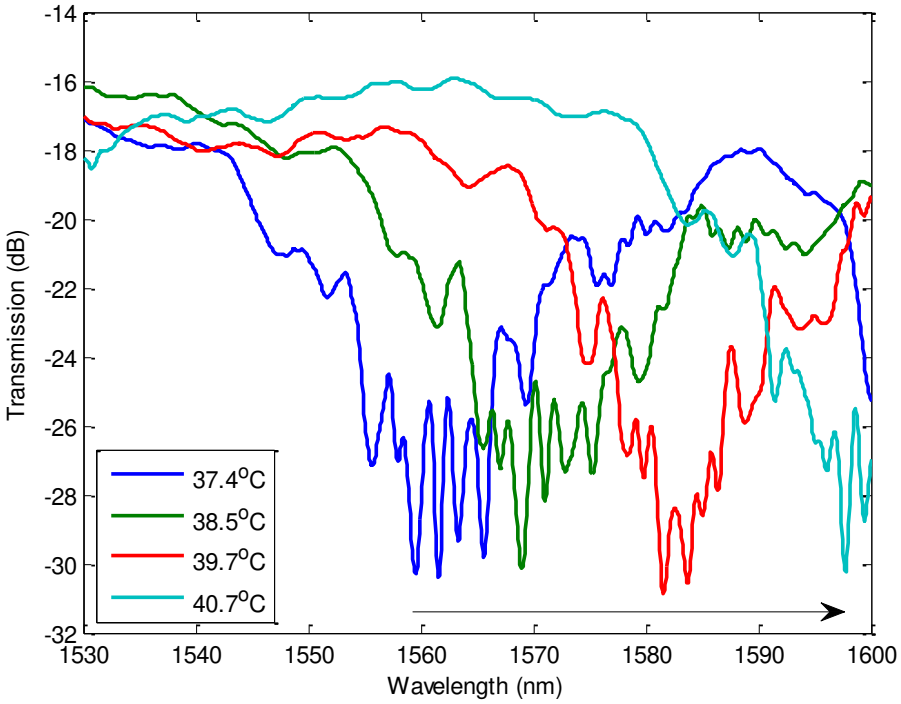

Figure 50: Measured spectrum of the NLC selectively filled PCF in the nematic phase at 37.4 °C, 38.5 °C, 39.7 °C, and 40.7 °C.

In the transition phase, the measured interference pattern shows an unstable pattern that is constantly changing. Figure 51 shows two instances of the captured interference patterns.

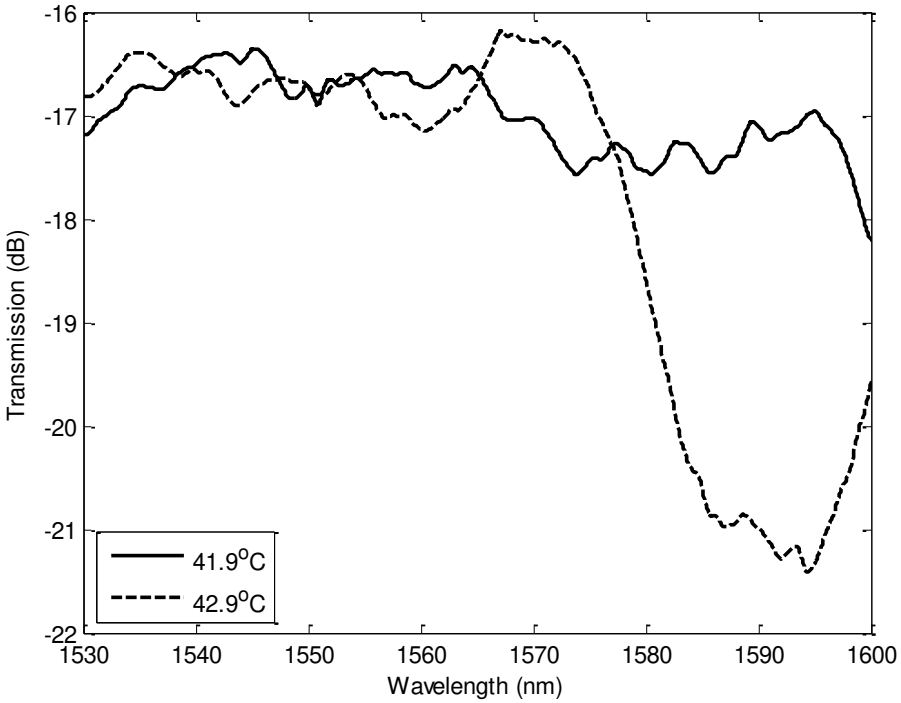

Figure 51: Measured spectrum of the NLC selectively filled PCF in the transition phase from nematic to isotropic phase.

Figure 52 displays the isotropic phase measurements, the measured interference pattern moves to the left side of the wavelength window as the temperature increases. The result shows the temperature dependency to the NLC refractive index, as shown in Figure 39. The strong mode coupling between the core modes and the NLC channel modes produce the dips found in the measured interference patterns.

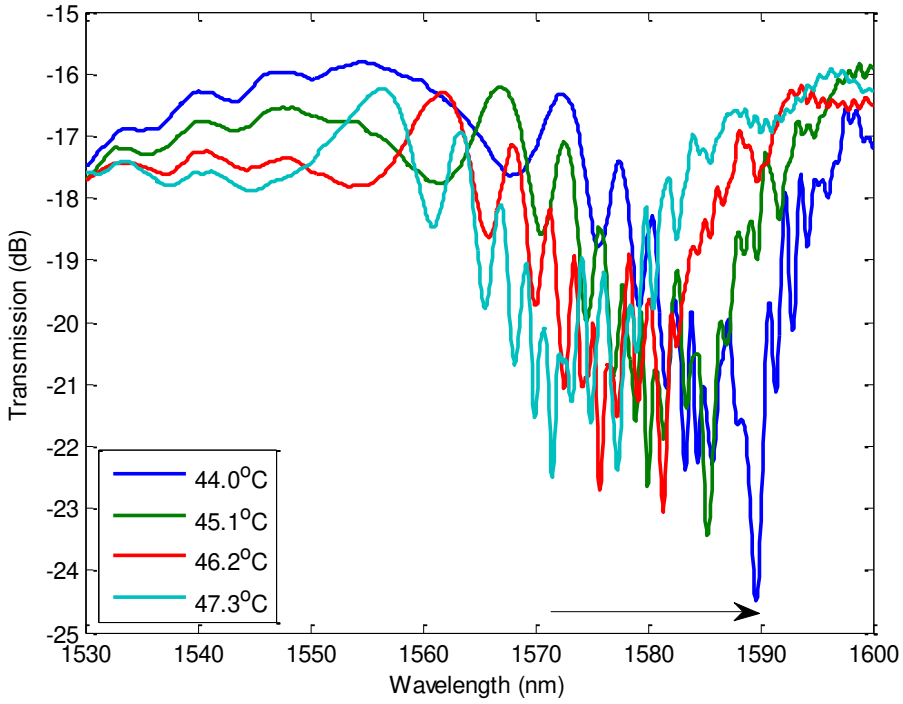

Figure 52: Measured spectrum of the NLC selectively filled PCF in the isotropic phase at 44.0 °C, 45.1 °C, 46.2 °C, and 47.3 °C.

The silica refractive index is lower than the NLC at all temperatures, therefore the higher order modes of the NLC channel will couple to the silica core. The mode coupling will occur at the phase matching condition at the resonance wavelength.

Assuming there is no temperature dependence of the silica core guided modes, therefore any wavelength shift in the interference pattern attributes to changes in the NLC channel. Consequently, the effective refractive index of the NLC channel modes changes with temperature.

It can be seen from Figure 49, Figure 50, and Figure 52 that there are multipeaks at the dip region. For the purposes of calibrating the temperature response, the dip at the longer wavelength of Figure 49 is traced. This is because there are fewer multipeaks in that span of wavelength. In Figure 52, the dip at longer wavelength is traced.

Figure 53 shows a quadratic curve fitting of the resonance wavelength shift in nematic phase. The resonance wavelength is the minimal point of the interference pattern in Figure 52. The temperature sensitivity in the nematic phase is found to be 1.61 nm/ °C between 28.8 °C to 31.5 °C and 4.55 nm/ °C between 34.1 °C to 36.3 °C, along the second-order polynomial curve.

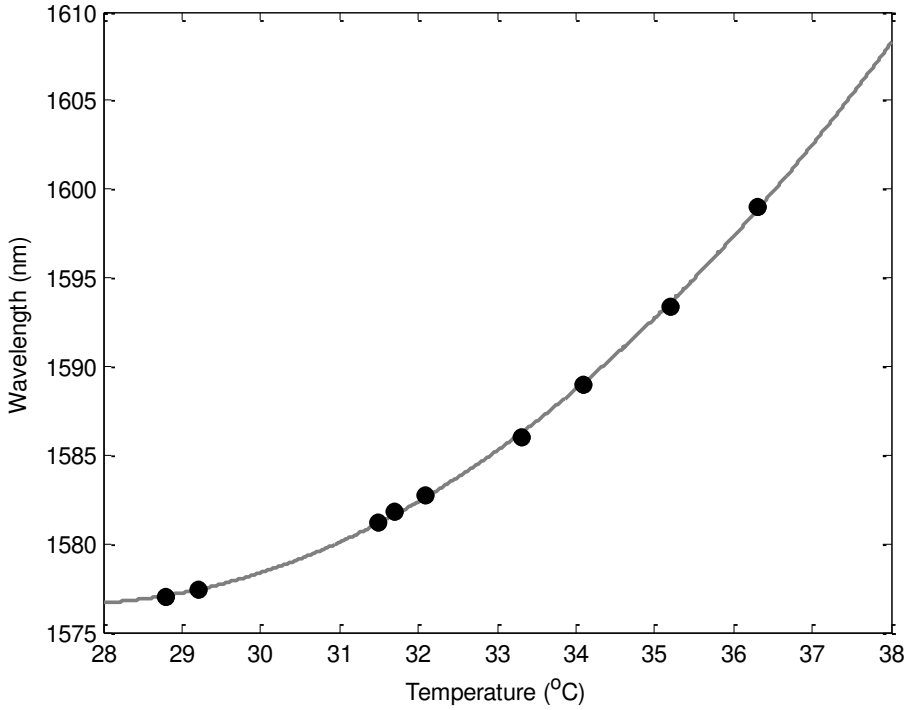

Figure 53: Temperature response of the resonance wavelength in nematic phase. Black circles represent the experimental data from Figure 49 and Figure 50, and the solid lines represent its curve fitting.

Figure 54 shows a linear regression line of the measured data points in the isotropic phase. The temperature sensitivity in the isotropic phase is found to be −3.72 nm/ °C between 44 °C to 47.5 °C.

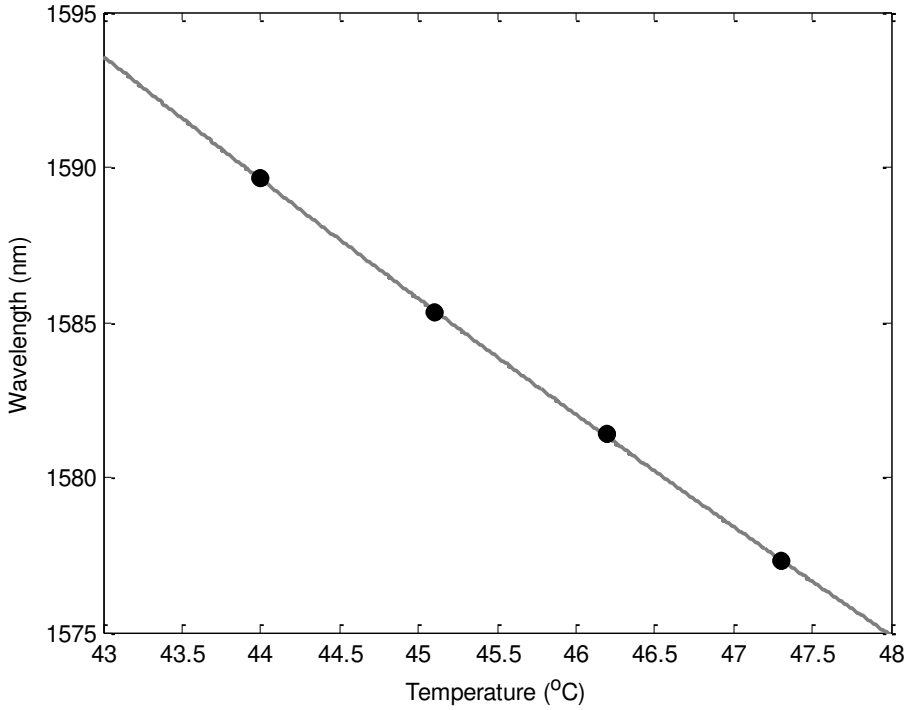

Figure 54: Temperature response of the resonance wavelength in isotropic phase. Black circles represent the experimental data from Figure 52, and the solid lines represent its linear fitting.

Next, the cut back method is used to investigate if there is any dependence on the interference pattern in the isotropic phase. The sensor is cleaved at the PCF to reduce the length and spliced to SMF for measurement.

The measured results for five different lengths are plotted in Figure 55. The measurement temperature is maintained at 46 °C with a deviation of less than 0.5 °C for consistency. The result shows that as the PCF length reduces the number of multipeaks in the resonance wavelength decreases.

Figure 55(e) shows the best resonance wavelength at 1576.5 nm without any multipeaks of 9 mm PCF length. The Full-Width Half-Maximum (FWHM) for the resonance wavelength, dip, is approximately 2 nm.

The experimental results show that there is no significant change in the insertion loss with the exception of the 18 mm PCF length. The typical insertion loss is from 16 to 20 dB. Because of the multipeaks near the dip, 101 mm, 78 mm, 68 mm, and 18 mm PCF length exhibit approximately 2 dB to 10 dB dynamic ranges.

The 9 mm PCF length has approximately 17 dB dynamic range without any multipeaks. It's FWHM is approximately 2 nm. Another observation from the five sub-plots is that the wavelength position of the dip is located at ~1580 nm.

Hence, the interference pattern of the 9 mm PCF length in Figure 55 is the easiest to distinguish and track than the other four PCF lengths for practical sensor application.

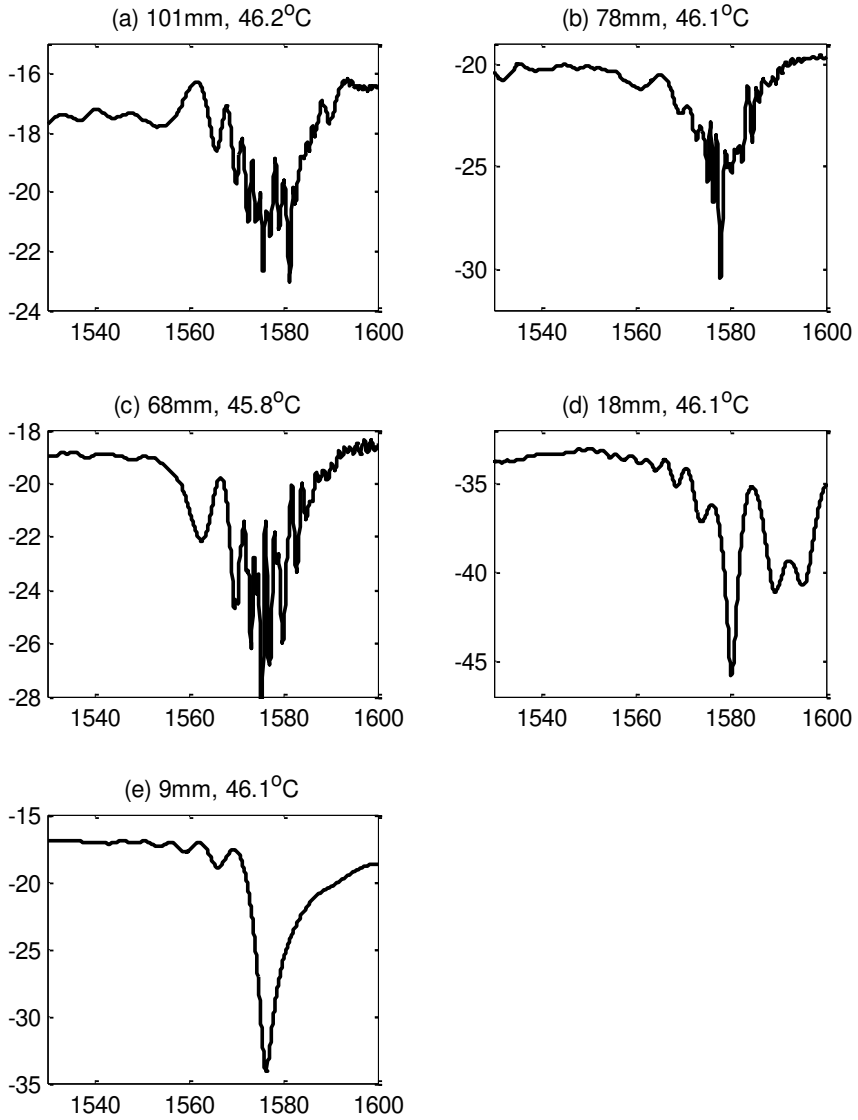

Figure 55: Measured spectrum of different PCF length at the same temperature around 46 °C. The horizontal axis is the wavelength in nm, and the vertical axis is the transmitted power in dB.

The 9 mm PCF length that has the best interference pattern without any multipeaks in the resonance wavelength is further investigated for temperature dependence.

The measured temperature spectra in the nematic, transition, and isotropic phases are plotted in Figure 56, Figure 57, and Figure 58 respectively.

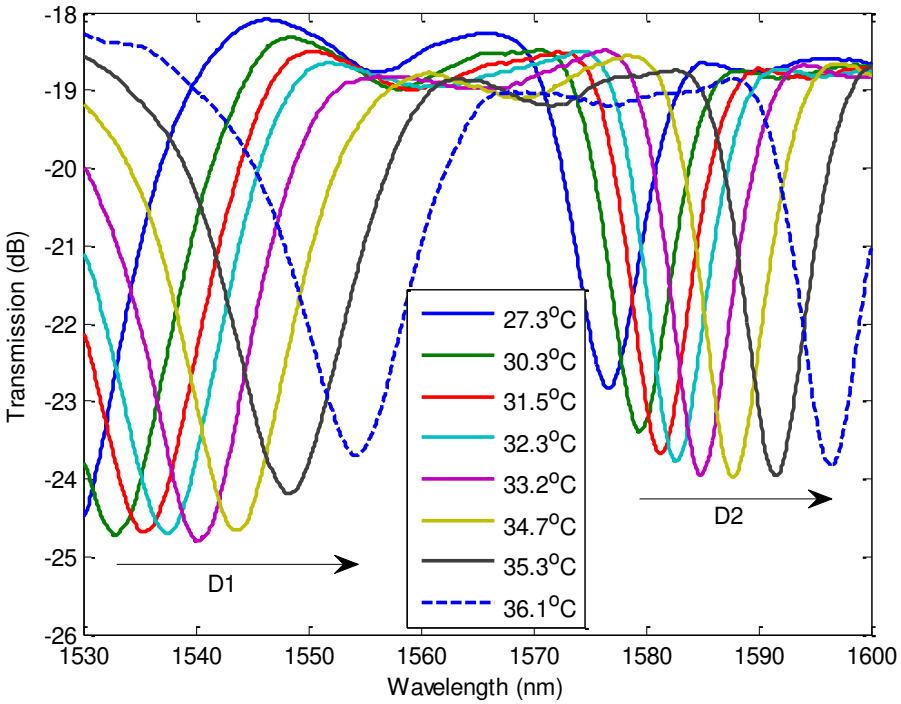

Figure 56: Measured spectrum of the 9 mm PCF length in the nematic phase from 27.3 °C to 36.1 °C.

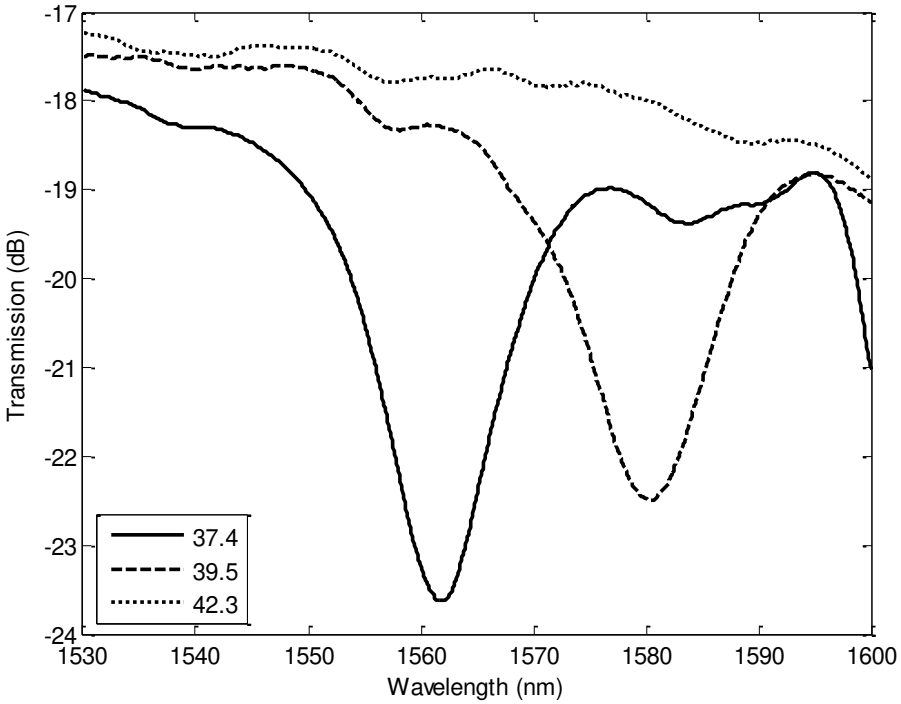

Figure 57: Measured spectrum of the 9 mm PCF length in the transition phase from 37.4 °C to 42.3 °C.

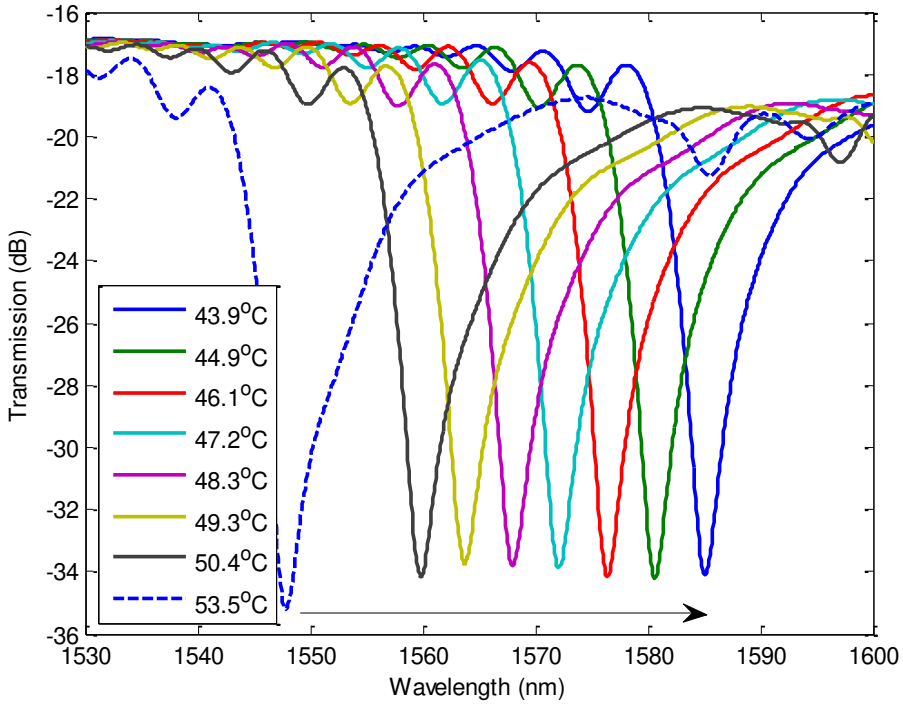

Figure 58: Measured spectrum of the 9 mm PCF length in the isotropic phase from 43.9 °C to 53.5 °C.

The resonance wavelengths of Figure 56 and Figure 58 are tracked and plotted in Figure 59 and Figure 60 respectively. In the nematic phase, the two dips' wavelengths, in the shorter and longer span of the wavelength window, are monitored as a function of temperature. The data points are fitted with second-order polynomial regression curves.

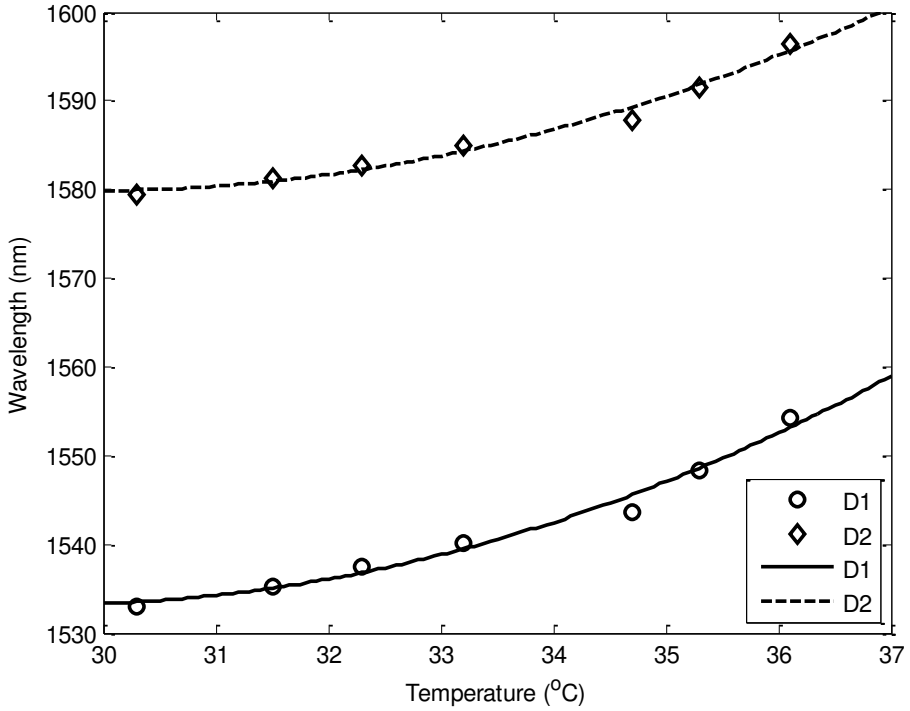

Figure 59: Measured temperature responses of the 9 mm PCF length by tracking the two resonance wavelengths in the nematic phase. Symbols represent the dips from Figure 56, and the solid lines represent its linear fitting

In Figure 60, the dip's wavelengths of all the five PCF lengths are plotted with respect to the measured temperature in isotropic phase. The linear regressions are shown in Figure 61. The 9 mm PCF length has a temperature sensitivity of −3.86 nm/ °C. The other four PCF lengths demonstrate temperature sensitivity ranging from −3.56 nm/ °C to −3.96 nm/ °C between 42 °C to 53 °C in the isotropic phase.

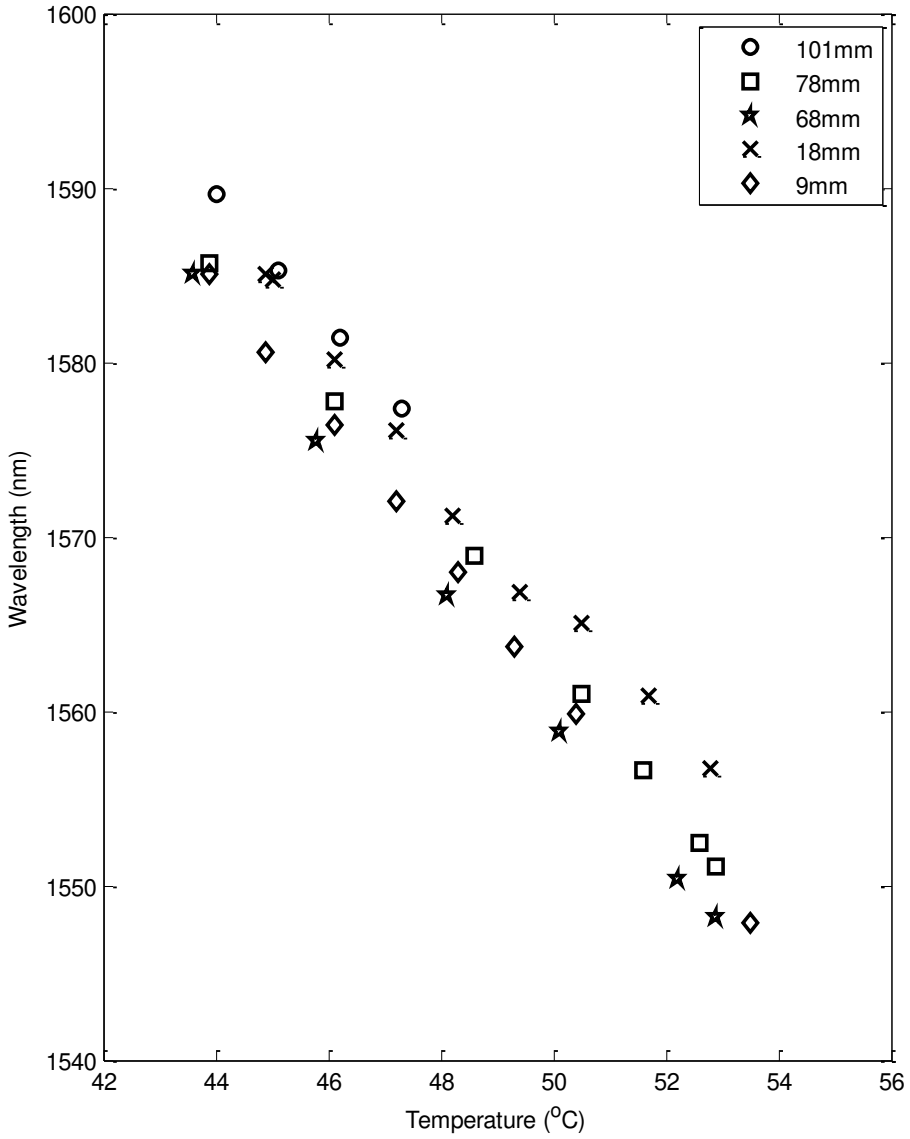

Figure 60: Measured temperature responses of five different length devices by tracking the resonance wavelength in the isotropic phase.

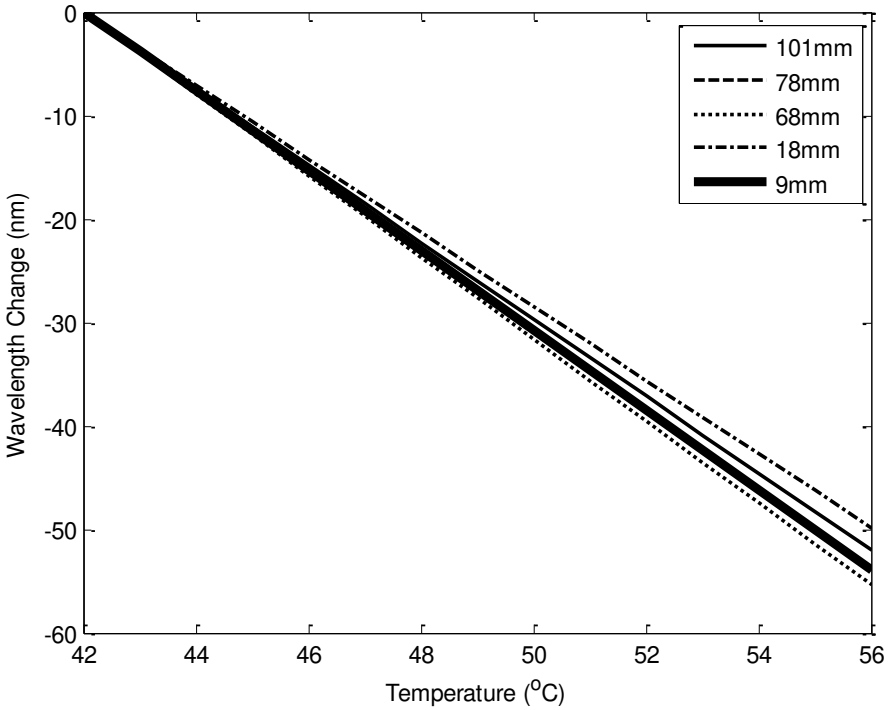

Figure 61: Linear regressions of the five different length devices.

5.4 Summary

A wide operating range temperature sensor using a PCF directional coupler structure is discussed. 6CHBT NLC is selectively infiltrated into one of the air hole of the PCF sensor for theoretical and experimental analysis. The device is fabricated and thermally tuned to investigate the thermal effect on the interference patterns.

The experiment reveals that the sensors' responses are dependent on the properties of NLC from 28.8 to 53.5 °C. The 6CHBT exhibits different refractive indices at different temperature regions corresponding to three different phases inside the NLC selectively filled PCF.

During the nematic phase between 28.8 °C to 36.3 °C, the data points of the resonance wavelength better fit a quadratic curve. The second-order polynomial relationships between the resonance wavelength and temperature, shown in Figure 53 and Figure 59, originate from the ordinary refractive index region of the 6CHBT as shown in Figure 39.

During the transition phase near 37.4 °C to 42.3 °C, the NLC selectively filled PCF experiences constant refractive index change between the ordinary refractive index region and isotropic refractive index region of the 6CHBT. The spectrum measured in time domain moves randomly as the transition phase. During the isotropic phase between 44 °C to 47.5 °C, the data points of the resonance wavelength fits a linear line and the corresponding temperature sensitivity is −3.72 nm/ °C. It operates in the near-linear isotropic refractive index region of the 6CHBT. The higher refractive index, as compared to silica, of the filled air hole leads to multimode propagation. It was found that the normalised frequency, V, is greater than 9.9 in the case of 6CHBT. This supports many higher order NLC core modes, and is defined by:

$$V = k_0 r \sqrt{n_{core,NLC}^2 - n_{clad}^2} = \frac{2\pi r}{\lambda} \sqrt{n_{core,NLC}^2 - n_{clad}^2}, \tag{26}$$

where $k_0 = \frac{2\pi}{\lambda}$ is the propagation constant, r is the air hole's radius, $n_{core,NLC}$ is the refractive index of the NLC and n_{clad} is the refractive index of the silica around the air hole.

Five different lengths of NLC selectively filled PCF are measured and show that as the length decreases the number of multipeaks in the resonance wavelength also decreases. The experimental result also shows that there is no significant change in the insertion loss. The five PCF lengths demonstrate temperature sensitivity ranging from −3.56 nm/ °C to −3.96 nm/ °C between 42 °C to 53 °C, in the isotropic phase. The measured mean and standard deviation temperature sensitivity are −3.79 nm/ °C and −0.153 nm/ °C, respectively. The measured temperature sensitivity show good agreement with the calculated temperature sensitivity of −3.27 nm/ °C. Using the refractive indices and temperature data from Figure 39, the theoretical refractive index sensitivity and refractive index resolution of the calculated model corresponds to −7201 nm/ RIU and -2.8×10^{-6}.

The measured mean temperature sensitivity is lower than prior work [110, 111] but its operating window demonstrated is an order higher. Wu *et al* have demonstrated a similar directional coupler using a small diameter, 125 µm endlessly single mode PCF and infiltrated index matching liquid, n = 1.50, with thermal coefficient of -3.86×10^{-4} RIU/ °C. They measured 11.61 nm/ °C over a temperature range of 50.7 °C to 51.7 °C (difference of 1.0 °C), which corresponds to 30100 nm/ RIU [110]. In another report, Wang *et al* have also demonstrated similar work (n = 1.46 index matching liquid and thermal coefficient of -3.89×10^{-4} RIU/ °C) achieving 54.3 nm/ °C covering a temperature range of 34.0 °C to 35.4 °C (difference of 1.4 °C) [111]. Another key difference with previous work is not using laser-assisted selective infiltration method to fill up one of the air hole with analyte liquid.

The performance of the sensor is determined by many physical parameters [112, 115, 114, 117] such as infiltrated air/liquid's physical properties, optical fibers' geometry and materials, selective infiltrated patterns, optical-fiber-to-optical-fiber splicing technique, etc. The spacing between the PCF's core and the single infiltrated air hole is one such parameter that changes the sensor performance. As the distance between the silica core and single infiltrated air hole increases, i.e. selective infiltrated to the next period of air hole, the coupling strength between the modes decreases resulting in a lower temperature sensitivity. When the air hole next to the PCF core is filled with medium such as glycerine [122], similar temperature sensitivity of −3.06 nm/ °C has been demonstrated. The performance of the device declines when the glycerine filled air hole is two or three periods away from the silica core at −2.12 nm/ °C and −0.11 nm/ °C, respectively.

6. Design and Analysis of Microfluidic Optical Fiber Device with Transverse Micro-Channel

6.1 Introduction

In the sixth chapter, the design and analysis of a microfluidic component is documented. A transverse micro-channel inside the single mode fiber is modelled using RSoft simulation software. Different geometry parameters are calculated, and an output power detection scheme is proposed to rapidly find the optimal fabrication-sensitivity design. Figure 62 and Figure 63 show the proposed schematic drawing of the microfluidic fiber device in this chapter.

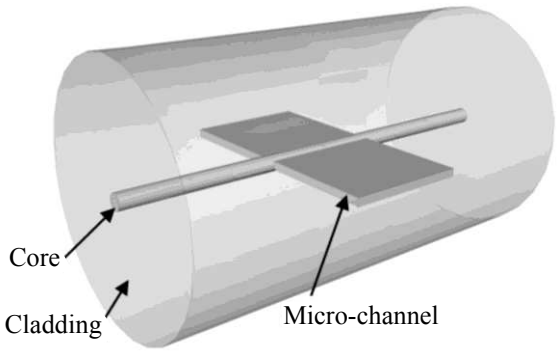

Figure 62: 3D schematic view of the microfluidic fiber device.

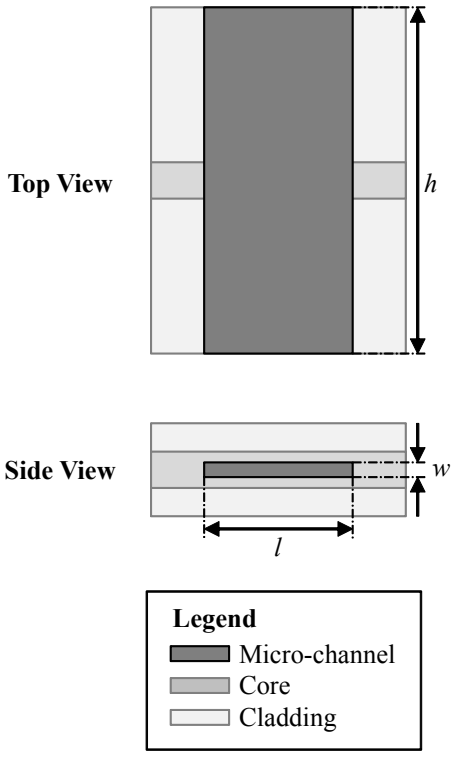

Figure 63: Top and side schematic view of the microfluidic fiber device.

6.2 Transverse Micro-Channel

Figure 64 shows the schematic drawing of the transverse micro-channel in a single mode fiber using RSoft simulation software. It consists of a rectangular transverse micro-channel intersecting across the core and cladding of the single mode fiber. The green region in Figure 64 is the cladding of the single mode fiber, and the yellow region is the core of single mode fiber. The grey region is the surrounding refractive index that varies for sensing. The red region is the micro-channel that has the same refractive index as the surrounding refractive index. A tiny orange region with a black triangular outline is the launch light and its direction. The purple

outline surrounding the entire region is the simulation boundary. The same colour coding scheme will be used throughout the chapter.

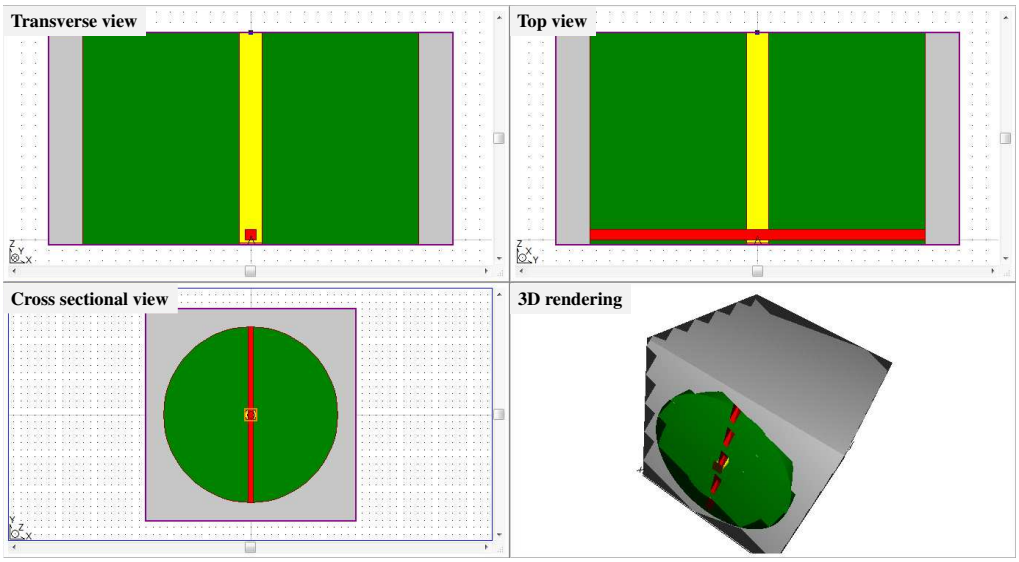

Figure 64: Screenshot of the RSoft three dimensional CAD drawing showing the transverse micro-channel in a single mode fiber. Upper left is the transverse view, upper right is the top view, lower left is the cross sectional view, and lower right is the 3D representation rendering.

The transverse micro-channel is quantified by its length (l) and width (w). For readability, the dimensions of the micro-channel are denoted as $l \times w$ in µm as shown in Figure 65. The depth of the transverse micro-channel is 125 µm, which is the diameter of a standard single mode fiber. The center of the transverse micro-channel aligns to the center of the single mode fiber.

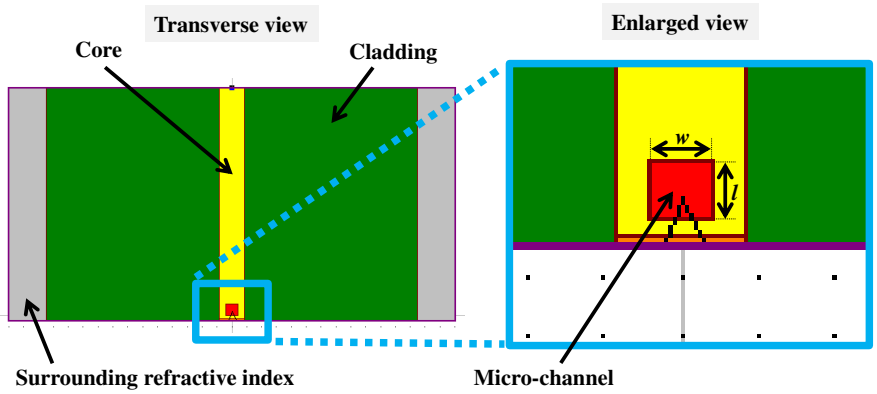

Figure 65: (a) Transverse view of the micro-channel in a single mode fiber with 125 µm cladding diameter. (b) Enlarge view at the transverse micro-channel outlined in blue box.

6.2.1 Operating Principle

Light propagates in the core of the single mode fiber. As it reaches the micro-channel, the propagating fundamental mode of the single mode fiber spreads throughout its cross section. This spread scatters light into the cladding of the

single mode fiber, and into the interface between the cladding and the surrounding medium.

At the cladding-surrounding medium interface, there is a loss of light from the single mode fiber due to refraction into the surrounding medium. Light that is not refracted is reflected from the interface back into the center of the single mode fiber where at the core and cladding interface experiences Fresnel's refraction and reflection. Light that is refracted propagates into the cladding of the single mode fiber again. The refraction and reflection interactions at the core and cladding interface slightly increase the intensity of the calculated power in the core, and at the cladding-surrounding medium interface decrease the intensity of the calculated total power in the single mode fiber.

The micro-channel also forms a Fabry–Pérot cavity. Input light is reflected multiple times at the single mode fiber and micro-channel interfaces. When the refractive index of the micro-channel matches the core guided mode, light transmitted across the micro-channel is maximised [123]. This is because there is little or no reflection at the single mode fiber and micro-channel interfaces.

Hence, light propagating in the micro-channel structure is influenced by the refractive index of micro-channel and surrounding medium. The interaction of light and change of the refractive index of analyte can be monitored by observing the intensity of the transmitted power through the micro-channel structure.

6.3 Result and Discussion

In this section, the following set of parameters in Table 9 is used for theoretical analysis in this thesis. The dynamic range and the effect of micro-channel length, width, and offset are investigated.

Parameter	**Value**
Length, *l* (μm)	50
Width, *w* (μm)	4
Refractive index of the core of SMF, n_{co}	1.4503
Refractive index of the cladding of SMF, n_{cl}	1.4436
Refractive index of analyte, n_{an}	Vary
Input wavelength (nm)	1550

Table 9: Set of parameters is investigated. The micro-channel and surrounding medium contain the same analyte.

6.3.1 Dynamic Range

Figure 66 shows the calculated transmitted power, *P*, through the micro-channel structure. The device displays oscillatory dependence on n_{an} from 1.0 to 1.6. The oscillatory shows two distinct refractive index regions from 1.00 to 1.42, and from 1.42 to 1.60. When $n_{an} < 1.42$, the micro-channel suffer significant scattering loss and the maxima of the interference pattern is ~7.5 dB. When $n_{an} > 1.42$, the micro-channel maxima improves to ~2 dB.

Figure 66 also plots the experimental data point of the research reported by J. Petrovic *et al* [123] for comparison. Their experimental result matches fairly close to the calculated result. However, the calculated oscillatory response of *P* could not be observed due to lack of measurement at smaller n_{an} step change. At discrete n_{an} ranges, *P* shows linearity as shown in the solid line of Figure 67.

As discussed in 4.4, many biosensing applications, particularly regarding certain tissues and agents, have refractive indices ranging from 1.334 to 1.455 [91, 94]. Often, biological tissues such as blood or protein are mixed with saline solution or phosphate buffered saline for analysis [124, 125]. For example, the refractive index of the mixture of blood (10% concentration) and saline solution decreases as it gets diluted to approximately 1.335 in the range of n_{an} = 1.330 to 1.336.

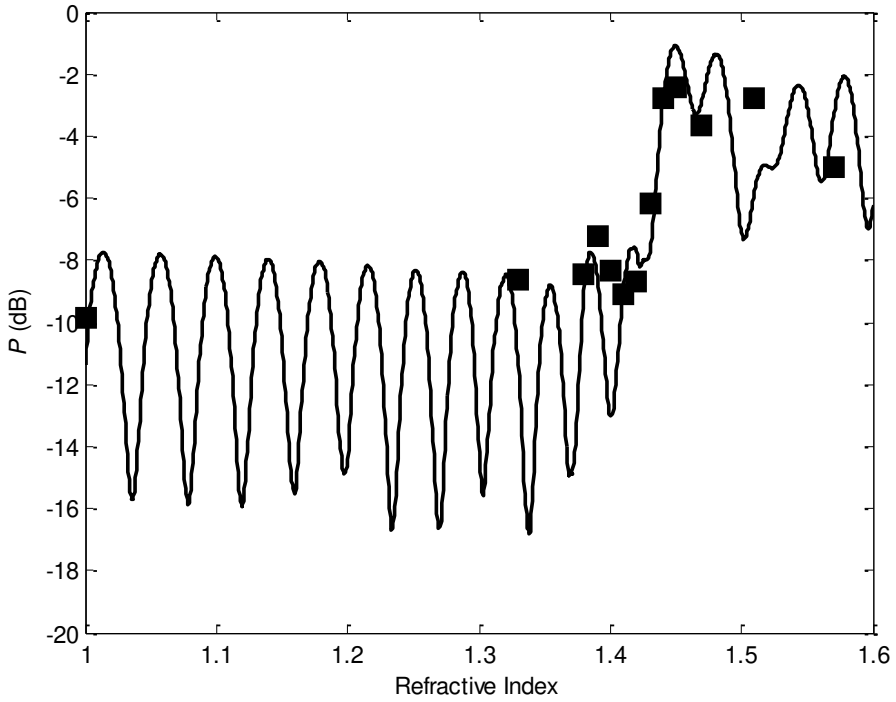

Figure 66: Transmission power for refractive indices between 1.00 to 1.60. Solid line denotes the calculated result. Square symbol denotes reported result from [123].

For a linear response device, the refractive index sensitivity can be determined by obtaining the dynamic range and the change in refractive index (ΔRI). The variation in P (ΔP), which is the amplitude change in P over two known refractive indices, is proposed as an output power detection scheme [126] to detect and measure n_{an}. The refractive index sensitivity of the device can be estimated as $\Delta P \times 100$ (dB)/ RIU.

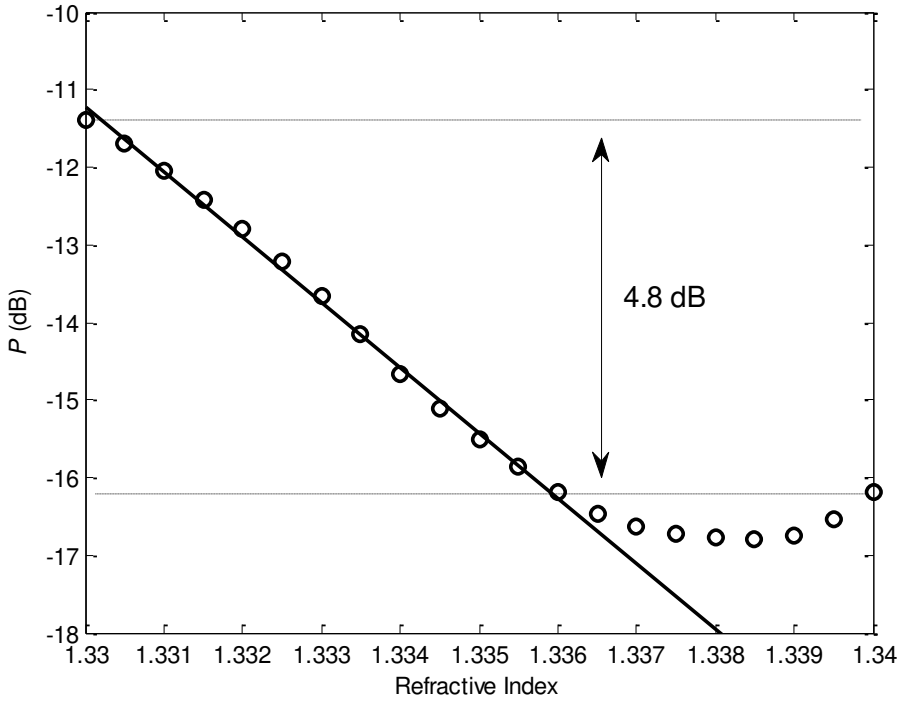

Figure 67: Transmission power for refractive indices between 1.330 to 1.340. Circle symbol denotes the calculated result. Solid line is the linear fit for the calculated result between 1.330 to 1.336.

The ΔP and ΔRI for Figure 67 are 4.8 dB and 0.01 respectively. Hence, the corresponding refractive index sensitivity is 480 dB/ RIU. Taking into account only the linear region of the response graph from 1.330 to 1.336 ($\Delta RI = 0.006$), the corresponding refractive index sensitivity improves to 800 dB/ RIU.

The improvement of the estimated refractive index sensitivity is 1.66 times better and is more practical due to its linear response. Nevertheless the scheme proposes a fast qualitative indication of the designed micro-channel structure.

The precision of the scheme depends on how well the corresponding refractive index response conforms to the linear refractive index window. There may be many sets of micro-channel dimensions suitable for refractive index sensing between 1.330 and 1.340. After separating out the potential sets, the most optimised micro-channel's design for high ΔP and high linearity can be converged.

To demonstrate the scheme, Figure 68 illustrates the intensity map of ΔP of n_{an} = 1.330 and 1.340 as a function of l and w. The intensity map indicates that ΔP varies significantly for different values of l and w. The most optimum dimension from the power detection scheme finds that the maximum ΔP is 58.1 dB at 80×4. It has an estimated refractive index sensitivity of 581 dB/ RIU.

The minimum ΔP = 0.000638 dB is found at 225×9, with an estimated device refractive index sensitivity of 0.0638 dB/ RIU. There are many ΔP hotspot in a series of bands concentrating at l < 100 μm and w = 4 μm at the bottom left of the intensity map. w < 2 μm generally displays very low ΔP for any practical detection purpose. For 100 < l < 300 μm, it is not feasible to fabricate high quality long structure and the ΔP is too low for consideration.

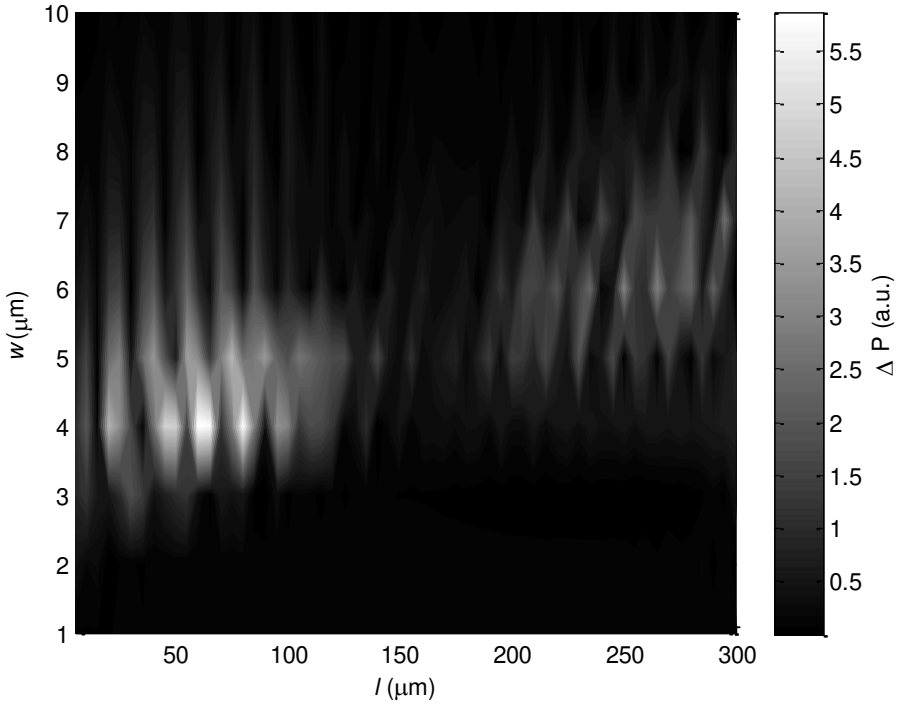

Figure 68: Power difference between refractive indices 1.330 and 1.340 for different channel length (l) and channel width (w). Grey bar shows the absolute power, ΔP, intensity in dB. Step change for w is 1 μm and for l is 5 μm.

Figure 69 shows three calculated P as a function of refractive index for three different reported dimensions for comparison. The refractive index span is from 1.330 to 1.340. The output power detection scheme estimated the refractive index sensitivity to be 581, 58.6 and 426.8 dB/ RIU for 80×4, 4×4 and 20×4, respectively [127, 128].

The linear region of 80×4 corresponds 761 dB/ RIU for refractive index between 1.333 to 1.339, a significant enhancement in sensitivity if the refractive index range is shortened. 4×4 has the least insertion loss and the least refractive index sensitivity.

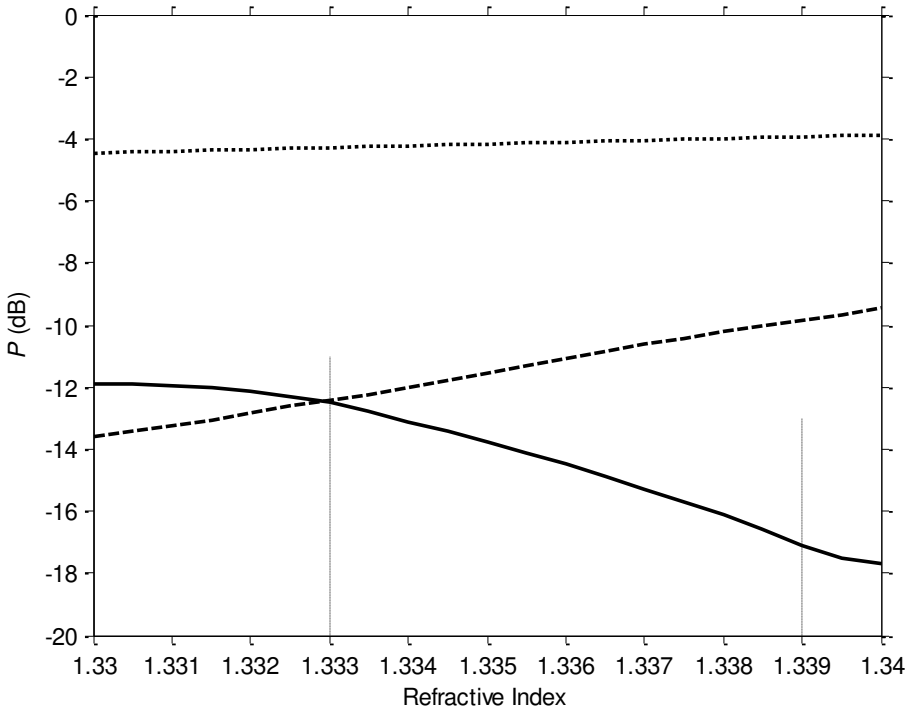

Figure 69: Calculated transmission power, *P*, for three different micro-channels' dimension as a function of refractive index. Solid line denotes 80×4. Dotted line denotes 4×4. Dashed line denotes 20×4.

6.3.2 Micro-Channel Length

To investigate how light propagate inside the micro-channel structure, a three dimensional model of micro-channel is simulated. n_{an} = 1.330 and w = 4 μm are set as constant for this part of the investigation. 15×4 has small ΔP; 50×4 and 80×4 have large ΔP.

Figure 70 shows the intensity of light propagating in the core of the single mode fiber and the overall intensity inside the single mode fiber over a propagation length z = 1000 μm. The micro-channel start from z = 0 μm.

Examining the partial power in the single mode fiber's core, as light propagate inside the micro-channel, P of the core decreases and stabilises at z = ~100 μm. The P of 50×4 and 80×4 decreases a further ~0.3 a.u. in amplitude more than 15×4. At z = ~350 μm from the reflection off the cladding-surrounding medium interface P of 50×4 and 80×4 has an obvious rise in core's P.

There is again a slight rise in the core's P at z = ~700 μm too. The phenomenon can also be observed in Figure 71, Figure 72 and Figure 73 by the reflected beam intersecting the core beam resulting in the increase in P at ~350 μm and ~700 μm.

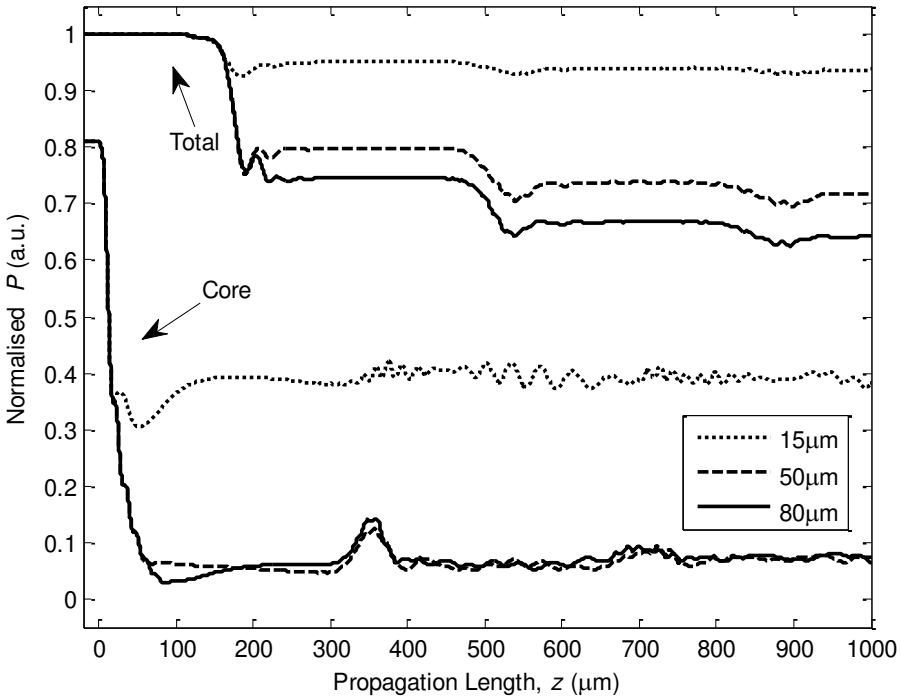

Figure 70: Power intensity along the whole propagation length with l = 15 μm, 50 μm, and 80 μm when w is fixed at 4 μm. Upper three lines are the total power in the single mode fiber and the micro-channel. Lower three lines are the partial power in the single mode fiber's core.

Next, the total power in the single mode fiber and the micro-channel is examined. For all three structures, the overall P starts to decrease dramatically and stabilises at z = ~200 μm. Later at z = ~550 μm, there is a slight decrease in amplitude again. The phenomenon can be seen in Figure 71, Figure 72 and Figure 73 by the refracted beam leaving the fiber at z = ~200 and ~550 μm. The third small refracted beam leaving the fiber at z = ~900 μm is barely visible.

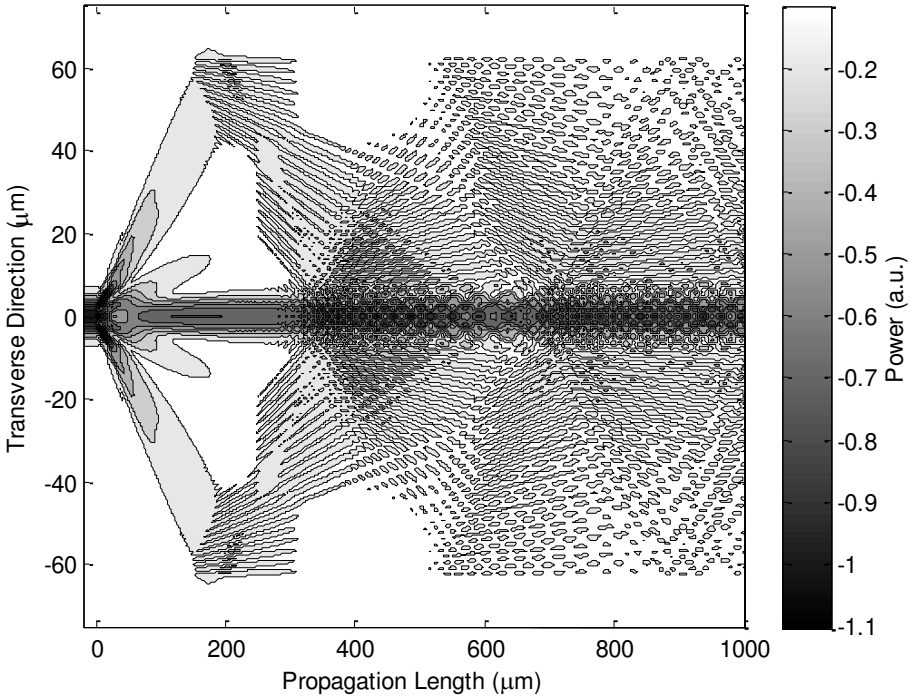

Figure 71: Beam propagation of 15×4 inside a single mode fiber.

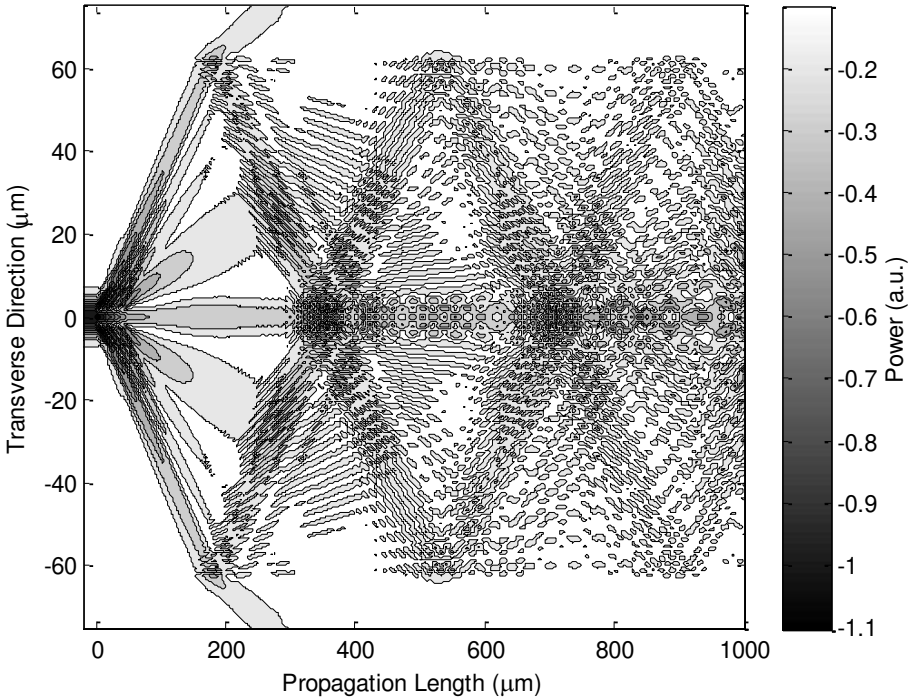

Figure 72: Beam propagation of 50×4 inside a single mode fiber.

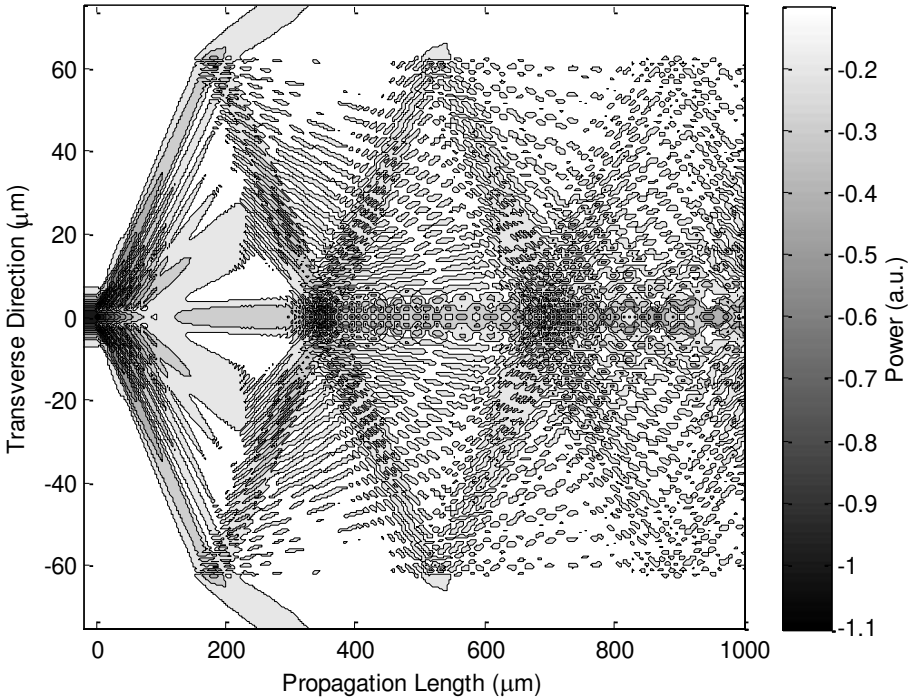

Figure 73: Beam propagation of 80×4 inside a single mode fiber.

The calculated results show that the structures exhibit similar trajectories at the two interfaces. 15×4 has most of its light energy concentrated inside the core of the single mode fiber and hence has the least insertion loss among the three structures.

50×4 and 80×4 propagate lesser light in their core but exhibits high light-fluid interaction at the two interfaces. The interaction results in more insertion loss than 15×4, and more importantly enhances the refractive index sensitivity to n_{an}. The refractive index sensitivity for the structure of 15×4, 50×4, and 80×4 are 17 dB/ RIU, 480 dB/ RIU, and 581 dB/ RIU respectively.

When there is more interaction at the two interfaces, we observe a significant increase in the refractive index response to refractive index changes in the surrounding medium. This insertion loss and refractive index sensitivity tradeoff is a design consideration. Overall, 50×4 and 80×4 displays a very similar propagation profile, providing the device designer an alternative for either one.

Figure 74 shows how much power is in the micro-channel from $z = -20$ μm to 100 μm for different l. The micro-channel start at $z = 0$ μm as a reference. The propagation intensity profiles for $l = 15$ μm, 50 μm, and 80 μm overlay one another. All three structures show identical propagation profile limited by the length of the micro-channel. The profile displays step-like decrement along the length of the micro-channel.

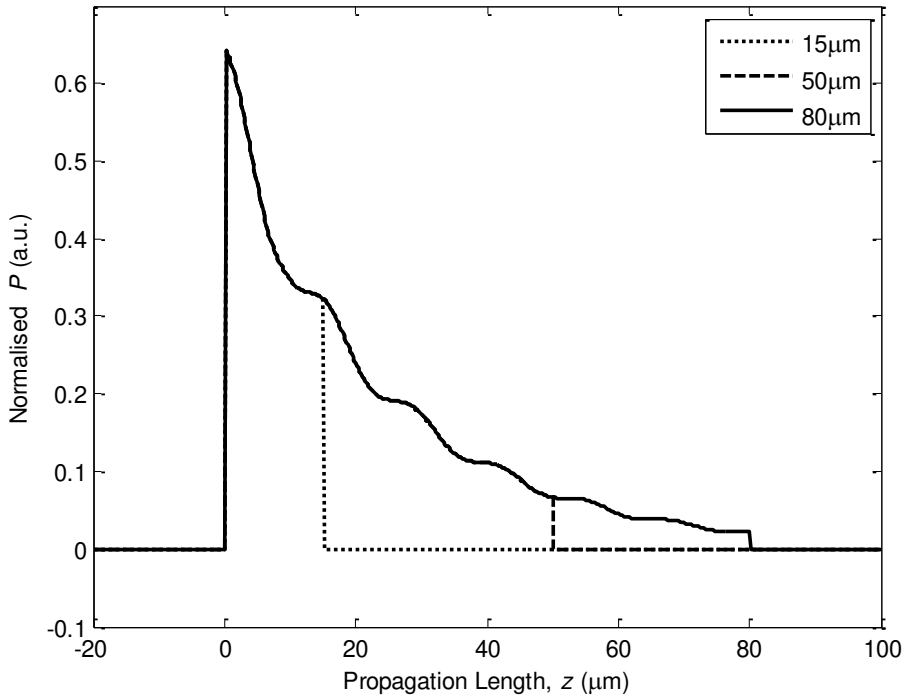

Figure 74: Power intensity inside the channel with l = 15, 50, and 80 μm when w is fixed at 4 μm.

6.3.3 Micro-Channel Width

In the next part of the investigation, n_{an} = 1.330 and l = 80 μm are set as constant to observe how light propagate inside the micro-channel for different w. The power intensity along the single mode fiber is plotted in Figure 75. 80×2 has small ΔP; 80×4 and 80×5 have large ΔP and high refractive index sensitivity.

80×2 exhibits the least insertion loss for both the total power in the optical fiber and the power in the single mode fiber's core. 80×4 and 80×5 both

displays similar insertion loss profile higher than 80×2 along the single mode fiber. The similar phenomenon in Figure 70 increase in *P* is also observed for 80×4 and 80×5 as depicted in Figure 75.

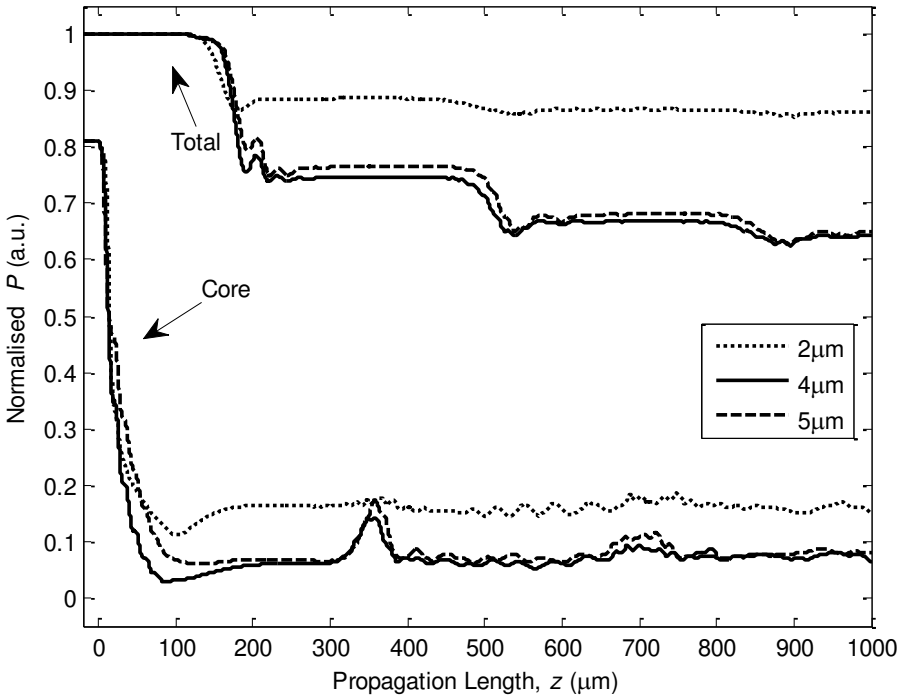

Figure 75: Power intensity along the whole propagation length with $w = 2$ μm, 4 μm, and 5 μm when l is fixed at 80 μm. Upper three lines are the total power in the single mode fiber and the micro-channel. Lower three lines are the partial power in the single mode fiber's core.

Figure 76 shows how much power is in the micro-channel from $z = -20$ μm to 100 μm for different w. All the three micro-channels show different propagation profiles even though l is fixed at 80 μm. 80×2 shows the least power in the micro-channel follow by 80×4 and then by 80×5. 80×2 reaches $P = 0$ around $z = 20$, while 80×4 and 80×5 never reach $P = 0$.

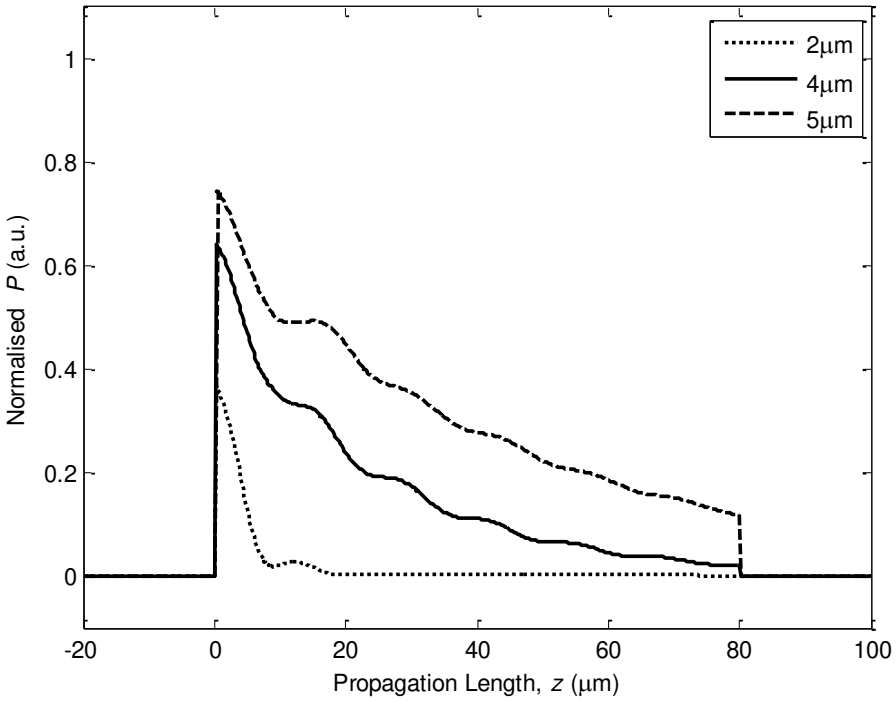

Figure 76: Power intensity inside the channel with $w = 2$ μm, 4 μm, and 5 μm when l is fixed at 80 μm.

Likewise a similar phenomenon of the reflected beam intersecting the core beam, in Figure 71 to and Figure 73, is also observed in Figure 77 and Figure

78. Trajectories at the two interfaces occur. Beam propagation of 80×2 exhibits very low intensity in the micro-channel and a significant amount of intensity surrounding the near region of the micro-channel.

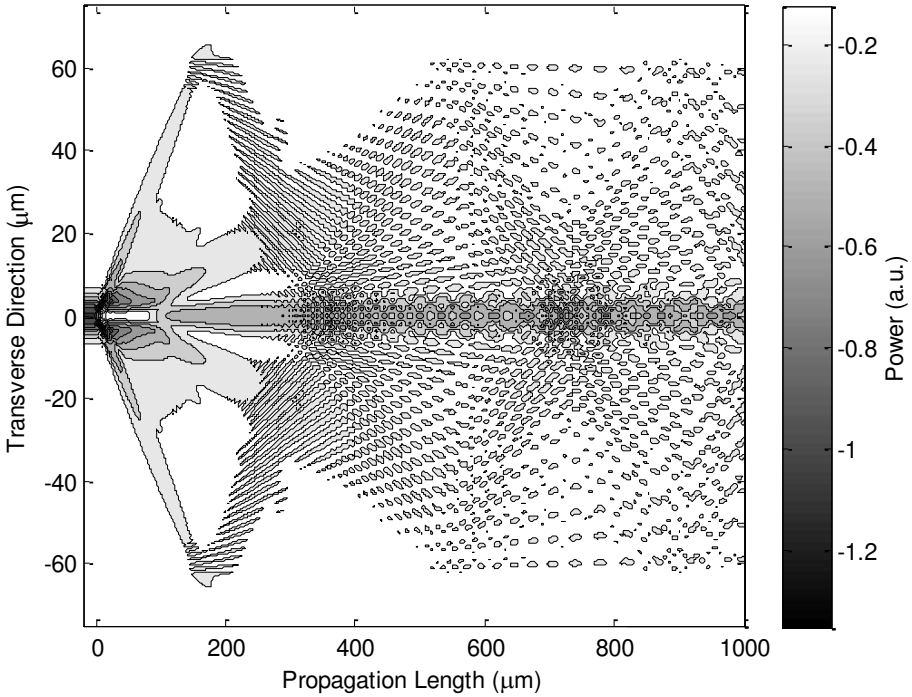

Figure 77: Beam propagation of 80×2 inside a single mode fiber

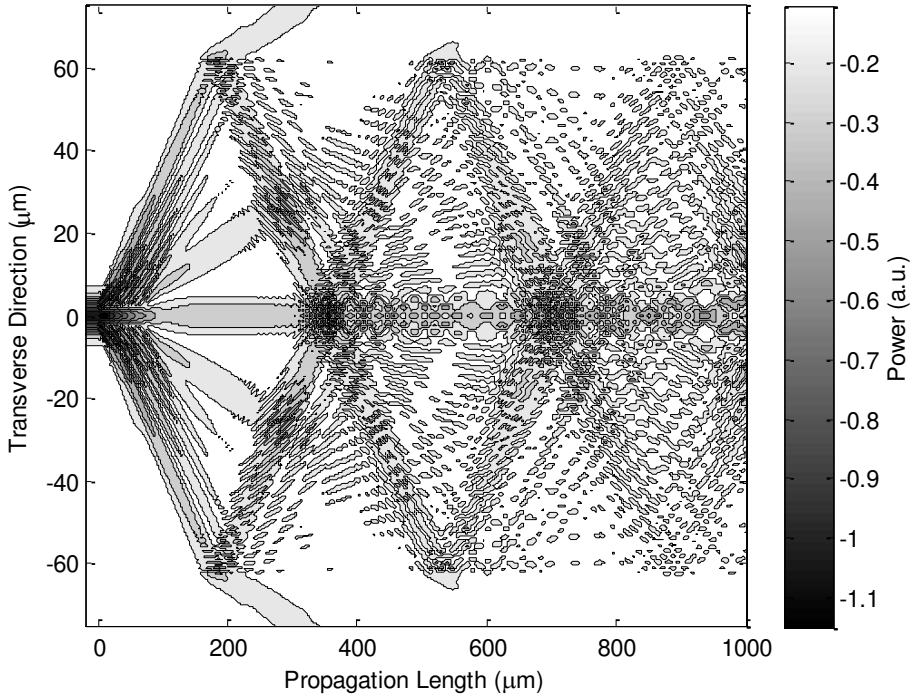

Figure 78: Beam propagation of 80×5 inside a single mode fiber.

The calculated refractive index sensitivity of 80×2, 80×4 and 80×5 are 17 dB/ RIU, 581 dB/ RIU and 251 dB/ RIU respectively. Again we observe that if there is more light-fluid interaction at the two interfaces, the corresponding refractive index sensitivity to n_{an} will be higher.

The five investigated micro-channels' refractive index response to the change in n_{an}, is plotted in Figure 79, for comparison. The channel dimension are 80×2 (green solid line), 15×4 (green dashed line), 80×4 (black solid line), 80×5 (red dash-dotted line), and 50×4 (blue dotted line).

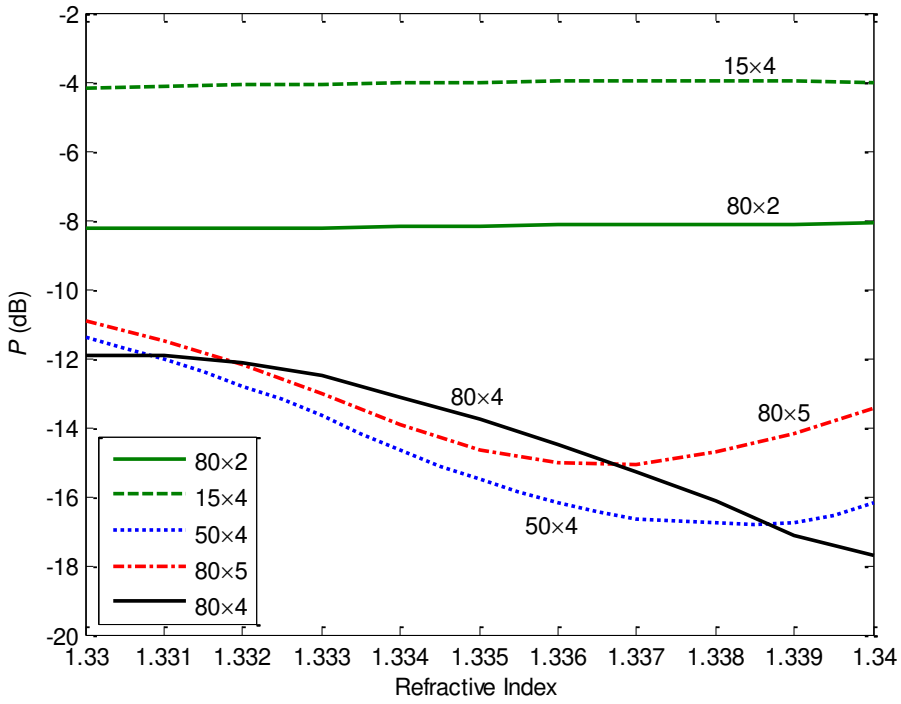

Figure 79: Refractive index sensitivity curves for five types of channel dimension.

80×2 and 15×4 display an almost horizontal line response corresponding to a very low sensitivity. Their insertion loss is lesser compared with the other three micro-channels, which display non-linear refractive index responses. A

linear fit is applied to get a practical range and the refractive index sensitivity is plotted in Table 10.

Micro-channels Dimension	**Span of Refractive Index**	**Refractive Index Sensitivity (dB/ RIU)**
80×4	1.333 to 1.339	761
50×4	1.333 to 1.336	845
80×5	1.333 to 1.336	681

Table 10: Refractive index response of micro-channels.

6.3.4 Micro-Channel Off-Center

The off-center micro-channel position, *y*, is the separation distance of the center axis of the micro-channel to the single mode fiber's core as illustrated in Figure 80. As *y* increases, the micro-channel will gradually shift out of the single mode fiber's core.

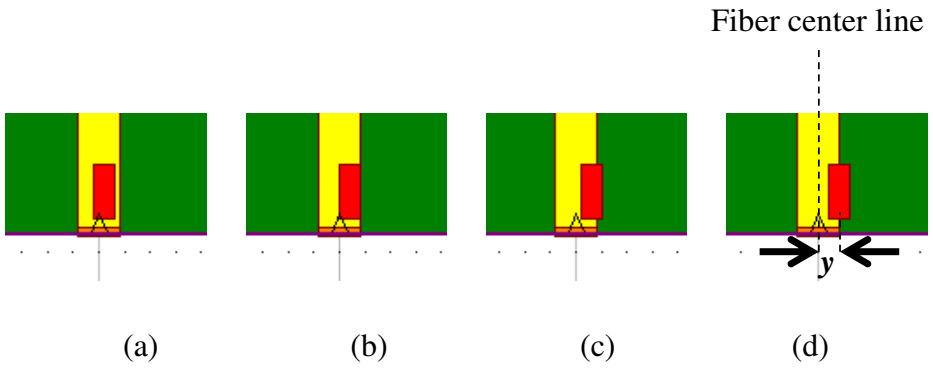

Figure 80: Micro-channel at (a) 10 µm, (b) 20 µm, (c) 30 µm, and (d) 40 µm offset from the center of the core.

The dimension of the highest refractive index sensitivity from Table 10 is simulated to investigate the effect of *y* on the refractive index sensitivity. The refractive index responses for y = 0 µm to 8 µm and refractive index from 1.330 to 1.340 of 80×4 are plotted in Figure 81. The surface plot shows that when *y* is about 2 µm, there is a visible horizontal gradient. Above 2 µm, there is no significant horizontal colour gradient.

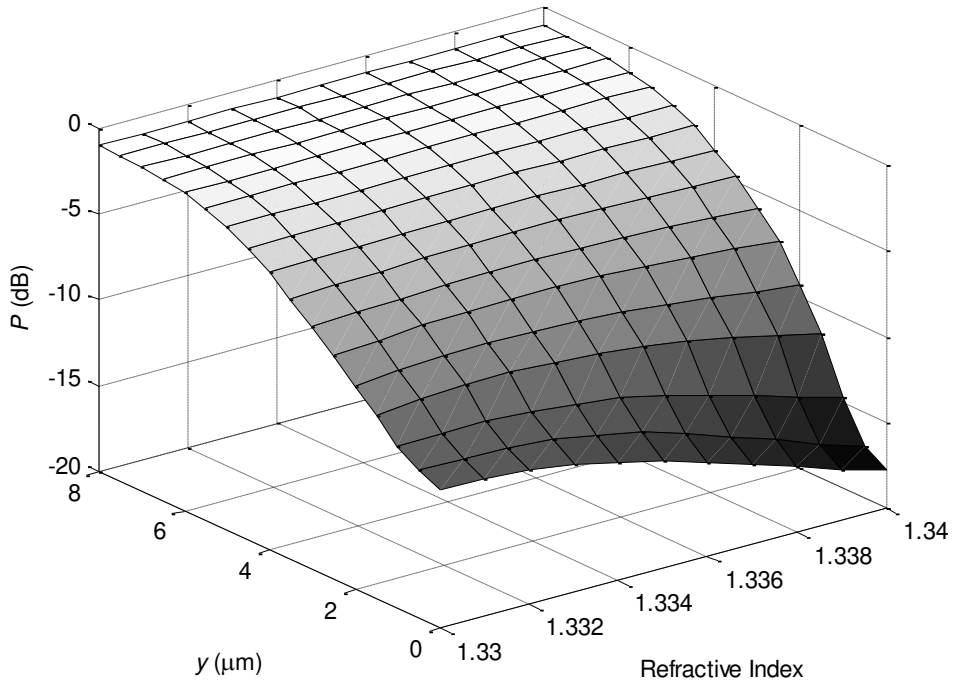

Figure 81: Surface plot of the transmission power with varying offset from 0 μm to 8 μm. The colour bar on the right shows the transmission power in dB. The micro-channel dimension is 80×4.

When y increase from 0 *μm to* 1.5 μm, the micro-channel is still within the region of the single mode fiber's core. There is lesser insertion loss. P increases a few dB across the refractive index range of 1.330 to 1.340. However, the gradient decreases. When y = 8 μm, the micro-channel is entirely outside the region of the single mode fiber's core. P is approximately −1 dB across the refractive index range of 1.330 to 1.340 with almost no visible gradient. Figure 82 depicts light propagating inside the micro-channel

structure with different y. The calculated parameters are n_{an} = 1.330, l = 4 μm and w = 80 μm. The solid lines are y = 0 μm, as reference. For y = 1.5 μm, the intensity follows closely to y = 0 μm. However, when y = 8 μm the intensity remains relatively same to the input intensity.

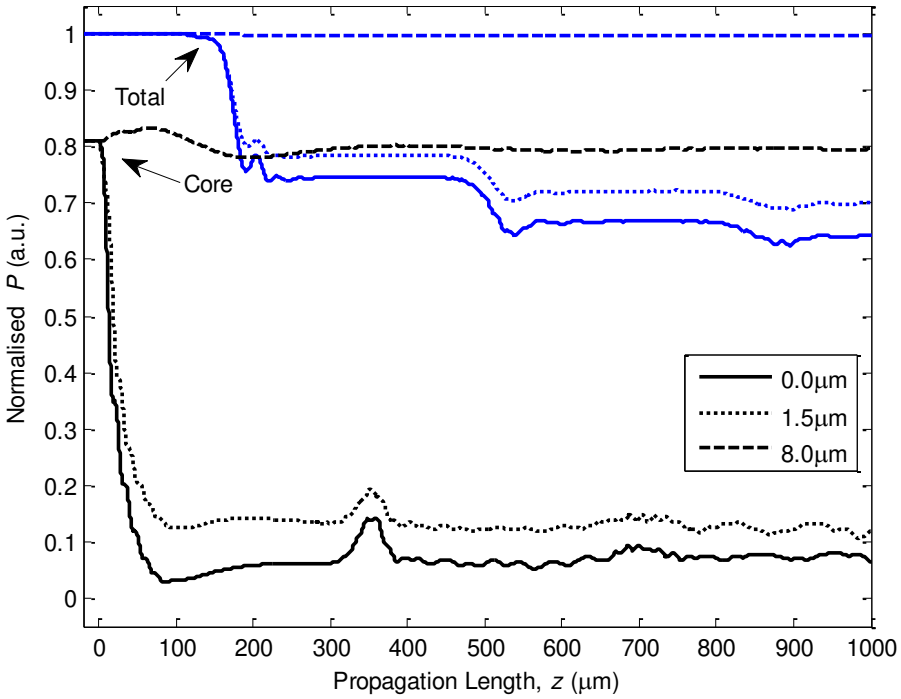

Figure 82: Power intensities along the 1000 μm propagation length when varying the offset 0 μm (solid lines), 1.5 μm (dotted lines), and 8 μm (dashed lines). Blue lines are the total power in the fiber. Black lines are the power in the single mode fiber's core. The micro-channel dimension is 80×4.

Figure 83 shows how much power is in the micro-channel from $z = -20$ μm to 100 μm for different y. The micro-channel starts from $z = 0$ μm to $z = 80$ μm. Again, we find that $y = 1.5$ μm resembles closely to $y = 0$ μm and the profile displays a step-like decrement along the length of the micro-channel. $y = 8$ μm displays very little amount of power in the core, which explains why its refractive index response is almost zero. This shows that there is too little light-analyte interaction in the micro-channel for $y = 8$ μm.

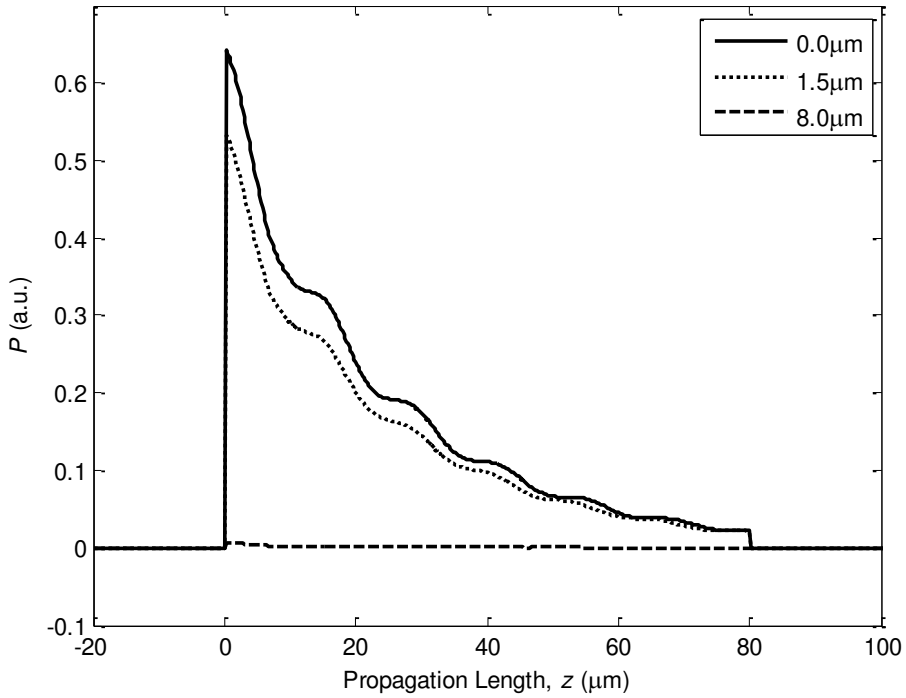

Figure 83: Power intensities inside the channel when varying $y = 0$ μm (solid line), 1.5 μm (dotted line), and 8 μm (dashed line). The micro-channel dimension is 80×4.

Lastly, the variation in P between refractive index 1.33 and 1.34 is plotted in Figure 84, derived from Figure 81.

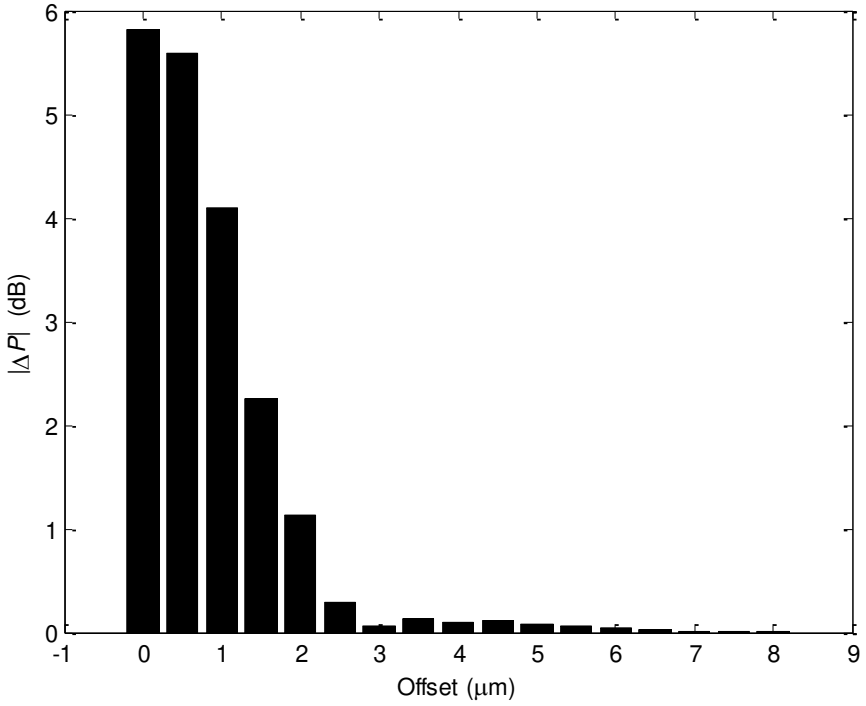

Figure 84: Transmission difference between refractive index 1.33 and 1.34 for offset 0 μm to 8 μm. The micro-channel dimension is 80×4.

The results show that when the micro-channel shifts further away from the center of the single mode fiber, it is also moving away from the core where the guided mode is. There is less light interference and scattering leading to a lower loss. Also observed is that ΔP decreases and the gradient gradually

flattens. The maximum refractive index sensitivity is at y = 0 μm without any offset, which is aligned in the middle of the single mode fiber core.

6.4 Summary

In this chapter, the micro-channel structure and how the geometry affects the light-fluid interaction has been discussed. The investigation shows that the micro-channel structure's length, width, and offset position, and the refractive index of the analyte in the micro-channel influence the transmission.

The calculated transmission results, as shown in Figure 66, are in good agreement with the experimental results from [123]. Scanning the refractive indices over a wider range (from 1.00 to 1.6) and with a finer step change (0.0005), an oscillating transmission response as a function of refractive indices is found from the numerical simulation. The reported experimental result does not show the oscillation due to the coarse step size of the refractive index and also probably due to the challenge of obtaining obtain a suitable refractive index liquid material.

The key takeaway is that an output power detection can scheme quickly estimate the refractive index response of a defined geometry of the micro-channel. Observing Figure 68, it can be seen that for a given refractive index range, when the width of the micro-channel is less than 10 μm, there are certain regions where the ΔP is high or low depending on the dimension of the micro-channel. From the power detection scheme, the proposed most optimum dimension for refractive

indices 1.330 to 1.340 is 80×4, with an estimated refractive index sensitivity of 581 dB/ RIU for a rectangular shaped micro-channel through the core of standard single mode fiber. The corresponding theoretical refractive index resolution is 6.9×10^{-4} when the level accuracy is 0.4 dB and analyte required to fill up the micro-channel is about several tens of picolitres. Assuming a high performance power detector is used, such as 0.01 dB, the theoretical refractive index resolution could reach 1.7×10^{-5}.

Comparing with those found in Table 3 and Table 8, the theoretical refractive index resolution is at the middle range of the sensors.

The Femtosecond Laser Irradiation followed by Chemical Etching (FLICE) [129] microfabrication technique has the potential to make the 80×4 structure inside the single mode fiber. It is a maskless technology that uses femtosecond laser pulses to irradiate moderate fluence structures inside the optical fiber, followed by etching of the laser modified zone. The moderate fluence produces sub-wavelength nanocracks that yields the best etching condition for the micro-channel. Hydrofluoric acid (HF), typically used as the etching solution, will etch more rapidly into the nanocracks at the irradiated region than the silica in contact with the acid. Hence, high aspect ratio micro-channel can be realized with FLICE.

J. Petrovic *et al* reported that when w is three times smaller than l, the micro-channel works as a scatterer of light guided by the core [123]. The proposed optimum dimension length is twenty times its width. The micro-channel is also the main contributor for insertion loss. After the light is scattered, it propagates

throughout the micro-channel, and the optical fiber's core and cladding boundaries experiences multiple Fresnel reflections and refractions. The reflected light periodically travels to the core, causing power of the core to oscillate, as shown in Figure 70 and Figure 75. At the cladding-surrounding medium interface, light leaks out of the optical fiber causing the total power in the single mode fiber and the micro-channel to drop.

Another fabrication technique, without using a femtosecond laser places a square glass capillary in between two single mode fibers for sensing a change in refractive index [128]. The capillary is tapered to an inner width of 10 µm and an outer width of 80 µm and chemically treated in order to improve the device's performance. The Mach-Zehnder interferometer based device may face challenges for practical usage especially when handling the 80 µm tapered capillary together with the two aligned optical fibers. In contrast, the proposed microfluidic optical fiber device preserves the 125 µm cladding structure, ensuring mechanical strength greater than that of the 80 µm thinned optical fiber type.

When designing and fabricating the micro-channel structure, considerations have to be made for the refractive index response, insertion loss, the geometries, surface finish, etc. The discussion provides some insight into the possible near water refractive index sensor fabrication geometries for the microfluidic optical fiber device.

7. Thesis Conclusion and Recommendation for Future Work

7.1 Thesis Conclusion

In conclusion, the thesis has presented three different optical fiber modification methods over four chapters for fabricate high performance optical fiber sensors. The results and discussions concentrate on how the fabrication methodologies could yield viable optical fiber sensor without costly machinery and yet still achieve comparably high sensitivity sensors to those available in the market. Majority of the work uses Photonic Crystal Fibers (PCF) or microstructured optical fibers to experimentally and theoretically investigate PCF sensors for refractive index and temperature sensing. As discussed in Chapter 2, the use of PCFs will generally yield higher sensitivity sensor compared to conventional optical fibers because of PCFs' unconventional propagation properties. The major contributions and organisation of the thesis are discussed in 1.4 and 1.5 respectively.

The research uses two microbubbles as in-fiber lenses to scatter light to form a modal interferometer for refractive index sensing by an external cladding sensing mechanism. This modal interferometer type of in-line microbubble PCF sensor is the first of its kind for refractive index sensing – to the best of the author's knowledge. A fusion splicer machine is used to fabricate the in-line microbubble PCF sensor by the microhole collapsing technique. The formation of the

microbubble is highly repeatable and its size is highly controllable, as discussed in Chapter 3.

In Chapter 4, three application demonstrations using four different samples of in-line microbubble PCF sensors, namely Sensor A, B, C, and D, were presented. Firstly, Sensors A and B demonstrate the trade-off for multiplexed refractive index sensors. Secondly, a dual parameter sensor, made using a LPG and Sensor C, demonstrates that it can simultaneously sense refractive index and temperature with very high accuracy. Thirdly, a biosensor, using Sensor D, for detecting biotin-streptavidin binding has been demonstrated. A thorough search of the relevant literature yielded that the work is first of its kind utilizing a PCF-based modal interferometer. The transmission based setup of the in-line microbubble PCF sensors (ranging from 166 nm/RIU to 320 nm/ RIU) is higher than the reflective based setup (11.5 nm/ RIU). It should be noted that the PCF's length used to fabricate the in-line microbubble PCF sensor is very short, in the range of a few millimetres compared with prior work. The modification method on PCF could yield theoretical refractive index resolution of 6.25×10^{-5}.

Likewise in Chapter 5, the development, fabrication technique and operating principle of the directional coupler structure have been investigated. Glue is applied to block the air holes of the PCF during the selective infiltration fabrication method. Many different patterns of selective infiltrated design have been illustrated. The design of one-hole filled with nematic liquid crystal has been further investigated and characterised. The temperature response of the theoretical mode

coupling results, calculated using Lumerical Mode Solutions, is in line with the experimental results. It shows that the nematic liquid crystal is highly temperature dependent, the interference patterns changes in different phase of liquid crystal, and the various infiltration length generate different interference patterns. This modification method could yield a theoretical refractive index resolution of -2.8×10^{-6}.

In Chapter 6, a transverse micro-channel structure inside the single mode fiber is calculated using RSoft BeamPROP for its influence refractive index sensing on various length, width and off-set parameters. The output power detection scheme provides a rapid way to select the most optimal geometry-sensitivity design. The Femtosecond Laser Irradiation followed by Chemical Etching (FLICE) microfabrication is an existing technique that could be used to fabricate and investigate the proposed geometry-sensitivity design. Compared with other similar work, the 125 μm cladding structure provides a better mechanical strength over thinner structure. The modification method on single mode fiber could yield a theoretical refractive index resolution of 1.7×10^{-5}.

7.2 Recommendations for Future Research

Many opportunities for extending the scope of this thesis are possible but it is time consuming and resource intensive. The first recommendation is to further investigate numerically the in-line microbubble PCF sensor on its resonance wavelength and its fundamental connection to the two microbubbles. An optical

fiber sensor that has an interference pattern resembling those of an LPG and is highly sensitive to the surrounding refractive index is highly valuable and beneficial. The outcome may yield a sensor with a strongly coupled resonance wavelength, which may favour manufacturing and production. The second recommendation is to investigate other parameters influencing the in-line microbubble PCF sensor, such as strain and pressure, and whether other commercial available PCFs are able to yield a similar or better refractive index sensitivity at the near water refractive index. In addition to the intensive theoretical investigation, by numerical method such as FDTD simulation, the effort in seeking more understanding about the in-line microbubble PCF sensor may solve the issue of high insertion loss found in the current work. This work can benefit the potential manufacturer, such as the use case for label-less biosensor to use cheaper detector devices.

The third recommendation is to simplify the infiltration process. A new PCF can be designed and fabricated enabling direct infiltration of fluid or gases without the need to block the air holes of the PCF. For example, an all-solid PCF may be fabricated with a single air hole for the infiltration process. The doped regions will have to be designed properly to guide the light-fluid interaction as well as confine light inside the PCF and couple light in-and-out of the PCF. This work can benefit the fabrication of the sensor as there is no need for a bulky laser, reducing the setup costs.

The last recommendation is to validate the optical transverse micro-channel. Femtosecond Laser Irradiation followed by Chemical Etching (FLICE) [129] is fabrication technique used to fabricate micro-structures. Marcinkevičius *et al* and Vishnubhatla *et al* had demonstrated [129, 130], by FLICE, that a three-dimensional micro-channel is able to be fabricated in silica material. Later, Lai *et al* used an additional glass slip attachment to make a micro-channel inside single mode fiber [131]. Leveraging on those techniques to fabricate almost any shape and size of micro-channel, the final proposed area of further research can demonstrate and validate the most-optimal geometry of the RSoft BeamPROP calculations, and expand into more complex micro-channels or micro-structures. The precision of the femtosecond laser inscription and the widening of the micro-channel at the opening from the chemical process may affect the refractive index response. Hence, further research can also investigate the effect of those parameters that will benefit the implementation of the microfluidic device.

Publications

List of author's publication in chronological order:

1. **J. L. Lim**, D. J. J. Hu, P. P. Shum, and Y. Wang, "Temperature Response of Polarization-Maintaining Photonic Crystal Fiber based Interferometer", *in Proc. of IEEE Microwave Photonics (MWP) Conference*, Singapore, 2011.

2. D. J. J. Hu, **J. L. Lim**, Y. Wang, and P. P. Shum, "Miniaturized photonic crystal fiber tip sensor for refractive index sensing", *in Proc. of IEEE Sensors Conference*, Ireland, 2011.

3. **J. L. Lim**, D. J. J. Hu, P. P. Shum, and Y. Wang, "Cascaded Photonic Crystal Fiber Interferometers for Refractive Index Sensing", *IEEE Photonic Journal*, vol. 4, no. 4, pp. 1163–1169, Aug. 2012.

4. **J. L. Lim**, D. J. J. Hu, P. P. Shum, Y. Wang, and E. J. Hao, "Microbubble-Enabled Photonic Crystal Fiber-based Sensors", *in Proc. of Photonics Global Conference (PGC)*, Singapore, 2012.

5. **J. L. Lim**, D. J. J. Hu, D. Cui, S. Yoo, P. P. Shum, and W. Loh, "Characteristics of Suspended-Core Fiber Interferometer: Modal Analysis", *in Proc. of Photonics Global Conference (PGC)*, Singapore, 2012.

6. D. J. J. Hu, **J. L. Lim**, M Jiang, Y. Wang, and W. Tong, "Long period grating cascaded to photonic crystal fiber modal interferometer for

simultaneous measurement of temperature and refractive index ”, *Optics Letters (OL)*, vol. 37, no. 12, pp. 2283–2285, Jun. 2012.

7. D. J. J. Hu, **J. L. Lim**, Y. Cui, K. Milenko, Y. Wang, P. P. Shum, and T. Wolinski, “Fabrication and characterization of a highly temperature sensitive device based on nematic liquid crystal filled photonic crystal fiber”, *IEEE Photonic Journal*, vol. 4, no. 5, pp. 1248–1255, Oct. 2012.

8. D. J. J. Hu, P. P. Shum, **J. L. Lim**, Y. Cui, K. Milenko, Y. Wang, and T. Wolinski, “A Compact and Temperature-Sensitive Directional Coupler Based on Photonic Crystal Fiber Filled With Liquid Crystal 6CHBT”, *IEEE Photonic Journal*, vol. 4, no. 5, pp. 2010–2016, Oct. 2012.

9. D. J. J. Hu, Y. Cui, **J. L. Lim**, P. P. Shum, G. Humbert, J. Auguste, and Y. Wang, “Design and fabrication of a holey fiber microfluidic device with transverse micro-channel”, *Photonics Letters of Poland*, vol. 6, no. 2, pp. 53–55, Jun. 2014.

10. **J. L. Lim**, D. J. J. Hu, P. P. Shum, and Y. Wang, “Design and Analysis of Microfluidic Optical Fiber Device for Refractive Index Sensing,” *IEEE Photonic Technology Letters*, vol. 26, no. 21, pp. 2130–2133, Nov. 2014.

11. **J. L. Lim***, K. Li*, D. J. J. Hu, P. P. Shum, E. J. Hao, Y. Wang, and M. Jiang, “Investigation of Temperature Sensitivity Under the Influence of Coupling Strength Between a Silica Core and a Satellite Waveguide in a

Photonic Crystal Fiber with Selective Infiltration of Nematic Liquid Crystal," *in Proc. of Photonics Global Conference (PGC)*, Singapore, 2015.

12. **J. L. Lim***, K. Li*, Z. Xu, D. J. J. Hu, R. Y.-N. Wong, P. P. Shum, E. J. Hao, Y. Wang, Q. Sun, and M. Jiang, "Investigation of temperature sensitivity under the influence of coupling strength between a silica core and a satellite waveguide in a photonic crystal fiber with selective infiltration of glycerin," *Procedia Engineering*, vol. 140, pp. 72–76, 2016.

13. **J. L. Lim***, Z. Xu*, D. J. J. Hu, Q. Sun, R. Y.-N. Wong, K. Li, M. Jiang, and P. P. Shum, "Investigation of temperature sensing characteristics in selectively infiltrated photonic crystal fiber," *Optics Express (OE)*, vol. 24, no. 2, pp. 1699–1707, Jan. 2016.

* denotes joint-first authorship

References

The list of cited references in this thesis is as follows:

[1] J. C. Knight, T. A. Birks, P. S. J. Russell and D. M. Atkin, "All-silica single-mode optical fiber with photonic crystal cladding," *Opt. Lett.,* vol. 21, no. 19, pp. 1547-1549, 1996.

[2] M. Walton, K. Eremin, A. Shortland, P. Degryse and S. Kirk, "Analysis of late bronze age glass axes from nippur - a new cobalt colourant," *Archaeometry,* vol. 54, no. 5, pp. 835-852, 2012.

[3] D. B. Keck and P. C. Schultz, "Method of producing optical Waveguide fibers". USA Patent 3,711,262, 16 Jan 1973.

[4] K. C. Kao and G. A. Hockham, "Dielectric-fibre surface waveguides for optical frequencies," *Proc. of IEE,* vol. 133, no. 7, pp. 1151-1158, 1966.

[5] L. Xiao, M. S. Demokan, W. Jin, Y. Wang and C.-L. Zhao, "Fusion Splicing Photonic Crystal Fibers and Conventional Single-Mode Fibers: Microhole Collapse Effect," *J. Lightw. Technol.,* vol. 25, no. 11, p. 3563−3574, 2007.

[6] J. Ju, W. Jin, Y. L. Hoo and M. S. Memokan, "A simple method for estimating the splice loss of photonic-crystal fiber/single-mode fiber," *Microwave and Opt. Techno. Lett.,* vol. 42, no. 2, pp. 171-173, 2004.

[7] Y. L. Hoo, W. Jin and H. L. Ho, "Loss analysis of single-mode fiber/photonic-crystal fiber splice," *Microwave and Opt. Techno. Lett.,* vol. 40, no. 5, pp. 378-380, 2004.

[8] P. V. Kaiser and H. W. Astle, "Low-loss single-material fibers made from pure fused silica," *The Bell System Technical Journal,* vol. 53, no. 6, p. 1021–1039, 1974.

[9] E. Hecht, "Interference," in *Optics*, San Francisco, Addison Wesley, 2002, pp. 385-389.

[10] E. Udd, "An overview of fiber-optic sensors," *Rev. Sci. Instrum.,* vol. 66, no. 8, pp. 4015-4030, 1995.

[11] X. Shu, L. Zhang and I. Bennion, "Sensitivity Characteristics of Long-Period Fiber Gratings," *Journal of Lightware Techno.,* vol. 20, no. 2, pp. 255-266, 2002.

[12] P. Hoffmann, B. Dutoit and R.-P. Salathe, "Comparison of mechanically drawn and protection layer chemically etched optical fiber tips,"

Ultramicroscopy, vol. 61, no. 1-4, pp. 165-170, 1995.

[13] M. Ozcan, A. Allahbeickaraghi and M. Dündar, "Possible hazardous effects of hydrofluoric acid and recommendations for treatment approach: a review," *Clin Oral Invest,* vol. 16, no. 1, pp. 15-23, 2012.

[14] V. R. Machavaram, R. A. Badcock and G. F. Fernando, "Fabrication of intrinsic fibre Fabry–Perot sensors in silica fibres using hydrofluoric acid etching," *Sensors and Actuators A,* vol. 138, no. 1, pp. 248-260, 2007.

[15] Q. Wu, Y. Semenova, P. Wang and G. Farrell, "High sensitivity SMS fiber structure based refractometer – analysis and experiment," *Opt. Express,* vol. 19, no. 9, pp. 7937-, 2011.

[16] S. Silva, O. Frazao, J. Viegas, L. A. Ferreira, F. M. Araujo, F. X. Malcata and J. L. Santos, "Temperature and strain-independent curvature sensor based on a singlemode/multimode fiber optic structure," *Meas. Sci. Technol. ,* vol. 22, p. 085201 (6pp), 2011.

[17] D. J. J. Hu, J. L. Lim, M. K. Park, L. T.-H. Kao, Y. Wang, H. Wei and W. Tong, "Photonic crystal fiber based interferometric biosensor for streptavidin and biotin detection," *IEEE Sel. Topics Quantum Electron.,* vol. 18, no. 4, pp. 1293-1297, 2012.

[18] S. Gao, W. Zhang, H. Zhang, P. Geng, W. Lin, B. Liu, Z. Bai and X. Xue, "Fiber modal interferometer with embedded fiber Bragg grating for simultaneous measurements of refractive index and temperature," *Sensors and Actuators B: Chemical,* vol. 188, pp. 931-936, 2013.

[19] A. P. Zhang, G. Yan, S. Gao, S. He, B. Kim, J. Im and Y. Chung, "Microfluidic refractive-index sensors based on small-hole microstructured optical fiber Bragg gratings," *Appl. Phys. Lett.,* vol. 98, no. 22, p. 221109, 2011.

[20] D. J. J. Hu, J. L. Lim, M. Jiang, Y. Wang, F. Luan, P. Shum, H. Wei and W. Tong, "Long period grating cascaded to photonic crystal fiber modal interferometer for simultaneous measurement of temperature and refractive index," *Opt. Lett.,* vol. 37, no. 12, p. 2283−2285, 2012.

[21] L. Rindorf and O. Bang, "Highly sensitive refractometer with a photoniccrystal-fiber long-period grating," *Opt. Lett.,* vol. 33, no. 6, pp. 563-565, 2008.

[22] Y. Gong, Y. Guo, Y.-J. Rao, T. Zhao and Y. Wu, "Fiber-Optic Fabry–Pérot Sensor Based on Periodic Focusing Effect of Graded-Index Multimode

Fibers," *IEEE Photon. Techno. Lett.,* vol. 22, no. 23, pp. 1708-1710, 2010.

[23] S.-J. Qiu, Y. Chen, J.-L. Kou, F. Xu and Y.-Q. Lu, "Miniature tapered photonic crystal fiber interferometer with enhanced sensitivity by acid microdroplets etching," *Appl. Opt.,* vol. 50, no. 22, pp. 4328-4332, 2011.

[24] T. A. Birks, J. C. Knight, B. J. Mangan, A. Ortigosa-Blanch and P. S. J. Russell, "Characterisation of photonic crystal fibres," in *Tech. Digest Symp. on Opt. Fib. Measu. (NIST 953)*, Colorado, 2000.

[25] J. C. Knight, T. A. Birks, R. F. Cregan, P. S. J. Russell and J.-P. d. Sandro, "Large mode area photonic crystal fibre," *Electronics Letters,* vol. 34, no. 13, pp. 1347-1348, 1998.

[26] M. C. P. Huy, G. Laffont, Y. Frignac, V. Dewynter-Marty, P. Ferdinand, P. Roy, J.-M. Blondy, D. Pagnoux, W. Blanc and B. Dussardier, "Fibre Bragg grating photowriting in microstructured optical fibres for refractive index measurement," *Meas. Sci. Technol.,* vol. 17, no. 5, pp. 992-997, 2006.

[27] N. Khurram, L. V. Nguyen, K. Alameh and Y. Chung, "Cladding Modes analysis of photonics crystal fiber for refractive index sensors using finite element method," in *Conference on Lasers and Electro-Optics (CLEO)*, San Jose, 2010.

[28] W. Liang, Y. Huang, Y. Xu, R. K. Lee and A. Yariv, "Highly sensitive fiber Bragg grating refractive index sensors," *Appl. Phy. Lett.,* vol. 86, no. 15, p. 151122, 2005.

[29] J.-L. Kou, M. Ding, J. Feng, Y.-Q. Lu, F. Xu and G. Brambilla, "Microfiber-Based Bragg Gratings for Sensing Applications: A Review," *Sensors,* vol. 12, no. 7, pp. 8861-8876, 2012.

[30] R. M. Samarth, "A Thermo-optically Tunable Optical Filter with Grating Assisted Asymmetric Waveguide Coupling," University of Massachusetts Lowell, ProQuest Dissertations Publishing, Michigan, 2011.

[31] E. J. Dickinson, . H. Ekström and E. Fontes, "COMSOL Multiphysics®: Finite element software for electrochemicalanalysis. A mini-review," *Electrochemistry Communications,* vol. 40, pp. 71-74, 2014.

[32] X. C. Tong, "Fundamentals and Design Guides for Optical Waveguides," in *Advanced Materials for Integrated Optical Waveguides*, Switzerland, Springer International Publishing, 2013, p. 32.

[33] J. C. Knight, T. A. Birks, D. M. Atkin and P. S. J. Russell, "Pure silica single-mode fibre with hexagonal photonic crystal cladding," in *Optical*

Fiber Communication (OFC), San Jose, CA, 1996.

[34] K. Oh and U.-C. Paek, Silica Optical Fiber Technology for Devices and Components: Design, Fabrication, and International Standards, New Jersey: Wiley, 2012, p. 15.

[35] P. J. Bennett, T. M. Monro and D. J. Richardson, "Toward practical holey fiber technology: fabrication, splicing, modeling, and characterization," *Optics Letters,* vol. 24, no. 17, pp. 1203-1205, 1999.

[36] K. Tajima, J. Zhou, K. Nakajima and K. Sato, "Ultralow Loss and Long Length Photonic Crystal Fiber," *Journal of Lightwave Technology,* vol. 22, no. 1, pp. 7-10, 2004.

[37] F. Benabid, "Hollow-core photonic bandgap fibre: new light guidance for new science and technology," *Phil. Trans. R. Soc. A,* pp. 1-24, 2006.

[38] R. F. Cregan, B. J. Mangan, J. C. Knight, T. A. Birks, P. S. J. Russell, P. J. Roberts and D. C. Allan, "Single-mode photonic band gap guidance of light in air," *Science,* vol. 285, no. 5433, pp. 1537-1539, 1999.

[39] Y. Zhu, C. Lu and P. Shum, "Photonic crystal fibers and their applications in optical communications and sensors," in *Proc. SPIE 4904, Optical Fiber and Planar Waveguide Technology II*, China, 2002.

[40] B. Lee, S. Roh and J. Park, "Current status of micro- and nano-structured optical fiber sensors," *Optical Fiber Technology,* vol. 15, no. 3, pp. 209-221, 2009.

[41] J. Liu, "Fiber-based tunable laser". U.S. Patent US20090041062 A1, 12 Feb. 2009.

[42] A. Afroozeh, S. E. Pourmand and A. Zeinalinezhad, "Simulation and Calculation of the Parameters of PCF under Terahertz Wave Band," *Advances in Environmental Biology,* vol. 8, no. 21, pp. 263-268, 2014.

[43] Y. Zhao and Z.-q. Deng, "Photonic crystal fiber based surface plasmon resonance chemical sensors," *Sensors and Actuators B: Chemical,* vol. 2023, pp. 557-567, 2014.

[44] W.-J. Liu, H.-N. Han, L. Zhang, R. Wang, Z.-Y. Wei and M. Lei, "Breathers in a hollow-core photonic crystal fiber," *Laser Physics Letters,* vol. 11, no. 4, p. 045402, 2014.

[45] J. M. Dudley and J. R. Taylor, "Ten years of nonlinear optics in photonic

crystal fibre," *Nat. Photon.,* vol. 3, no. 2, pp. 85-90, 2009.

[46] N. Anscombe, "Photonic crystal pioneer," *Nat. Photon.,* vol. 5, no. 8, pp. 464-465, 2011.

[47] D. J. J. Hu, P. Shum, C. Lu, X. Yu, G. Wang and G. Ren, "A holey fiber design for single-polarization single-mode guidance," *Appl. Opt.,* vol. 48, no. 20, pp. 4038-4043, 2009.

[48] D. J. J. Hu, P. Shum, C. Lu and G. Ren, "Dispersion-flattened polarization-maintaining photonic crystal fiber for nonlinear applications," *Opt. Commun.,* vol. 282, no. 20, pp. 4072-4076, 2009.

[49] D. J. J. Hu, G. Alagappan, Y. K. Yeo, P. P. Shum and P. Wu, "Broadband transmission in hollow-core Bragg fibers with geometrically distributed multilayered cladding," *Opt. Exp.,* vol. 18, no. 18, pp. 18671-18684, 2010.

[50] Y. Zhu, P. Shum, H.-W. Bay, M. Yan, X. Yu, J. Hu, J. Hao and C. Lu, "Strain-insensitive and high-temperature long-period gratings inscribed in photonic crystal fiber," *Opt. Lett.,* vol. 30, no. 4, pp. 367-369, 2005.

[51] H. B. Liu, H. Y. Liu, G. D. Peng and P. L. Chu, "Strain and temperature sensor using a combination of polymer and silica fibre Bragg gratings," *Opt. Comm.,* vol. 219, no. 1-6, pp. 139-142, 2003.

[52] G. A. Cárdenas-Sevilla, V. Finazzi, J. Villatoro and V. Pruneri, "Photonic crystal fiber sensor array based on modes overlapping," *Opt. Exp.,* vol. 19, no. 8, pp. 7596-7602, 2011.

[53] E. Li, G.-D. Peng and X. Ding, "High spatial resolution fiber-optic Fizeau interferometric strain sensor based on an in-fiber spherical microcavity," *Appl. Phys. Lett.,* vol. 92, no. 10, p. 101117, 2008.

[54] R. Jha, J. Villatoro and G. Badenes, "Ultrastable in reflection photonic crystal fiber modal interferometer for accurate refractive index sensing," *Appl. Phys. Lett.,* vol. 93, no. 19, p. 191106, 2008.

[55] J. L. Lim, D. J. J. Hu, P. P. Shum and Y. Wang, "Cascaded photonic crystal fiber interferometers for refractive index sensing," *IEEE Photon. Jnl.,* vol. 4, no. 4, pp. 1163-1169, 2012.

[56] K. Milenko, D. J. J. Hu, P. P. Shum, T. Zhang, J. L. Lim, Y. Wang, T. R. Wolinski, H. Wei and W. Tong, "Photonic crystal fiber tip interferometer for refractive index sensing," *Opt. Lett.,* vol. 37, no. 8, pp. 1373-1375, 2012.

[57] S. Silva, J. L. Santos, F. X. Malcata, J. Kobelke, K. Schuster and O. Frazão, "Optical refractometer based on large-core air-clad photonic crystal fibers," *Opt. Lett.,* vol. 36, no. 6, p. 852−854, 2011.

[58] Y. Wang, H. Bartelt, W. Ecke, R. Willsch, J. Kobelke, M. Kautz, S. Brueckner and M. Rothhardt, "Sensing properties of fiber Bragg gratings in small-core Ge-doped photonic crystal fibers," *Opt. Comm,* vol. 282, no. 6, pp. 1129-1134, 2009.

[59] Y. Zhu, P. Shum, J.-H. Chong, M. K. Rao and C. Lu, "Deep-notch, ultracompact long-period grating in a large-mode-area photonic crystal fiber," *Opt. Lett.,* vol. 28, no. 24, pp. 2467-2469, 2003.

[60] H. Kim, J. Kim, U. Paek, B. Lee and K. Kim, "Tunable photonic crystal fiber coupler based on a side-polishing technique," *Opt. Lett.,* vol. 29, no. 11, pp. 1194-1196, 2004.

[61] H. C. Nguyen, B. T. Kuhlmey, E. C. Magi, M. J. Steel, P. Domachuk, C. L. Smith and B. J. Eggleton, "Tapered photonic crystal fibres: properties, characterisation and applications," *Appl. Phys. B,* vol. 81, no. 2-3, pp. 377-987, 2005.

[62] D. L. Kingsbury and P. L. Marston, "Scattering by bubbles in glass: Mie theory and phyiscal optics approximation," *Appl. Opt.,* vol. 20, no. 14, pp. 2348-2350, 1981.

[63] F. R. A. Onofri, M. Krzysiek, J. Mroczka, K.-F. Ren, S. Radev and J.-P. Bonnet, "Optical characterization of bubbly flows with a near-critical-angle scattering technique," *Exp. Fluids.,* vol. 47, no. 4-5, p. 721–732, 2009.

[64] G. E. Davis, "Scattering of Light by an Air Bubble in Water," *J. Opt. Soc. Am.,* vol. 45, no. 7, pp. 572-572, 1955.

[65] N. Kopylov and A. R. Kortan, "Method of elimating light scattering bubles in optical fiber preforms". USA Patent 5,776,222, 07 Jul. 1998.

[66] A. R. Tynes, A. D. Pearson and D. L. Bisbee, "Loss Mechanisms and Measurements in Clad Glass Fibers and Bulk Glass," *J. Opt. Soc. Am.,* vol. 61, no. 2, pp. 143-153, 1971.

[67] N. Morita and N. Kumagai, "Scattering and Mode Conversion of Guided Modes by a Spherical Object in an Optical Fiber," *IEEE Transactions on Microwave Theory and Techniques,* vol. 28, no. 2, pp. 137-141, 1980.

[68] I. D. Chremmos and N. K. Uzunoglu, "Analysis of scattering by a linear chain of spherical inclusions in an optical fiber," *J. Opt. Soc. Am. A,* vol. 23,

no. 12, pp. 3054-3062, 2006.

[69] L. Xiao, W. Jin and M. S. Demokan, "Fusion splicing small-core photonic crystal fibers and single-mode fibers by repeated arc discharges," *Opt. Lett.,* vol. 32, no. 2, pp. 115-117, 2007.

[70] R. Fan, Y. Hou and W. Sun, "Photonic crystal fiber Fabry-Perot interferometers with high-reflectance internal mirrors," *Photonic Sensors,* vol. 5, no. 2, pp. 97-101, 2015.

[71] H. Y. Choi, M. J. Kim and B. H. Lee, "All-fiber Mach-Zehnder type interferometers formed in photonic cystal fiber," *Opt. Express,* vol. 15, no. 9, pp. 5711-5720, 2007.

[72] S.-F. Cheng and L.-K. Chau, "Colloidal Gold-Modified Optical Fiber for Chemical and Biochemical Sensing," *Anal. Chem.,* vol. 75, no. 1, pp. 16-21, 2003.

[73] J. E. Hoffman, S. Ravets, J. A. Grover, P. Solano, P. R. Kordell, J. D. Wong-Campos, L. A. Orozco and S. L. Rolston, "Ultrahigh transmission optical nanofibers," *AIP Advances,* vol. 4, no. 6, p. 067124, 2014.

[74] J. Villatoro, V. Finazzi, G. Coviello and V. Pruneri, "Photonic-crystal-fiber-enabled micro-Fabry–Perot interferometer," *Opt. Lett.,* vol. 34, no. 16, pp. 2441-2443, 2009.

[75] J. Villatoro, V. Finazzi, V. P. Minkovich, V. Pruneri and G. Badenes, "Temperature-insensitive photonic crystal fiber interferometer for absolute strain sensing," *Appl. Phy. Lett.,* vol. 91, no. 9, p. 091109, 2007.

[76] J. H. Chong and M. Rao, "Development of a system for laser splicing photonic crystal fiber," *Opt. Express,* vol. 11, no. 12, pp. 1365-1370, 2003.

[77] F. C. Favero, G. Bouwmans, V. Finazzi, J. Villatoro and V. Pruneri, "Fabry–Perot interferometers built by photonic crystal fiber pressurization during fusion splicing," *Opt. Lett.,* vol. 36, no. 21, pp. 4191-4193, 2011.

[78] D.-W. Duan, Y.-J. Rao, Y.-S. Hou and T. Zhu, "Microbubble based fiber-optic Fabry–Perot interferometer formed by fusion splicing single-mode fibers for strain measurement," *Appl. Opt.,* vol. 51, no. 8, pp. 1033-1036, 2012.

[79] S. Zhang, Q. Zhong, X. Qian, X. Lin, F. Xu, W. Hu and Y. Lu, "A three-beam path photonic crystal fiber modal interferometer and its sensing applications," *J. Appl. Phys.,* vol. 108, no. 2, p. 023107, 2010.

[80] J. Villatoro, V. P. Minkovich, V. Pruneri and G. Badenes, "Simple all-microstructured-optical-fiber interferometer built via fusion splicing," *Opt. Express,* vol. 15, no. 4, p. 1491−1496, 2007.

[81] D. J. J. Hu, Y. Wang, J. L. Lim, T. Zhang, K. B. Milenko, Z. Chen, M. Jiang, G. Wang, F. Luan, P. P. Shum, Q. Sun, H. Wei, W. Tong and T. R. Wolinski, "Novel Miniaturized Fabry–Perot Refractometer Based on a Simplified Hollow-Core Fiber With a Hollow Silica Sphere Tip," *IEEE Sensors Journal,* vol. 12, no. 5, pp. 1239-1245, 2012.

[82] W. Qian, C. C. Chan, C.-L. Zhao, Y. Liu, T. Li, L. Hu, K. Ni and X. Dong, "Photonic crystal fiber refractive index sensor based on a fiber Bragg grating demodulation," *Sensors and Actuators B: Chemical,* Vols. 166-167, pp. 761-765, 2012.

[83] J. H. Chong, P. Shum, H. Haryono, A. Yohana, M. K. Rao, C. Lu and Y. Zhu, "Measurements of refractive index sensitivity using long-period grating refractometer," *Opt. Comm.,* vol. 229, no. 1-6, pp. 65-69, 2004.

[84] P. Schiebener, J. Straub, J. M. H. L. Sengers and J. S. Gallagher, "Refractive index of water and steam as function of wavelength, temperature and density," *J. Phys. Chem. Ref. Data,* vol. 19, no. 3, pp. 677-718, 1990.

[85] Y. Jung, S. Kim, D. Lee and K. Oh, "Compact three segmented multimode fibre modal interferometer for high sensitivity refractive-index measurement," *Meas. Sci. Technol.,* vol. 17, no. 5, pp. 1129-1133, 2006.

[86] A. Mehta, W. Mohammed and E. G. Johnson, "Multimode Interference-Based Fiber-Optic Displacement Sensor," *IEEE Photon. Technol. Lett.,* vol. 15, no. 8, pp. 1129-1131, 2003.

[87] O. Krupin, H. Asiri, C. Wang, R. N. Tait and P. Berini, "Biosensing using straight long-range surface plasmon waveguides," *Opt. Express,* vol. 21, no. 1, pp. 698-709, 2012.

[88] J. Beuthan, O. Minet, J. Helfmann, M. Herrig and G. Müller, "The spatial variation of the refractive index in biological cells," *Phys. Med. Biol.,* vol. 41, no. 3, pp. 369-382, 1996.

[89] W. Choi, C. Fang-Yen, K. Badizadegan, S. Oh, N. Lue, R. R. Dasari and M. S. Feld, "Tomographic phase microscopy," *Nature Methods,* vol. 4, no. 9, pp. 717-719, 2007.

[90] R. M. Pearson, "The refractive index of contact lens saline solutions," *Contact Lens & Anterior Eye,* vol. 36, no. 3, pp. 136-139, 2013.

[91] J. G. Lyubovitsky, "CaltechTHESIS," 15 Apr 2003. [Online]. Available: https://thesis.library.caltech.edu/1322/. [Accessed 28 05 2018].

[92] N. Lue, G. Popescu, T. Ikeda, R. R. Dasari, K. Badizadegan and M. S. Feld, "Live cell refractometry using microfluidic devices," *Opt. Lett.,* vol. 31, no. 18, pp. 2759-2761, 2006.

[93] S. M. Partridge, H. F. Davis and G. S. Adair, "The Chemistry of Connective Tissues - 2. Soluble proteins derived from partial hydrolysis of elastin," *Biochem. Journal,* vol. 61, no. 1, pp. 11-21, 1955.

[94] F. P. Bolin, L. E. Preuss, R. C. Taylor and R. J. Ference, "Refractive index of some mammalian tissues using a fiber optic cladding method," *Appl. Opt.,* vol. 28, no. 12, pp. 2297-2303, 1989.

[95] W. J. Bock, T. A. Eftimov, P. Mikulic and J. Chen, "An Inline Core-Cladding Intermodal Interferometer Using a Photonic Crystal Fiber," *Jnl. of Lightwave Techno.,* vol. 27, no. 17, p. 3933, 2009.

[96] S. Silva, J. L. Santos, F. X. Malcata, J. Kobelke, K. Schuster and O. Frazão, "Optical refractometer based on large-core air-clad photonic crystal fibers," *Opt. Lett.,* vol. 36, no. 6, pp. 852-854, 2011.

[97] Q. Wang and G. Farrell, "All-fiber multimode-interference-based refractometer sensor: proposal and design," *Opt. Lett.,* vol. 31, no. 3, pp. 317-319, 2006.

[98] G. Lin, M.-Y. Fu, H.-J. Sheng, H.-T. Sun and W.-F. Liu, "A High Sensitivity Index Sensor Based on No-Core Fibers," *Applied Mechanics and Materials,* Vols. 284-287, pp. 1986-1990, 2013.

[99] J. Villatoro, M. O. Kreuzer, R. Jha, V. P. Minkovich, V. Finazzi, G. Badenes and V. Pruneri, "Photonic crystal fiber interferometer for chemical vapor detection with high sensitivity," *Opt. Exp.,* vol. 17, no. 3, pp. 1447-1453, 2009.

[100] D. Passaro, M. Foroni, F. Poli, A. Cucinotta, S. Selleri, J. Laegsgaard and A. O. Bjarklev, "All-silica hollow-core microstructured Bragg fibers for biosensor application," *IEEE Sensors Jnl.,* vol. 8, no. 7, pp. 1280-1286, 2008.

[101] X. Sun, "Wavelength-selective coupling of dual-core photonic crystal fiber with a hybrid light-guiding mechanism," *Opt. Lett.,* vol. 32, no. 17, pp. 2484-2486, 2007.

[102] B. Sun, M.-Y. Chen, Y.-K. Zhang and J.-C. Yang, "Design of refractive index sensors based on the wavelength-selective resonant coupling

phenomenon in dual-core photonic crystal fibers," *J. Biomed. Opt.,* vol. 17, no. 3, p. 037002, 2012.

[103] J. J. Hu, P. Shum, G. Ren, X. Yu, G. Wang, C. Lu, S. Ertman and T. R. Wolinski, "Investigation of thermal influence on the bandgap properties of liquid-crystal photonic crystal fibers," *Opt. Commun.,* vol. 281, no. 17, pp. 4339-4342, 2008.

[104] D. J. J. Hu, P. Shum, C. Lu, X. Sun, G. Ren, X. Yu and G. Wang, "Design and analysis of thermally tunable liquid crystal filled hybrid photonic crystal fiber coupler," *Opt. Commun.,* vol. 282, no. 12, pp. 2343-2347, 2009.

[105] K. Nielsen, D. Noordegraaf, T. Srensen, A. Bjarklev and T. P. Hansen, "Selective filling of photonic crystal fibres," *J. Opt. A: Pure Appl. Opt.,* vol. 7, no. 8, pp. L13-L20, 2005.

[106] A. M. Jones, A. V. V. Nampoothiri, A. Ratanavis, T. Fiedler, N. V. Wheeler, F. Couny, R. Kadel, F. Benabid, B. R. Washburn, K. L. Corwin and W. Rudolph, "Mid-infrared gas filled photonic crystal fiber laser based on population inversion," *Opt. Exp.,* vol. 19, no. 3, pp. 2309-2316, 2011.

[107] Y. Cui, P. P. Shum, D. J. J. Hu, G. Wang, G. Humber and Q. Dinh, "Temperature sensor by using selectively-filled photonic crystal fiber Sagnac interferometer," *IEEE Photon. J.,* vol. 4, no. 5, pp. 1801-1808, 2012.

[108] H. W. Lee, M. A. Schmidt and P. S. J. Russell, "Excitation of a nanowire "molecule" in gold-filled photonic crystal fiber," *Opt. Lett.,* vol. 37, no. 14, pp. 2946-2948, 2012.

[109] N. Healy, J. R. Sparks, R. R. He, P. J. A. Sazio, J. V. Badding and A. C. Peacock, "High index contrast semiconductor ARROW and hybrid ARROW fibers," *Opt. Exp.,* vol. 19, no. 11, pp. 10979-10985, 2011.

[110] D. K. C. Wu, B. T. Kuhlmey and B. J. Eggleton, "Ultrasensitive photonic crystal fiber refractive index sensor," *Opt. Lett.,* vol. 34, no. 3, pp. 322-324, 2009.

[111] Y. Wang, M. Yang, D. N. Wang and C. R. Liao, "Selectively infiltrated photonic crystal fiber with ultrahigh temperature sensitivity," *IEEE Photon. Technol. Lett.,* vol. 23, no. 20, pp. 1520-1522, 2011.

[112] T. R. Wolinski, K. Szaniawska, S. Ertman, P. Lesiak, A. W. Domanski, R. Dabrowski, E. Nowinowski-Kruszelnicki and J. Wojcik, "Influence of temperature and electrical fields on propagation properties of photonic liquid-crystal fibres," *Meas. Sci. Technol.,* vol. 17, no. 5, pp. 985-991, 2006.

[113] D. J. J. Hu, J. L. Lim, Y. Cui, K. Milenko, Y. Wang, P. P. Shum and T. Wolinski, "Fabrication and Characterization of a Highly Temperature Sensitive Device Based on Nematic Liquid Crystal-Filled Photonic Crystal Fiber," *IEEE Photon. Jnl.,* vol. 4, no. 5, pp. 1248-1255, 2012.

[114] S.-M. Kuo, Y.-W. Huang, S.-M. Yeh, W.-H. Cheng and C.-H. Lin, "Liquid crystal modified photonic crystal fiber (LC-PCF) fabricated with an un-cured SU-8 photoresist sealing technique for electrical flux measurement," *Opt. Exp.,* vol. 19, no. 19, pp. 18372-18379, 2011.

[115] F. Du, Y. Lu and S.-T. Wu, "Electrically tunable liquid-crystal photonic crystal fiber," *Appl. Phys. Lett.,* vol. 85, no. 12, pp. 2181-2183, 2004.

[116] T. R. Wolinski, S. E. A. Czapla, M. Tefelska, A. W. Domanski, J. Wojcik, E. Nowinowski-Kruszelnicki and R. Dabrowski, "Photonic liquid crystal fibers for sensing applications," *IEEE Trans. Instrum. Meas.,* vol. 57, no. 8, pp. 1796-1802, 2008.

[117] J. J. Hu, G. Ren, P. Shum, X. Yu, G. Wang and C. Lu, "Analytical method for band structure calculation of photonic crystal fibers filled with liquid crystal," *Opt. Exp.,* vol. 16, no. 9, pp. 6668-6674, 2008.

[118] G. Ren, P. Shum, J. Hu, X. Yu and Y. Gong, "Study of polarization-dependent bandgap formation in liquid crystal filled photonic crystal fibers," *IEEE Photon. Technol. Lett.,* vol. 20, no. 8, pp. 602-604, 2008.

[119] D. J. J. Hu, P. P. Shum, J. L. Lim, Y. Cui, K. Milenko, Y. Wang and T. Wolinski, "A Compact and Temperature-Sensitive Directional Coupler Based on Photonic Crystal Fiber Filled With Liquid Crystal 6CHBT," *IEEE Photon. J.,* vol. 4, no. 5, pp. 2010-2016, 2012.

[120] F. Pang, W. Xiang, H. Guo, N. Chen, X. Zeng and Z. Chen, "Special optical fiber for temperature sensing based on cladding-mode resonance," *Opt. Lett.,* vol. 16, no. 17, pp. 12967-12972, 2008.

[121] L. Jin, Z. Wang, Q. Fang, B. Liu, Y. Liu, G. Kai, X. Dong and B. Guan, "Bragg grating resonances in all-solid bandgap fibers," *Opt. Lett.,* vol. 32, no. 18, pp. 2717-2719, 2007.

[122] Z. Xu, J. L. Lim, D. J. J. Hu, Q. Sun, R. Y.-N. Wong, M. Jiang and P. P. Shum, "Investigation of temperature sensing characteristics in selectively infiltrated photonic crystal fiber," *Opt. Express,* vol. 24, no. 2, pp. 1699-1707, 2016.

[123] J. Petrovic, Y. Lai and I. Bennion, "Numerical and experimental study of microfluidic devices in step-index optical fibers," *Appl. Opt.,* vol. 47, no. 10,

p. 1410–1416, 2008.

[124] A. Nahmad-Rohen, H. Contreras-Tello, G. Morales-Luna and A. García-Valenzuela, "On the effective refractive index of blood," *Phys. Scr.,* vol. 91, no. 1, p. 015503 (8pp), 2016.

[125] J. G. Quinn, S. O'Neill, A. Doyle, C. McAtamney, D. Diamond, B. D. MacCraith and R. O'Kennedy, "Development and Application of Surface Plasmon Resonance-Based Biosensors for the Detection of Cell–Ligand Interactions," *Analytical Biochemistry,* vol. 281, no. 2, pp. 135-143, 2000.

[126] J. L. Lim, D. J. J. Hu, P. P. Shum and Y. Wang, "Design and Analysis of Microfluidic Optical Fiber Device for Refractive Index Sensing," *IEEE Photon. Tech. Lett.,* vol. 26, no. 21, pp. 2130-2133, 2014.

[127] K. Zhou, Y. Lai, K. Sugden, L. Zhang and I. Bennion, "A refractometer based on a micro-slot in a fiber Bragg grating formed by chemically assisted femtosecond laser processing," *Opt. Exp.,* vol. 15, no. 24, p. 15848–15853, 2007.

[128] C. Grillet, P. Domachuk, V. Ta'eed, E. Mägi, J. A. Bolger, B. J. Eggleton and L. E. Rodd, "Compact tunable microfluidic interferometer," *Opt. Exp.,* vol. 12, no. 22, p. 5440–5447, 2004.

[129] K. C. Vishnubhatla, N. Bellini, R. Ramponi, G. Cerullo and R. Osellame, "Shape control of microchannels fabricated in fused silica by femtosecond laser irradiation and chemical etching," *Optics Express,* vol. 17, no. 10, pp. 8685-8695, 2009.

[130] A. Marcinkevičius, S. Juodkazis, M. Watanabe, M. Miwa, S. Matsuo, H. Misawa and J. Nishii, "Femtosecond laser-assisted three-dimensional microfabrication in silica," *Optics Letters,* vol. 26, no. 5, pp. 277-279, 2001.

[131] Y. Lai, K. Zhou, L. Zhang and I. Bennion, "Microchannels in conventional single-mode fibers," *Opt. Lett.,* vol. 31, no. 17, pp. 2559-2561, 2006.

[132] F. Poli, A. Cucinotta and S. Selleri, Photonic Crystal Fibers: Properties and Applications, Dordrecht: Springer, 2007.

[133] K. Kurokawa, K. Tajima, K. Tsujikawa, K. Nakajima, T. Matsui, I. Sankawa and T. Haibara, "Penalty-Free Dispersion-Managed Soliton Transmission Over a 100-km Low-Loss PCF," *Jnl. of Lightwave Tech.,* vol. 24, no. 1, pp. 32-37, 2006.

[134] W. G. French, J. B. MacChesney, P. B. O'Connor and G. W. Tasker, "Optical waveguides with very low losses," *The Bell Sys. Tech. J.,* vol. 53, pp. 951-

954, 1974.

[135] J. B. MacChesney, P. B. O'Connor, F. V. DiMarcello, J. R. Simpson and P. D. Lazay, "Preparation of low loss optical fibers using simultaneous vapor phase deposition and fusion," in *Proc. of Intern. Congr. on Glass*, Kyoto, 1974.

[136] Kenneth E. Hendrickson, The Encyclopedia of the Industrial Revolution in World History, vol. 3, Maryland: Rowman & Littlefield, 2015.

[137] T. Li, Optical Fiber Communications: Fiber Fabrication, vol. 1, Florida: Academic Press, 1985, p. 34.

[138] W. H. Tranter, D. P. Taylor, R. E. Ziemer, N. F. Maxemchuk and J. W. Mark, The Best of the Best: Fifty Years of Communications and Networking Research, Canda: Wiley-IEEE Press, 2007, pp. 194-196.

[139] Y. Zhang, Y. Li, X. Lan, Y. Huang, G. Chen and H. Xiao, "Fringe Visibility Enhanced Extrinsic Fabry–Perot Interferometer Using a Graded Index Fiber Collimator," *IEEE Photon. Jnl.,* vol. 2, no. 3, pp. 469-481, 2010.

[140] B. J. Thompson and E. Wolf, "Two-Beam Interference with Partially Coherent Light," *Jnl. of the Opt. Society of America,* vol. 47, no. 10, pp. 895-902, 1957.

[141] Y. Tian, W. Wang, N. Wu, X. Zou, C. Guthy and X. Wang, "A Miniature Fiber Optic Refractive Index Sensor Built in a MEMS-Based Microchannel," *Sensors,* vol. 11, no. 1, pp. 1078-1087, 2011.

[142] S. Todoroki, "Fiber fuse propagation behavior," in *Selected Topics on Optical Fiber Technology*, Croatia, IntechOpen, 2012, pp. 551-570.

[143] R. Kashyap, "Kashyap -- The Fiber Fuse - from a curious effect to a critical issue: A 25th year retrospective," *Opt. Express,* vol. 21, no. 5, pp. 6422-6441, 2013.

[144] E. M. Dianov, I. A. Bufetov and A. A. Frolov, "Destruction of silica fiber cladding by the fuse effect," *Opt. Express,* vol. 29, no. 16, pp. 1852-1854, 2004.

THE END